Master's Thesis

Temporal Localized States in Injected Microcavities: The Influence of Phase Modulation

Submitted by

Marc Hunkemöller

4. September 2024

First Examiner: PD Dr. Svetlana V. Gurevich

Second Examiner: Prof. Dr. Julien J. P. Javaloyes

Universität Münster

institut für theoretische physik

Contents

1 Introduction

Localized states (LSs) are a natural phenomenon observed across various disciplines. Examples include special vegetation patterns like fairy circles in biology [Get+22], vibrated granular materials [UMS96], water waves [MFS87], and, of course, optics [ABR99]. These structures are considered localized due to their short correlation range, which is much smaller than the domain size.
The nature of LSs depends on the specific system in which they occur. First, they can be classified as either conservative or dissipative. In conservative systems, a given parameter set leads to a family of soliton solutions. In contrast, dissipative systems result in a fixed solution due to the presence of attractors [GA12]. Next, LSs can manifest in different forms depending on the characteristics of the localization, such as temporal [Sch+19], spatial [MFS87; Nie+92], vectorial [Pes+04] and in phase [HK84; Gus+15]. Temporal localized states (TLSs) can evolve across two or more different time scales, for example induced by time delay, exhibiting similarities to spatial LS [YG14; YG17].
In recent decades, TLSs in optical systems have garnered significant interest in nonlinear optics due to their potential applications in optical information storage and processing [Leo+10; Her+14]. TLSs naturally occur in optical systems with injected microcavities [Del+07; Bar+16], where they form continuous pulse trains closely related to optical frequency combs [Lug+18]. The repetition rate of TLS is directly linked to the spacing between the peaks constituting the frequency comb [Lug+18]. Applications for optical frequency combs include arbitrary pulse generation [CW10], among others.
This thesis examines a vertical external-cavity delayed Kerr Gires-Tournois interferometer (KGTI) under continuous wave (CW) injection [Sch+19]. In this setup, the interplay of Kerr nonlinearity and second-order dispersion forms a bistable cavity response, allowing for the realization of TLS. The external cavity introduces a delay, enriching the dynamics by allowing evolution on different time scales. This setup provides a rich playground for various dynamics [Sch+19], including conservative solitons in delayed systems [SGJ22], dissipative TLS [SJG22], and square waves [Koc+22], just to name a few. In the weakly dissipative limit, the KGTI is described by the Lugiato-Lefever equation [LL87], leading to similarities with the nonlinear Schrödinger equation in the conservative limit [SGJ22].
Additionally, this thesis expands the KGTI model by introducing external phase modulation, which influences the dynamics of the pulses like a potential. This creates confinement, alters dynamics, and affects the pulse position.
Thus, the goal of this thesis is to explore the changes in the dynamics of the KGTI

when phase modulation is added. By systematically analyzing how phase modulation affects the formation, stability, and behavior of temporal localized states, we aim to uncover new insights into the interaction between nonlinearity, dispersion, and external phase modulation. This investigation involves both theoretical and numerical studies, utilizing mainly the frameworks of path continuation and numerical integration.
Finally, this thesis aims to deepen our understanding of complex nonlinear optical systems and lead to potential applications in areas such as optical information processing and advanced optical communication technologies [Leo+10; SPH12]. By bridging concepts from different physical systems, this research may contribute to broader interdisciplinary advancements in the study of localized states and soliton dynamics.

1.1 Outline

This thesis is structured as described in the following. After the Introduction in Chapter 1, we provide the theoretical background and review previous results relevant to this thesis in Chapter 2.
We begin the analysis of the modulated system, viewed as a standard synchronization problem, in Chapter 3.1. We find synchronization regions in the frame work of Arnold tongues, saddle-node infinite period bifurcations and excitable orbits.
Next, in Chapter 3.2, we explore the weakly dissipative limit of the KGTI also called the uniform field limit where the field amplitudes are small and thus the influence of the nonlinearity is small. Additionally, we analyze the TLS within the framework of Hermite-Gauss modes and resonance curves thereof.
Further, in Chapter 3.3 we leave the weakly dissipative limit and briefly study the nonlinear regime close to the weakly dissipative limit where similar behavior can be found as before. Moreover, we are able to stabilize TLS outside a bistable CW solution.
In Chapter 3.4, we look into a highly nonlinear regime where the KGTI exhibits complex dynamics due to the interplay of nonlinearity, second- and third-order dispersion, injection, losses, and phase modulation. Supplementing the observed dynamics, we analyze the pulse positions by modeling the pulses as particles in a potential in Chapter 3.5. In Chapter 3.5.1 we determine the neutral modes of the system to facilitate this study.
The thesis concludes with a summary, discussion of open questions, and future research directions in Chapter 4.

2 Theoretical Preliminaries

First, we aim to establish a common framework for the subsequent discussion by providing foundational knowledge of nonlinear physics, time-delay systems, and other relevant concepts. We begin with fundamental definitions, followed by an analysis of stability and bifurcations. Next, we briefly discuss localized states and the derivation of the equations governing the KGTI system. Finally, we cover the basics of synchronization and the numerical methods utilized in this thesis.

2.1 Dynamical Systems

Dynamical systems provide a mathematical framework for modeling the time evolution of real-world phenomena. The state of such a system at any given time t is typically represented by an n-dimensional vector $\boldsymbol{x}(t)$. The behavior of the system is governed by differential equations, which can be written as:

$$\dot{\boldsymbol{x}}(t) = \boldsymbol{F}\left(\boldsymbol{x}(t), t, \boldsymbol{\mu}\right), \tag{2.1}$$

with an initial condition specified by

$$\boldsymbol{x}_0 = \boldsymbol{x}(t_0), \tag{2.2}$$

where $\dot{\boldsymbol{x}}$ represents the time derivative of $\boldsymbol{x}$, $\boldsymbol{\mu}$ is a vector of parameters, and $\boldsymbol{x}_0$ denotes the initial state of the system at time t_0. This constitutes an initial value problem, where the solution must satisfy both the differential equation and the initial condition.
Dynamical systems are broadly classified based on whether the time t and the state vector $\boldsymbol{x}(t)$ are discrete or continuous. They can also be categorized according to whether they are spatially extended. For instance, systems with continuous time and state variables are modeled by partial differential equations (PDEs), while those without spatial extension are modeled with ordinary differential equations (ODEs). If a system has no explicit time dependence it is called autonomous. Otherwise, it is nonautonomous.
Key concepts in the study of dynamical systems include trajectories, which represent the paths traced by the state vector $\boldsymbol{x}(t)$ in phase space over time. The phase space represents all possible states of a dynamical system and the dimensions of the phase space correspond to the degrees of freedom of the system. Trajectories are unique and do not intersect due to the deterministic nature of differential equations. Additionally, the long-term behavior of a dynamical system can often be characterized by subsets of phase space called attractors, which are sets towards which trajectories tend to evolve. The unstable equivalent would be called a repeller. In some cases, attractors can have

complex geometric shapes and a fractal dimension. In these cases, the trajectories are aperiodic and highly sensitive to the initial conditions, leading to unpredictable motion and chaos [Str15].
Understanding the structure and behavior of dynamical systems is essential for various fields, including physics, engineering, biology, and economics. By analyzing these systems, one can predict the future behavior of complex phenomena, optimize processes, and gain insights into the underlying mechanics of natural and engineered systems [Ern08; Str15].

2.1.1 Delay-Differential Equations

In real-world systems, finite propagation times make the system dependent on its past states, leading to delay-differential equations (DDEs). Using our previous notation, a DDE can be expressed as:

$$\dot{\boldsymbol{x}}(t) = \boldsymbol{F}(\boldsymbol{x}(t), \boldsymbol{x}(t-\tau), t, \boldsymbol{\mu}). \tag{2.3}$$

Here, the system depends on its state at time $t - \tau$. The initial condition must be specified as a function over the interval $[t_0 - \tau, t_0)$ leading to infinite degrees of freedom. Because of this DDEs are infinite dimensional, resulting in an infinite-dimensional phase space [Ern08]. Systems can depend on multiple or state-dependent delays.
This thesis examines a delay algebraic equation (DAE). Such a system can be written as:

$$\boldsymbol{M}\dot{\boldsymbol{x}}(t) = \boldsymbol{F}(\boldsymbol{x}(t), \boldsymbol{x}(t-\tau), t, \boldsymbol{\mu}), \tag{2.4}$$

where $\boldsymbol{M}$, called the *mass matrix*, has entries on its diagonal that are either one or zero. A zero entry removes the time derivative of the corresponding field, rendering only an algebraic constraint rather than a full differential equation. In our system, there is only one constant delay, τ, and all time-delayed terms are contained in the algebraic constraint. Because of this structure, we can insert the algebraic constraint into the other equation repeatedly, resulting in effectively infinitely many delays: $2\tau, 3\tau, 4\tau, \ldots$.

2.2 Linear Stability

Understanding whether a solution to a dynamical system is stable is crucial to determine if it can be realized in real-world scenarios. Stability analysis evaluates if small perturbations to the solution are amplified or damped by the system. Linear stability analysis, which involves linearizing the system around a specific solution, is one common method to determine this.

2.2.1 Linear Stability of Fixed Points

A basic solution to a system $\boldsymbol{F}$, without delay, is a fixed point $\boldsymbol{x}^*$. Such a fixed point satisfys $\dot{\boldsymbol{x}} = \boldsymbol{F}(\boldsymbol{x}^*, t, \boldsymbol{\mu}) = 0$. A fixed point lies on an invariant manifold and remains unchanged over time, i.e., $\boldsymbol{x}^*(t) = \boldsymbol{x}^*$. To analyze the stability of this fixed point, we introduce a small perturbation $\boldsymbol{\delta}(t)$. Using the ansatz $\boldsymbol{x}(t) = \boldsymbol{x}^* + \boldsymbol{\delta}(t)$ and linearizing the system up to first order, we get:

$$\begin{aligned}\dot{\boldsymbol{\delta}}(t) &= \boldsymbol{F}(\boldsymbol{x},t,\boldsymbol{\mu})|_{\boldsymbol{x}=\boldsymbol{x}^*} + (\boldsymbol{\nabla F})(\boldsymbol{x},t,\boldsymbol{\mu})|_{\boldsymbol{x}=\boldsymbol{x}^*}\,\boldsymbol{\delta}(t) + \mathcal{O}\Big(\boldsymbol{\delta}^2\Big)\\ &= \mathcal{L}\boldsymbol{\delta}(t) + \mathcal{O}\Big(\boldsymbol{\delta}^2\Big),\end{aligned}$$

where $\mathcal{L} = (\boldsymbol{\nabla F})(\boldsymbol{x},t,\boldsymbol{\mu})|_{\boldsymbol{x}=\boldsymbol{x}^*}$ is the Jacobian matrix evaluated at the fixed point. This results in a linear differential equation. Using the ansatz $\boldsymbol{\delta}(t) = \boldsymbol{\delta}_0 e^{\lambda t}$, for $|\boldsymbol{\delta}_0| \ll 1$, the differential equation transforms into an eigenvalue problem. Since $\mathcal{L}$ is an $n \times n$ matrix and $\boldsymbol{\delta}_0$ an n-dimensional vector, there are n eigenvalues and n eigenvectors. A positive real part of an eigenvalue indicates an exponential amplification of the perturbation, leading to an unstable fixed point. A fixed point is stable if the real parts of all eigenvalues are negative, causing all perturbations to be damped exponentially.
For a two-dimensional case, the eigenvalues $\lambda_\pm$ can be found using the trace-determinant criterion:

$$\lambda_\pm = \frac{1}{2}\left(\mathrm{tr}(\mathcal{L}) \pm \sqrt{\mathrm{tr}(\mathcal{L})^2 - 4\mathrm{det}(\mathcal{L})}\right). \tag{2.5}$$

This shows that eigenvalues can be complex. A non-zero imaginary part of the eigenvalues corresponds to an oscillatory solution, leading to an inward or outward spiraling trajectory around the fixed point.

2.2.2 Linear Stability for Systems with Time Delay

To determine the linear stability of a fixed point for a system with time delay, we start with the equation $\dot{\boldsymbol{\delta}}(t) = \boldsymbol{F}\left(\boldsymbol{x}(t), \boldsymbol{x}(t-\tau), t, \boldsymbol{\mu}\right)$. Using the same ansatz as before yields:

$$\dot{\boldsymbol{\delta}}(t) = \boldsymbol{A}(t)\boldsymbol{\delta}(t) + \boldsymbol{B}(t)\boldsymbol{\delta}(t-\tau) + \mathcal{O}\left(\boldsymbol{\delta}^2\right), \tag{2.6}$$

where

$$\boldsymbol{A}(t) = \partial_1 \boldsymbol{F}\left(\boldsymbol{x}(t), \boldsymbol{x}(t-\tau), t, \boldsymbol{\mu}\right)|_{\boldsymbol{x}=\boldsymbol{x}^*}, \quad \boldsymbol{B}(t) = \partial_2 \boldsymbol{F}\left(\boldsymbol{x}(t), \boldsymbol{x}(t-\tau), t, \boldsymbol{\mu}\right)|_{\boldsymbol{x}=\boldsymbol{x}^*}. \tag{2.7}$$

Here, $\boldsymbol{A}$ and $\boldsymbol{B}$ are the Jacobians with respect to the first and second arguments, evaluated at the solution $\boldsymbol{x}^*$. Since $\boldsymbol{x}^*$ is a stationary solution, $\boldsymbol{A}$ and $\boldsymbol{B}$ are time-independent. Using the same exponential ansatz for the perturbation as before, the problem turns into an eigenvalue problem for λ, and therefore the stability depends on the characteristic equation:

$$\det\left(-\lambda\mathbb{1} + \boldsymbol{A} + \boldsymbol{B}e^{-\lambda\tau}\right) = 0. \tag{2.8}$$

This equation is a quasi-polynomial and generally has an infinite number of complex solutions [YG17]. However, the eigenvalues are bounded to the left, meaning there exists some $C \in \mathbb{R}$ such that $\mathrm{Re}(\lambda) < C$, and they accumulate at $-\infty$. Thus, only a finite number of eigenvalues contribute to the stability, determined by their real parts, as previously discussed [Hal71].

In the long delay limit [YG15], where $\tau \gg 1$, meaning that the delay time is assumed to be significantly larger than the intrinsic timescales of the system, the eigenvalues can be split into two parts: a pseudo-continuous spectrum and an instantaneous spectrum. For the pseudo-continuous spectrum, we know that the roots converge to curves given by:

$$\lambda = \frac{\gamma(\omega)}{\tau} + \mathrm{i}\omega. \tag{2.9}$$

where the real part scales with $1/\tau$, as the perturbations stemming from the delay can only grow as fast as the delay [LWY11]. The distance between neighboring eigenvalues scales with $2\pi/\tau$ [YG17]. As a consequence, for increasing delay, the discrete spectrum of eigenvalues for a system with long delay becomes pseudo-continuous and resembles the dispersion-relation curves of a spatially extended system. Additionally, the discrete nature of the eigenvalues is similar to that of spatially extended systems on a bounded domain. For a diverging delay, $\tau \to \infty$, the pseudo-continuous eigenvalues will tend to the critical value $|\lambda| = 1$ [YP09].
The instantaneous spectrum consists of n eigenvalues, where n is the number of fields. These eigenvalues originate from the ordinary differential equation part of Eq. (2.6), $\dot{\boldsymbol{\delta}}(t) = \boldsymbol{A}(t)\boldsymbol{\delta}(t)$, corresponding to the system without delay [YP09]. A mass matrix, as in Eq. (2.4), reduces the number of instantaneous eigenvalues to the number of non-zero elements on the diagonal of $\boldsymbol{M}$.
However, for $\tau \to \infty$ the instantaneous eigenvalues will tend to some unstable value:

$$\lambda \to \lambda_\infty, \quad |\lambda_\infty| > 1. \tag{2.10}$$

These eigenvalues always have a negative real part for the considered system and parameter range of this thesis, and are therefore not of further interest. The instantaneous eigenvalues are also call *strongly unstable eigenvalues* because they will diverge on a much faster time scale than the pseudo-continuous eigenvalues, since they are independent of the delay [YP09].

2.2.3 Poincaré Map

In the study of dynamical systems, reducing the system's dimensionality methodically can be highly beneficial. A Poincaré map is a tool used to achieve this by reducing the dimension of a system by one, while preserving crucial information about the long-term behavior of trajectories [AFs15]. Consider an n-dimensional system $\dot{\boldsymbol{x}} = \boldsymbol{F}(\boldsymbol{x})$ and a hypersurface $\mathcal{S}$ of dimension $(n-1)$, chosen to be transversal to the flow. Denote the k-th intersection point of the trajectory with $\mathcal{S}$ as $\boldsymbol{x}_k$. The Poincaré map $\mathcal{P}$ is defined as

$$\boldsymbol{x}_{k+1} = \mathcal{P}(\boldsymbol{x}_k), \tag{2.11}$$

which maps one intersection point to the next.
Poincaré maps are especially useful for studying flows near periodic orbits. In systems with an attracting periodic orbit, all $\boldsymbol{x}_k$ eventually accumulate near the intersection point of the periodic orbit and the hypersurface $\mathcal{S}$, converging to the intersection point.

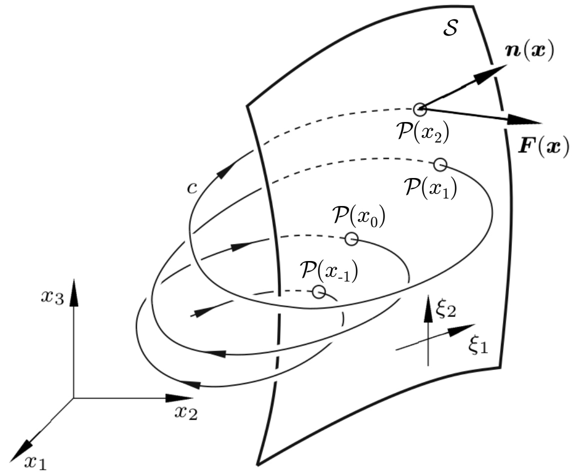

Figure 2.1: Illustration of a Poincaré map $\mathcal{P}$ which projects each intersection of the trajectory and the hypersurface $\mathcal{S}$ onto the next. Adapted from [AFs15].

Thus, for a fixed point $\boldsymbol{x}^*$ of $\mathcal{P}$ (i.e., $\mathcal{P}(\boldsymbol{x}^*) = \boldsymbol{x}^*$), the corresponding trajectory is a periodic orbit [Str15]. Poincaré maps help in the stability analysis of these periodic orbits, as you will see in the following section.

2.2.4 Linear Stability of Periodic Solutions

Another special kind of solution to a dynamical system is a periodic orbit. This means that the solution changes in time but constantly repeats itself with a period T, i.e. $\boldsymbol{x}^*(t) = \boldsymbol{x}^*(t+T)$. To determine the stability of a periodic orbit we need to apply Floquet theory [Flo83]. The basic idea is again to assess a small perturbation and study whether the perturbation is amplified or damped over time. Note, there is no complete Floquet theory for DDEs, however the Floquet multipliers, which determine the stability of a solution, can be defined in a similar way [Jau16]. The following derivation follows [AFs15].
Assuming a system $\dot{\boldsymbol{x}} = \boldsymbol{F}(\boldsymbol{x}, t)$ with the periodic solution $\boldsymbol{x}^*(t) = \boldsymbol{x}^*(t+T)$ and a small perturbation $\boldsymbol{\delta}(t)$. Inserting the ansatz $\boldsymbol{x}(t) = \boldsymbol{x}^*(t) + \boldsymbol{\delta}(t)$ into the system yields

$$\begin{aligned}\dot{\boldsymbol{x}}^*(t) + \dot{\boldsymbol{\delta}}(t) &= \boldsymbol{F}(\boldsymbol{x}^*(t) + \boldsymbol{\delta}(t), t) \\ &= \boldsymbol{F}(\boldsymbol{x}^*(t), t) + \left.\frac{\partial \boldsymbol{F}(\boldsymbol{x}(t), t)}{\partial \boldsymbol{x}}\right|_{\boldsymbol{x}=\boldsymbol{x}^*} \boldsymbol{\delta}(t) + \mathcal{O}\left(\boldsymbol{\delta}^2\right).\end{aligned}$$

With the definition $\mathcal{D}(t) = \left.\frac{\partial \boldsymbol{F}(\boldsymbol{x}(t),t)}{\partial \boldsymbol{x}}\right|_{\boldsymbol{x}=\boldsymbol{x}^*}$ one can conclude a linear set of equations for the small perturbation, neglecting higher order terms,

$$\dot{\boldsymbol{\delta}}(t) = \mathcal{D}(t)\boldsymbol{\delta}(t). \tag{2.12}$$

Since $\boldsymbol{x}^*(t)$ is a periodic function with period T the same follows for the time-dependent coefficient matrix $\mathcal{D}(t)$

$$\mathcal{D}(t) = \mathcal{D}(t+T). \tag{2.13}$$

This characteristic of $\mathcal{D}$ and the characteristics of a Poincaré map are used to reduce the coefficients to constants. In order to find the Poincaré map the fundamental solutions $\boldsymbol{\varphi}_i$, $i = 1, \dots, n$ of the linearized system (2.12) need to be found. A state of the system can be written as a superposition of the fundamental solutions $\boldsymbol{\varphi}_i(t)$:

$$\begin{aligned} \boldsymbol{x}(t) &= c_1\boldsymbol{\varphi}_1(t) + \cdots + c_n\boldsymbol{\varphi}_n(t) \\ &= \boldsymbol{\Phi}(t)\boldsymbol{c} \end{aligned}$$

where $\boldsymbol{\Phi}(t) = (\boldsymbol{\varphi}_1, \dots, \boldsymbol{\varphi}_n)$ and $\boldsymbol{c} = (c_1, \dots, c_n)$. The fundamental solutions shall be normalized such that the initial condition lies on a hypersphere with radius 1. Mathematically, this translates to

$$\boldsymbol{\Phi}(0) = \mathbb{1}. \tag{2.14}$$

Since for each solution $\boldsymbol{x}^*(t)$ the periodicity says that $\boldsymbol{x}^*(t+T)$ is also a solution and thus can be represented by the fundamental solutions there is a constant $n \times n$-matrix $\mathbf{C}$ with

$$\boldsymbol{\Phi}(t+T) = \boldsymbol{\Phi}(t)\mathbf{C}. \tag{2.15}$$

As can be seen from the previous equation $\mathbf{C}$ maps $\boldsymbol{\Phi}(t)$ onto $\boldsymbol{\Phi}(t+T)$ which is in fact, the characteristic of a Poincaré map. Consequently, using the normalization of (2.14), we get:

$$\boldsymbol{\Phi}(T) = \boldsymbol{\Phi}(0)\mathbf{C} = \mathbf{C}, \tag{2.16}$$

where $\mathbf{C}$ is the so-called *monodromy matrix*. Geometrically, the initial solution $\boldsymbol{x}$ lies

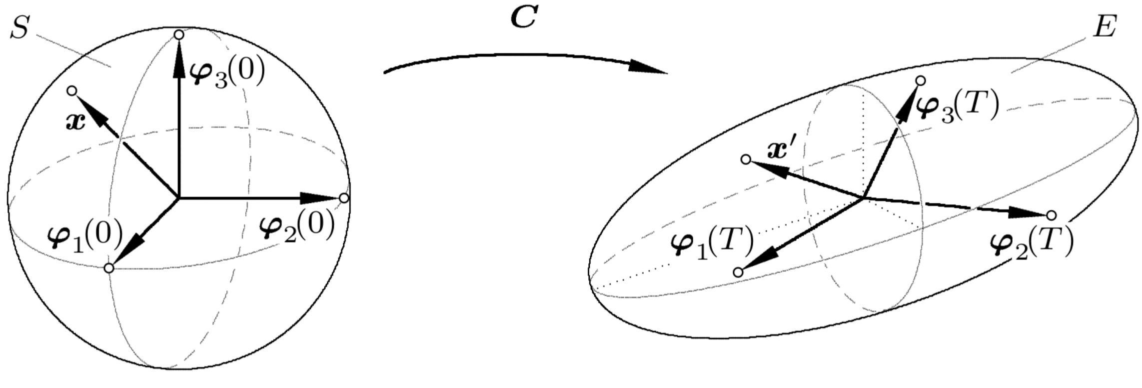

Figure 2.2: Geometrical interpretation of monodromy matrix in a three-dimensional case [AFs15].

on a hypersphere S with radius one. After applying the monodromy matrix the initial solution is projected onto $\boldsymbol{x}'$ and the hypersphere is deformed into an ellipsoid E. The semi-axes of this ellipsoid correspond to the eigenvalues λ_i of the monodromy matrix $\mathbf{C}$ and determine the stability of their periodic orbit. In Fig. 2.2 a corresponding geometrical interpretation of the monodromy matrix and its eigenvalues are given. The eigenvalues are called *Floquet multipliers*. If all Floquet multipliers fulfill $|\lambda_i| < 1$ $\forall i = 1, \dots, n$ the system is stable, i.e. all perturbations will fade away over time. Geometrically speaking, the ellipsoid has to be contained inside of the hypershpere

with radius one. Otherwise, if $|\lambda_i| > 1$ for only one Floquet multiplier the system is unstable and a small perturbation will grow over time.
Since a delay system possesses an infinite number of dimensions the number of Floquet multipliers is infinite. Therefore, numerical methods are used to find the monodromy matrix and its eigenvalues. Starting from Eq. (2.12) and integrating over one period, applying the initial condition, Eq. (2.14), yields the monodromy matrix $\mathbf{C}$. The number of discretization points reduces the dimensionality of the DDE from infinity to a finite number. Furthermore, an autonomous system has at least one Floquet multiplier which has always the value one. This eigenvalue corresponds to the neutral mode, a perturbation along the periodic orbit. This characteristic will be used in deriving an effective equation of motion for the pulse position in chapter 3.5. Otherwise, the case $\max(|\lambda_j|) = 1$ occurs at bifurcations of periodic orbits. To study the behavior of the system at this point nonlinear stability analysis is required [Str15].

2.3 Bifurcation Theory

Bifurcation theory is the study of topological or qualitative changes in the phase space of a system when continuously varying a control parameter. At a critical parameter value, e.g. new fixed points or attractors are created or annihilated, periodic orbits emerge and so on. In general, bifurcations are divided into two main classes.
First, local bifurcations which can be fully identified through linear stability analysis of invariant manifolds, i.e. the study of eigenvalues of the (local) Jacobian in dependence of the control parameter μ. This local changes of phase space can be described with normal forms using weakly nonlinear theory. Normal forms are the simplest dynamical system showing a certain kind of bifurcation.
Second, global bifurcations which correspond to global changes of the phase space, i.e. when changing a control parameter an extended invariant manifolds collides with other structures in phase space. The linear study implemented for local bifurcations cannot describe global bifurcations, therefore no normal form which describe the full bifurcation can be derived. However, there are scaling laws for the amplitude and period which can be used to identify the occurring global bifurcation [Str15].

2.3.1 Fold Bifurcation

In a fold bifurcation, a critical parameter change causes the collision and annihilation of two fixed points. Alternatively, changing the parameter in the opposite direction, leads to the sudden creation of two fixed points, a phenomenon colloquially referred to as "out of the clear blue sky", hence the alternative name *blue sky bifurcation*. Another name for this bifurcation is "saddle-node bifurcation", referring to the unstable (saddle) and stable (node) fixed points involved in bifurcation. The corresponding normal form is represented by the differential equation:

$$\dot{x} = \mu + x^2. \tag{2.17}$$

Depending on the control parameter μ, three distinct cases can be observed, as depicted in Fig. 2.3 (i). Here, the critical value μ_c is zero. For $\mu < 0$, two fixed points exist, one

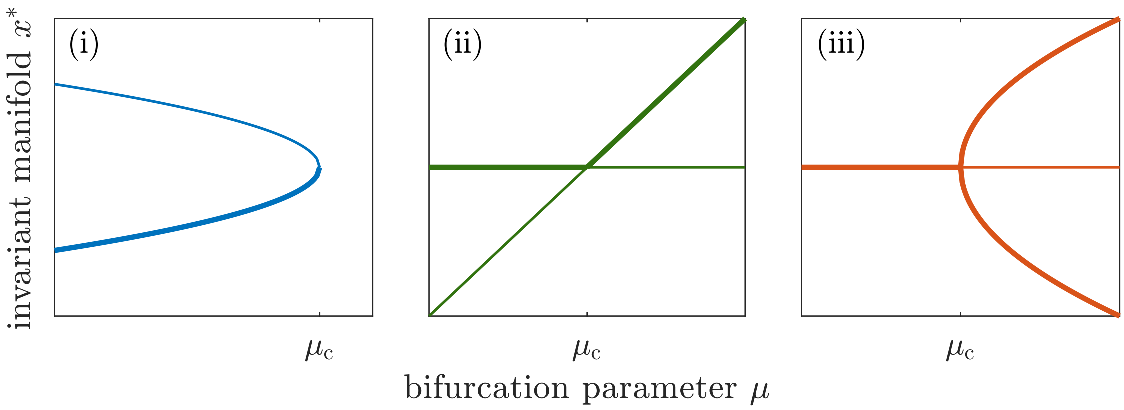

Figure 2.3: Bifurcation diagram of a (i) fold bifurcation, (ii) transcritical bifurcation and (iii) supercritical pitchfork bifurcation. Stable (unstable) fixed points are shown in bold (thin), respectively.

stable and one unstable. Increasing μ to zero results in only one fixed point, and for $\mu > 0$, no fixed points remain. The corresponding bifurcation diagram of fixed points (see Fig. 2.3 (i)) illustrates why this bifurcation is termed a fold bifurcation. Following one fixed point towards μ_c, the curve folds over or under itself [Str15].
A similar bifurcation can occur for two limit cycles, known as the saddle-node bifurcation of cycles. Where a stable and an unstable limit cycle collide and annihilate, similar to the dynamics observed with fixed points [Str15].

2.3.2 Transcritical Bifurcation

In a transcritical bifurcation, one fixed point exists for all values of the control parameter. However, this fixed point exchanges stability with another fixed point. The normal form of this bifurcation is given by

$$\dot{x} = \mu x - x^2. \tag{2.18}$$

The two fixed points are $x^* = 0$ and $x^* = \mu$. The critical value is $\mu_c = 0$. For $\mu < 0$, the fixed point $x^* = 0$ is stable, whereas for $\mu > 0$, the stable fixed point is $x^* = \mu$. The bifurcation is illustrated in Fig. 2.3 (ii) [Str15].

2.3.3 Pitchfork Bifurcation

The normal form of the supercritical pitchfork bifurcation is

$$\dot{x} = \mu x - x^3. \tag{2.19}$$

This equation is invariant under the transformation $x \to -x$. For $\mu < 0$, the only fixed point is $x^* = 0$. At the critical value $\mu_c = 0$, two stable fixed points, $x^* = \pm\sqrt{\mu}$, emerge from the original solution, and $x^* = 0$ loses its stability. The bifurcation diagram is shown in Fig. 2.3 (ii).
In the supercritical case, the cubic term acts to stabilize the system. If the sign of the cubic term is changed, it acts to destabilize the system, resulting in a subcritical

pitchfork bifurcation. The bifurcation diagram for the subcritical case is the inverted version of the supercritical case, with stable parts becoming unstable and vice versa.

2.3.4 SNIPER bifurcation

The term SNIPER bifurcation stands for **S**addle-**N**ode **I**nfinite **Per**iod bifurcation, representing a global bifurcation of limit cycles. An exemplary system displaying a SNIPER bifurcation is given in polar coordinates (r, θ) by the following set of differential equations:

$$\dot{r} = r(1 - r^2), \tag{2.20a}$$
$$\dot{\theta} = \mu - r \sin\theta, \tag{2.20b}$$

where $\mu \geq 0$. Here, r denotes the radial direction and θ represents the angular direction of the system. The corresponding Cartesian coordinates are given by: $x_1 = r\cos\theta$ and $x_2 = r\sin\theta$.
In the radial direction, all trajectories monotonically approach the stable limit cycle at $r^* = 1$, compare with Fig. 2.4 (black circle), except for the trajectory starting from the unstable fixed point at $r^* = 0$.

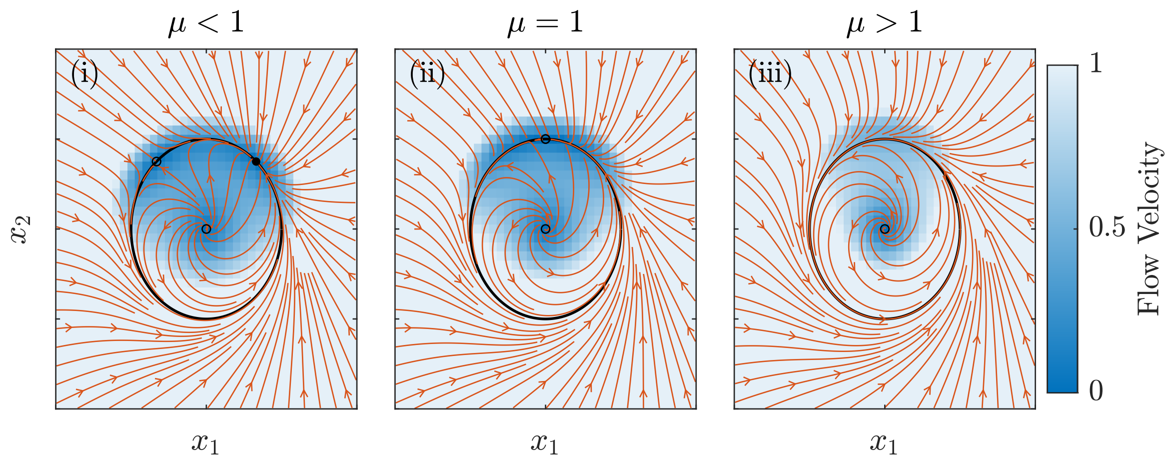

Figure 2.4: Streamline diagram of a SNIPER bifurcation occurring in the system described in Eqs. (2.20a) and (2.20b): (i) below the critical value, (ii) at the critical value and (iii) above the critical value.

The dynamic in the angular component is more complex. For $\mu > 1$, all motion is counterclockwise. As μ decreases, a bottleneck forms at $\theta = \pi/2$, becoming increasingly pronounced as the critical value $\mu_c = 1$ is approached. At this critical point, the period of the cycle T diverges to infinity. When $\mu = 1$, a fixed point emerges on the cycle at the bottleneck location, which then bifurcates into a saddle point and a stable node as μ decreases further. This process is illustrated in Fig. 2.4 (i) - (iii).
The period elongation near the bifurcation point scales as $(\mu - \mu_c)^{-1/2}$, while the amplitude of the oscillation remains of order $\mathcal{O}(1)$. This square-root scaling behavior is a general characteristic of systems near a saddle-node bifurcation.

When the control parameter is varied in the opposite direction, starting from the stable node and saddle point, the fixed points annihilate, leaving behind a saddle-node remnant or "ghost", which induces a slowdown of the period known as a bottleneck [Str15].
Another type of global bifurcation is the homoclinic bifurcation, where a limit cycle moves closer to a saddle point and eventually collides with it, forming a homoclinic orbit. Unlike the SNIPER bifurcation, where the scaling of the period is exponential, in a homoclinic bifurcation the period scales logarithmically. These scaling laws allow us to differentiate between different global bifurcations [Str15].

2.4 Localized States

Localized states (LS) can be characterized as temporal or spatial profiles where an amplitude peak emerges against a uniform background. If the peak is positive, the LS is called bright and if the peak is negative, it is called dark. These structures exhibit a correlation length significantly shorter than the domain size. This classification reveals similarities to classical solitons, a nonlinear phenomenon observed in conserved systems, such as those described by the Korteweg-de Vries equation [KV95] and the nonlinear Schrödinger equation [ZS72].

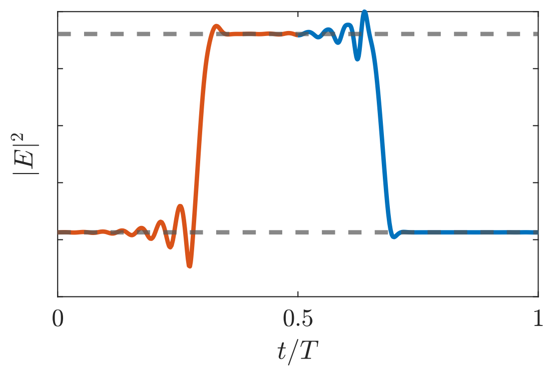

Figure 2.5: Exemplary LS solution of the KGTI, defined in Eqs. (2.25a) and (2.25b), to illustrate domains and locking of domain walls. The intensity levels of the bistable homogeneous solutions are marked with dashed lines.

The existence of LSs is directly linked to the bistability of two distinct states. There are several mechanisms for forming LS, for example:

1. **Homogeneous State Bistability:** The two states are different homogeneous solutions or domains. A pair of fronts can lock through e.g. third-order dispersion and forms a LS, linking their emergence and stability to front propagation or domain wall motion [SJG22].

2. **Homogeneous and Pattern State Bistability:** One state is a homogeneous solution, while the other is a pattern state. In certain scenarios, a piece of a pattern embedded in a homogeneous background can remain stable [Par+21].

In this thesis, only the first case is relevant, as the KGTI system does not support pattern solutions in the studied parameter regime. The locking of two homogeneous solutions is illustrated in Fig. 2.5, where the two domains, marked with dashed lines, represent the bistable homogeneous solutions of the KGTI.

2.4.1 Dissipative Solitons

In a Hamiltonian system, the emergence of a soliton can be attributed to the balance between nonlinear and dispersive effects, which allows for stable propagation with a constant velocity and shape. Specifically, group-velocity dispersion tends to broaden a pulse, while nonlinearity acts to steepen it. A stable soliton arises only when these two opposing effects are precisely balanced. The amplitude or energy of a soliton is not fixed by the system parameters but is instead determined by the initial conditions, resulting in a family of soliton solutions with potentially infinite variations.

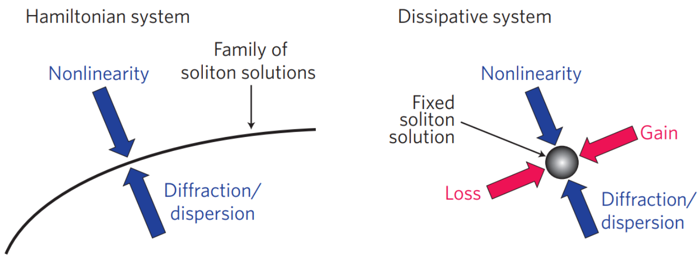

Figure 2.6: Qualitative differences between the solitons in Hamiltonian and dissipative systems, after setting the equation parameters [GA12].

In conservative systems, the phase space volume remains constant over time, ruling out the formation of attractors and fixed points. However, most real-world systems are not conserved. Nevertheless, localized structures in dissipative systems exhibit behaviors similar to conservative solitons. In these systems, such localized wave-like structures are sometimes referred to as dissipative solitons [GA12]. For a dissipative soliton to be stable, a secondary balance between gain and loss must be achieved, in addition to the balance between nonlinearity and dispersion. Fig. 2.6 illustrates these balances for both conservative and dissipative cases.

In optical systems, dissipative solitons manifest themselves as confined wave packets within a nonlinear medium, where their existence and stability critically depend on maintaining energy balance. Unlike conservative systems where soliton characteristics are determined by initial conditions, in dissipative systems, the pulse shape and energy are dictated by the system's attractors, which are predefined by the chosen parameter set. The stability of a dissipative soliton is directly linked to the stability of the corresponding attractor. A strong attractors provides high stability. Despite the predetermined profile shape, varying parameters can yield a diverse array of profiles and solutions through smooth transformations or bifurcations. For instance, a fixed point may evolve into a limit cycle, and bifurcations can lead to chaotic soliton dynamics [GA12]. Thus, bifurcation analysis serves as a valuable tool for tracking solutions through parameter space.

Nonlinear optical setups are particularly well-suited for studying pattern formation and the creation of localized structures. One method to introduce optical nonlinearity is by incorporating a medium exhibiting a strong optical Kerr effect [OTL11; Ode+14]. In nonlinear optics pattern formation in the temporal domain are especially interesting, where systems often display fast and slow time scales, analogous to spatial and temporal dimensions in spatially extended systems [Lug+18; HTW92]. Group-velocity dispersion facilitates the space-like interaction [LPB15] balanced with the Kerr effect. The second balance is given by losses and gain. In practical optical setups, loss is inevitable due to imperfect mirror reflectivities or necessary experimental detection, whereas gain is provided by external sources such as optical or electrical pumping [LPB15].

2.4.2 Two-Time Representation

In systems with long time delays, the resulting dynamics unfold on different time scales [Are+92; GP96]. To represent these dynamics, each point in time can be expressed as $t = \theta T + \sigma$, where T represents a characteristic period (e.g., the delay time of the system, the period of a pulse, or the period of external forcing), $\theta \in \mathbb{N}$ counts the number of elapsed periods, and σ is the remainder describing the time in one round trip [Are+92].

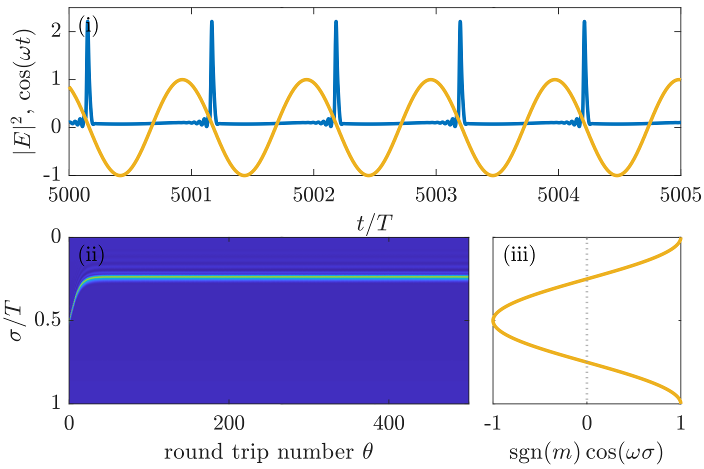

Figure 2.7: (i) Exemplary zoom into a time trace (blue) with phase modulation (yellow) and (ii) corresponding two-time representation in the synchronized case of the phase modulated KGTI described in Eqs. (2.25a) and (2.28). (iii) shows one period of the phase modulation in the fast time scale σ. The vertical axes of (ii) and (iii) align.

Geometrically, this temporal decomposition can be visualized by slicing the time trace into segments of length T and stacking them. Fig. 2.7 illustrates this process. The upper panel shows the original time trace, while the lower panel displays the stacked slices in a two-time diagram. Each slice aligns with the periodic forcing indicated by the yellow curve. The term *round trip* refers to a time interval of size τ, corresponding to the delay a pulse accumulates by traveling through the external cavity.

As depicted in Fig. 2.7, the resulting two-time diagram of a delayed system exhibits similarities to spatially extended systems [Are+92]. Here, the discrete variable θ counts the round trips and can be interpreted as a time-like variable describing the system's evolution over multiple periods (e.g., many round trips). Meanwhile, σ acts as a space-like variable describing the fast dynamics occurring within a single period. This representation of the time-delayed system clarifies purely temporal dynamics across different time scales, allowing comparisons to one-dimensional spatially extended systems and revealing phenomena such as coarsening and drift [YG17]. Moreover, it is easier to track dynamics on thousands of round trips than in endlessly long time traces. In this framework, periodic solutions of purely temporal dynamics of time-delayed systems correspond to steady states in the two-time representation. For systems with multiple delays, the corresponding space-time representation expands to include multiple spatial dimensions [YG14].

2.5 The KGTI

This thesis deals with the analysis of a vertical external-cavity delayed Kerr Gires-Tournois interferometer with injection (KGTI) known from various previous works [Sch+19; SJG22]. The setup is shown in Fig. 2.8. Additionally, we will introduce phase modulation to the system.

2.5.1 Setup and System Derivation

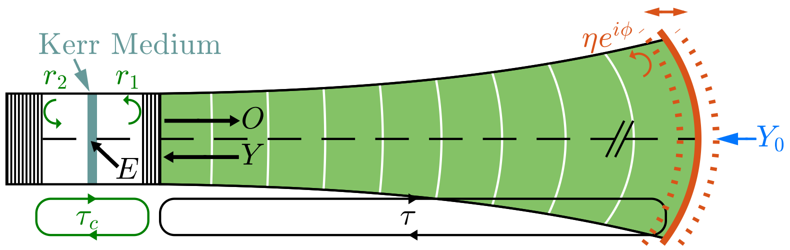

Figure 2.8: Schematic of the KGTI. A micro-cavity with round trip time τ_c containing a Kerr medium is coupled to a long external cavity with round trip τ that is closed by a mirror with reflectivity η. Due to the reflection at the external mirror the fields gain an additional phase of ϕ. Through the external mirror a monomode injection field with amplitude Y_0 is introduced to the setup. In orange the periodic movement of the external mirror is indicated.

The system consists of two coupled cavities. First, a microcavity (white) containing a Kerr medium which is a few micrometers long and has a round trip time τ_c. Second, a cavity (green) which is a few centimeters long, called the external cavity, with round trip time $\tau \gg \tau_c$. The external cavity is closed by a feedback mirror with feedback phase ϕ and reflectivity η which determines the strength of the feedback. The microcavity is enclosed by two distributed Bragg mirrors with reflectivities $r_{1,2}$. The resulting light coupling efficiency h of the two cavities is given by

$$h = \frac{(1 + |r_2|)\,(1 - |r_1|)}{(1 - |r_1|\,|r_2|)}. \tag{2.21}$$

For a perfect bottom mirror $|r_2| = 1$ the coupling efficiency is $h = 2$, which corresponds to the so-called Gires-Tournois interferometer regime.
The whole setup is subject to external monomode injection with amplitude Y_0 introduced through the external mirror. The difference between the microcavity resonance and the injection frequency $\delta = \omega_\mathrm{c} - \omega_0$ is called the detuning. With this detuned injection the system loses its phase invariance. The time evolution is described by the microcavity field E, the external cavity field Y and the output field O. We chose to only describe the slowly varying field envelopes with E, Y and O since the fast modes within can easily be reconstructed with the frequency ω_0.
The output of the microcavity, defined as

$$O(t) = E(t) - Y(t), \tag{2.22}$$

propagates through the external cavity and gains an additional phase due to reflection at the external mirror and due to the propagation. This additional phase is collected in

$$\varphi_0 = \phi + \omega_0 \tau. \tag{2.23}$$

After one round trip, of duration τ through the external cavity the output is reinserted into the microcavity. Hence, the microcavity input consists of the reflected output from the previous round trip $\eta e^{i\varphi_0} O\left(t - \tau\right)$ and the injection Y_0. This significant round trip time τ in the external cavity introduces dynamics that evolve on two time scales.
The external cavity field $Y(t)$ which is inserted into the microcavity with the light coupling efficiency h acts as a pumping for the microcavity field E. Inside the microcavity, the Kerr nonlinearity causes an effective detuning of

$$\theta = \delta - |E|^2. \tag{2.24}$$

In summary, we can write the injected KGTI as

$$\dot{E}(t) = \left[-1 + i\left(|E(t)|^2 - \delta\right)\right] E(t) + hY(t) \tag{2.25a}$$

$$Y(t) = \eta e^{i\varphi_0} \left[E(t-\tau) - Y(t-\tau)\right] + \sqrt{1-\eta^2} Y_0. \tag{2.25b}$$

Additionally, for this thesis the well established KGTI system is extended with a periodically modulated effective feedback phase. There are several ways to include phase modulation into the setup. One way is moving the feedback mirror back and forth, changing the delay τ by a small amount:

$$\tau(t) = \tau_0 + \Delta\tau(t), \tag{2.26}$$

where τ_0 is the original delay induced by the unchanged external cavity and $\Delta\tau(t)$ the change in the external cavity delay caused by the periodic movement of the external mirror.
For the effective feedback phase, defined in Eq. (2.23), we have to accommodate for the change of the external cavity delay. Due to the high frequency ω_0, the phase changes by a non-negligible amount. To include the time dependence into the feedback phase we write

$$\varphi(t) = \phi + \omega_0(\tau + \Delta\tau(t)) = \varphi_0 + m\cos(\omega t). \tag{2.27}$$

We can rewrite the equation in this way, since we only focus on cosine-like phase modulation. From this follows $\Delta\tau = m/\omega_0$ is small, since $\omega_0 \gg 1$.
Another way to incorporate phase modulation is periodically changing the frequency of the injection beam, causing a similar effect. The specific method used to create the phase modulation does not affect the right-hand side of Eq. (2.27), ensuring that our results are not limited to any particular mechanism used to produce the phase modulation. The second equation extended with the phase modulation reads

$$Y(t) = \eta e^{i(\varphi_0 + m\cos(\omega t))}\left[E(t-\tau) - Y(t-\tau)\right] + \sqrt{1-\eta^2}Y_0. \tag{2.28}$$

This approach is implemented in the numerical analysis of this thesis, allowing for general applicability across various phase modulation techniques.
This equation contains no time derivative of $Y(t)$ and can therefore be interpreted as an algebraic constraint, called a delay algebraic equation (DAE) while the first equation is an ODE. The equation for $Y(t)$ can be inserted into the first equation yielding the dependence of $\dot{E}(t)$ on the delayed quantities $Y(t-\tau)$ and $E(t-\tau)$. Repeated insertion of the algebraic constraint leads to a dependence of the current state on all previous round trips which is especially strong for a high reflection coefficient η.

2.5.2 Solution of the KGTI without Phase Modulation

In this thesis we will only study the normal dispersion regime, meaning we always choose $\delta > 0$. The continuous wave (CW) solutions of the system without phase modulation are steady states of the form $E(t) = \tilde{E}$ and $Y(t) = \tilde{Y}$. The frequency is locked to the injection Y_0, resulting in only a constant phase shift between the CW solution and the injection Y_0. Using this ansatz, the relationship between the injection Y_0 and the intensity of the microcavity field $I_\mathrm{s} = |\tilde{E}|^2$ can be expressed as

$$|Y_0|^2 = \frac{\eta^2\left(h^2 - 2h\right) + \left[1 + 2\eta\cos\varphi_0 + \eta^2\right]\left[1 + (\delta + I_\mathrm{s})^2\right] - 2h\eta\left[\cos\varphi_0 - (\delta - I_\mathrm{s})\sin\varphi_0\right]}{h^2\left(1-\eta^2\right)} I_\mathrm{s} \tag{2.29}$$

which reduces for $\varphi_0 = 0$ to

$$Y_0^2 = \frac{k^2 + (I_\mathrm{s} - \delta)^2}{h^2\frac{1-\eta}{1+\eta}} I_\mathrm{s}, \tag{2.30}$$

with $k = (1 + [1-h]\eta)/(1+\eta)$ [SJG22].
Since the system is of third order in E, optical bistability can occur within certain parameter ranges, which is generally the case in this work. The CW solution forms a S-shaped curve when the integrated intensity $\langle |E|^2 \rangle$ is plotted in black in Fig. 2.9 against the injection Y_0, while keeping all other parameters constant. The branch exhibits two folds, leading to a bistability range between high and low intensity levels with a uniformly unstable connection. This bistability of homogeneous states lays the foundation for the occurrence of TLS in a normal dispersion regime.
TLS in the normal dispersion regime of the KGTI, without phase modulation, form via fronts connecting homogeneous states. Due to third-order dispersion, these connecting

fronts exhibit oscillatory tails, as shown in Fig. 2.5, which cause the fronts to lock at discrete distances, leading to a variety of pulse shapes [Sch+19]. Because the domain walls can lock only at discrete distances, the corresponding TLS lie on a snaking branch structure, ranging from bright to dark pulses, as depicted in Fig. 2.9.
The interaction between the fronts, due to third-order dispersion, locks the drifting fronts at specific injection ranges for different distances, resulting in collapsed snaking around the Maxwell line. At the Maxwell line, $Y_{0,\mathrm{MP}} \approx 0.61$, the interacting fronts have the same speed, and their relative dynamics are arrested [SJG22]. The TLS branch emerges from the CW branch through a subcritical Andronov-Hopf bifurcation. The corresponding branch, obtained via continuation, is shown in Fig. 2.9. The y-axis represents the integrated intensity $\langle |E|^2 \rangle$, which provides a clear separation between the windings of the snaking branch. Other measures, such as the maximum or minimum measure, do not offer this level of separation.

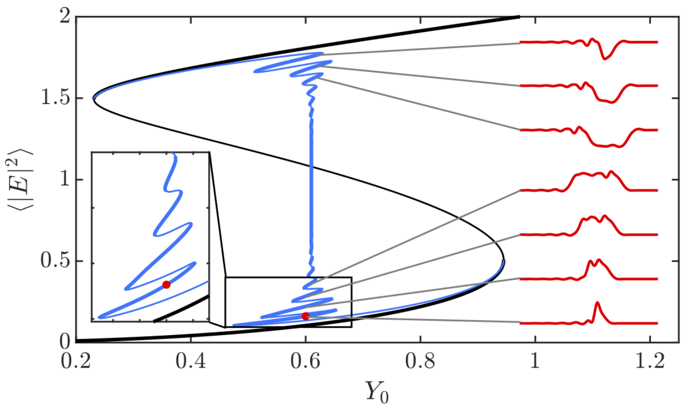

Figure 2.9: Bifurcation diagram of the KGTI without phase modulation, as in Eqs. (2.25a) and (2.25b). The CW and the TLS branch are depicted in black and blue, respectively. Thick (thin) lines represent stable (unstable) solutions, respectively. In red, the solution profiles of the indicated points are shown. The parameters are $\delta = 1.5$, $h = 2$, $\eta = 0.75$, $\varphi_0 = 0$ and $\tau = 100$ [SJG22].

TLS occur with a fixed period that depends on the pulse shape, specifically the locking distance of the domain walls. Due to causality, this period must always be larger than the delay τ. If the two-time diagram is scaled with the delay τ, this effect appears as a small drift of the TLS. In the long delay limit, this drift approaches an asymptotic value, meaning that while the period and τ grow to infinity, their difference remains constant [YG17].

2.5.3 Lugiato-Lefever Equation

In the DAE model (2.25a) and (2.28), the role of third-order dispersion (TOD) and group-delay dispersion (GDD) are not distinguishable. However, a multiple time scale analysis of the DAE in the uniform field limit reveals a PDE that intuitively describes the dependencies of TOD and GDD on system parameters. The TOD coefficient depends on the reflectivity η and the light coupling efficiency h. In the good cavity limit, the GDD coefficient is small compared to the coefficient of the TOD, and the cavity's

dynamics are mostly controlled by TOD, which explains the strong oscillatory tails for η close to one [SJG22].
This regime is marked by small cavity losses and weak injection, i.e. $\eta \approx 1$ and $\tilde{\varphi}$ has to be in the same order of magnitude as η differs from one.
In this regime, a multiscale analysis of the KGTI leads to the Lugiato-Lefever equation [SGJ22]:

$$\left(i\partial_\theta + \tilde{\varphi} + iv\partial_\sigma - \frac{\beta_2}{2}\partial_\sigma^2 - i\frac{\beta_3}{6}\partial_\sigma^3 + \gamma|A|^2\right) A = F(A), \tag{2.31}$$

where $F(A) = i(\eta-1)A + iY_0\sqrt{8(1-\eta)}/(1+i\delta)$ contains losses and injection. The coefficients $v = 2/(1+\delta^2)$, $\beta_2 = 4\delta/(1+\delta^2)^2$, $\beta_3 = 4(3\delta^2-1)/(1+\delta^2)^3$ and $\gamma = 2/(1+\delta^2)$ determine the amount of second- and third-order dispersion, as well as nonlinearity [SGJ22]. The effective round trip phase is $\tilde{\varphi} = \varphi_0 - 2\arctan\delta \mod 2\pi$. For a sufficiently small phase modulation we can use the same results and just swap the constant φ_0 for the modulated feedback phase $\varphi(t)$ afterwards. The shape of the LLE corresponds to a driven, damped and detuned NLSE [Lug+18] with third-order dispersion. In this limit and in the presence of phase modulation, the phase $\tilde{\varphi}$ becomes time-dependent, introducing a periodic potential, similar to the potential in the Gross–Pitaevskii equation.
The LLE is one of the first models to describe pattern formation specifically in nonlinear optics and was proposed in 1987 by L. Lugiato and R. Lefever [LL87]. It is often interpreted as an extended, dissipative version of the NLSE with additional terms describing optical injection, losses and detuning.
While the original LLE accounts for spatial variations in optical resonators in the transverse direction, a temporal (longitudinal) version emerges when spatial (transversal) variations are negligible compared to temporal dynamics, as seen in optical fiber systems. This transition was performed by Haelterman et al. [HTW92]. A major step in this transition was to replace diffraction by group-velocity dispersion. This temporal version of the LLE regained attention when Del'Haye et al. [Del+07] demonstrated that microresonators equipped with a Kerr nonlinearity are suitable for the generation of optical frequency combs.
In summary, the LLE is able to describe various optical systems, from pattern formation and soliton dynamics to frequency comb generation and will be therefore the starting point of our analysis. It is important to note, while the LLE can describe the model quite well in the given limit, however, we still simulate the full model, in the described parameter range.

2.6 Synchronization and Arnold Tongues

Synchronization is a fundamental concept in nonlinear science, widely observed and utilized across various systems. Generally, synchronization refers to the adjustment of frequencies of oscillators due to weak interaction [PRK01]. This section is based on the work presented in [PRK01].
The phenomenon was first described by Christiaan Huygens in the 17TH century [OM15], who observed the synchronization of two pendulum clocks hanging from the

same support. To create a system capable of synchronization, self-sustained oscillators are required. A self-sustained oscillator is an active system, meaning it contains an internal energy source and is described as an autonomous system. The form of oscillation must depend solely on the system's parameters, independent of how the oscillation is initiated, and the oscillation must be stable against small perturbations. Examples of self-sustained oscillators include lasers, oscillatory chemical reactions like the Belousov-Zhabotinsky reaction, pacemakers in human hearts, and electronic circuits for generating radio-frequency power [PRK01].
For the synchronization of two self-sustained oscillators, a second oscillator that interacts with a first one is needed, implying that the oscillators are coupled. In Huygens' case, the two pendulum clocks were mounted on the same support beam, creating a coupling that allowed small forces to act between the clocks. If the pendulums have a small difference in frequency, known as detuning, the weak coupling will lead to synchronization of the two clocks, eliminating the frequency difference. The two pendulums can swing either in-phase or anti-phase.
In general, synchronization marks the onset of a specific relationship between the phases of oscillators, known as phase locking. If the coupling is too weak and/or the detuning is too large, the oscillators will not synchronize. Understanding these dynamics is crucial for applications ranging from biological rhythms to communication technologies and chemical oscillations.

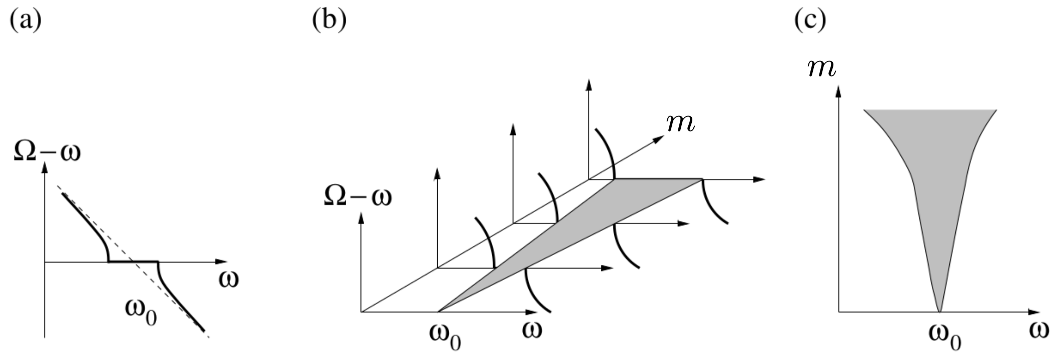

Figure 2.10: (a) Detuning of the driven Ω and driving oscillator ω as a function of ω. (b) Family of $\Omega - \omega$ for various driving amplitudes m. (c) Synchronization region known as *Arnold tongue* in the (ω, m)-pane. Adapted from [PRK01].

In this thesis, we focus on the unidirectional coupling between two oscillators. A modern example of this concept is a radio-controlled watch. Specifically, the thesis examines the synchronization of a periodic oscillator (the KGTI) by an external force (the periodic phase modulation). The injected KGTI produces TLSs with a certain period T or frequency $\Omega = 2\pi/T$, forming a self-sustained oscillator. This analysis explores the impact of an external periodic potential on the behavior of TLSs in the KGTI system.
An external force is applied in the form of periodically shifting the outer mirror back and forth with the frequency ω, thus periodically increasing and decreasing the delay time τ by a small amount and causing a modulated feedback phase for the fields going back into the cavity. This is the second self-sustained oscillator coupled unidirectionally to the first one. The modulated feedback phase is $\varphi = \varphi_0 + m\cos(\omega t)$, hence the

amplitude of the forcing is m. For small detunings $(\Omega-\omega)$, the oscillators synchronize, i.e., the frequency Ω of the TLS becomes equal to ω. If the detuning exceeds a critical value, the synchronization breaks down.
In Fig. 2.10 (a), the detuning $\Omega-\omega$ is plotted in dependence on the driving frequency ω. The bandwidth where the detuning vanishes is the synchronization region. In part (b) of Fig. 2.10, a third axis is added, displaying the modulation amplitude m. In this three-dimensional plot, the synchronization region becomes an area (gray) called the *Arnold tongue* or synchronization region, where the frequencies are locked, a concept also known as mode locking in laser physics.
As m increases, the tongue widens, and as m decreases, it narrows. For vanishing m, the tongue touches the ω-axis at the value of ω_0, the natural frequency of the forced system. The third part of Fig. 2.10 displays the plane defined by $\Omega-\omega=0$, where the Arnold tongue is located.
If either the detuning is too large or the force is too strong, the forced oscillator cannot be synchronized by the other oscillator. However, the forced oscillator feels the forcing and displays non-uniform motion. The oscillations are periodically accelerated and decelerated, but the interaction can never fully entrain one oscillator to the other. This periodic change manifests as a beating with period T_{beat}.

2.7 Numerical Methods

In nonlinear physics, most systems cannot be solved analytically, meaning there is no closed-form solution for nonlinear equations. One of the main challenges in solving nonlinear systems analytically is the principle of superposition, which applies to linear systems but not to nonlinear ones. Consequently, numerical methods are essential for studying nonlinear systems and approximating solutions. Thus, numerical methods are fundamental to the study of nonlinear physics and DDEs. Furthermore, the numerical tool `DDE-Biftool` [ELR02; Sie+16] uses discrete fields, making discretization unavoidable. `DDE-Biftool` is a tool for the numerical continuation of solutions to DDE which is used extensively in this thesis. By discretizing, the number of degrees of freedom is reduced from infinity to the number of sample points within one delay.

2.7.1 Direct Numerical Simulation

Due to the nonlinear nature of our system, we must employ numerical methods. A straightforward algorithm to compute the time evolution of a DDE is Euler's method. Combined with an initial condition, this forms an initial value problem, where time integration reveals the system's behavior over time starting from the initial condition. For a one-dimensional system f with a single delay τ,

$$\dot{x}(t)=f(x(t),x(t-\tau),t), \tag{2.32}$$

the time step Δt is chosen such that $\tau/\Delta t=N\in\mathbb{N}$. This choice ensures that we can use the same discretization points without needing to interpolate between nodes when accessing the time trace for the delayed terms. Then, the discrete time can be written as $t=n\Delta t=t_n$, where $n\in\mathbb{N}$. An initial condition must be defined for an interval of length τ, meaning the initial condition is a discrete function $x_0(s)$, where $s \in \{-\tau, -\tau + \Delta t, \ldots, -\Delta t, 0\}$. Euler's method samples the derivative of x once every time step, by evaluating the right-hand side of our system, and assumes it is constant between samples. With the shorthand notation $x(t_n) = x_n$, Euler's method can be formulated as

$$x_{n+1} = x_n + \Delta t \cdot f(x_n, x_{n-N}, t_n). \tag{2.33}$$

This algorithm corresponds to a first-order expansion, leading to a local truncation error of order $\mathcal{O}(\Delta t^2)$ and a global truncation error (over the entire integration interval) of $\mathcal{O}(\Delta t)$. Other methods, such as Runge-Kutta methods, use multiple weighted sampling points per time step and can achieve smaller local and global truncation errors [Gur22]. Nonetheless, for this thesis, we consider an semi-implicit scheme.
For the KGTI system, starting from the Eqs. (2.25a) and (2.28)

$$\begin{aligned}
\dot{E}(t) &= \left[-1 + i\left(|E(t)|^2 - \delta\right)\right] E(t) + hY(t) \\
Y(t) &= \eta e^{i(\varphi_0 + m\cos(\omega t))} \left[E(t-\tau) - Y(t-\tau)\right] + \sqrt{1-\eta^2} Y_0,
\end{aligned}$$

we rewrite $\dot{E}$ as the difference between neighboring sampling points with the abbreviation $\mathcal{L}_n = -1 + i\left(|E_n|^2 - \delta\right)$. The first equation becomes

$$\begin{aligned}
&& \frac{E_{n+1} - E_n}{\Delta t} &= \mathcal{L}_n E_n + hY_n \\
\Leftrightarrow && E_{n+1} &= E_n + \Delta t\left(\mathcal{L}_n E_n + hY_n\right)
\end{aligned}$$

To increase the accuracy of this algorithm, the sampling points are replaced with the average of sampling points at times t_n and t_{n+1}, making this scheme semi-implicit:

$$E_{n+1} = E_n + \Delta t\left(\mathcal{L}_n \frac{E_n + E_{n+1}}{2} + h\frac{Y_n + Y_{n+1}}{2}\right). \tag{2.35}$$

Solving for E_{n+1} gives the update equation:

$$E_{n+1} = \frac{1}{1 - \frac{\Delta t}{2}\mathcal{L}_n}\left[\left(1 + \frac{\Delta t}{2}\mathcal{L}_n\right) E_n + \frac{\Delta t}{2} h\left(Y_n + Y_{n+1}\right)\right]. \tag{2.36}$$

For the second equation, defining $N = \tau/\Delta t \in \mathbb{N}$, it can be rewritten in discrete form as:

$$Y_{n+1} = \eta e^{i(\varphi_0 + m\cos(\omega t_n))}\left(E_{n-N} - Y_{n-N}\right) + \sqrt{1-\eta^2} Y_0. \tag{2.37}$$

This is the semi-implicit Euler scheme used for the direct numerical simulations (DNS) in this thesis. Since this scheme has already been implemented for the system without phase modulation, the majority of the code is adapted and extended to include the modulated feedback phase. This modification renders the system non-autonomous. Additional parameters are introduced to account for ω and m.

2.7.2 Numerical Continuation

Numerical path-continuation is a method that enables the tracking of both stable and unstable solutions through parameter space in multistable regimes. Unlike direct numerical simulation (DNS), which starts from an initial condition and converges to a

stable solution, continuation begins with a known solution and follows it through parameter space, even if the solution becomes unstable. At bifurcation points, emerging solutions can be followed. This technique allows for a systematic exploration of solutions in the parameter space of a given system, e.g. steady states, periodic solutions, and bifurcation points. Offering greater control and insight compared to direct time integration.
This section is based on the work presented in [Thi21].
Consider a solution $(\boldsymbol{x}_0^*, \mu_0)$ to the system $\dot{\boldsymbol{x}} = \boldsymbol{F}(\boldsymbol{x}, \mu)$, where μ is a control parameter and the continuation parameter of our choice. The continuation parameter μ is varied to trace the solution branch $\boldsymbol{x}^*(\mu)$. A initial solution $\boldsymbol{x}_0^*$ can be obtained from methods like DNSs.
Starting from $\boldsymbol{x}_0^*$, an initial guess for the next solution at $\mu_1 = \mu_0 + \Delta\mu$ is calculated using the tangent of the curve $\boldsymbol{x}^*(\mu)$ at $(\boldsymbol{x}_0^*, \mu_0)$. For a small step $\Delta\mu$:

$$\boldsymbol{x}_1^{*(0)} = \boldsymbol{x}_0^* + \Delta\mu \left.\frac{\partial \boldsymbol{x}^*}{\partial \mu}\right|_{(\boldsymbol{x}_0^*, \mu_0)} \tag{2.38}$$

The tangent direction can be evaluated from differentiating $0 = \boldsymbol{F}(\boldsymbol{x}^*(\mu), \mu)$:

$$\begin{aligned} 0 &= \left[\frac{\partial \boldsymbol{F}}{\partial \boldsymbol{x}}\frac{\partial \boldsymbol{x}}{\partial \mu} + \frac{\partial \boldsymbol{F}}{\partial \mu}\right]_{(\boldsymbol{x}_0^*, \mu_0)} \\ \iff \qquad \left.\frac{\partial \boldsymbol{x}}{\partial \mu}\right|_{(\boldsymbol{x}_0^*, \mu_0)} &= -\left[\left(\frac{\partial \boldsymbol{F}}{\partial \boldsymbol{x}}\right)^{-1}\frac{\partial \boldsymbol{F}}{\partial \mu}\right]_{(\boldsymbol{x}_0^*, \mu_0)} \end{aligned}$$

Since the initial approximation $\boldsymbol{x}_1^{*(0)}$ is linear, significant errors are expected, and $\boldsymbol{F}(\boldsymbol{x}^{*(0)}(\mu), \mu) = 0$ is likely not satisfied. Therefore, Newton's method is used to iteratively refine the solution:

$$\boldsymbol{x}_1^{*(n+1)} = \boldsymbol{x}_1^{*(n)} - \left.\left(\frac{\partial \boldsymbol{F}}{\partial \boldsymbol{x}}\right)^{-1}\right|_{(\boldsymbol{x}_1^{*(n)}, \mu_0)} \boldsymbol{F}\left(\boldsymbol{x}_1^{*(n)}\right) \tag{2.39}$$

This iterative scheme starts with the initial guess $\boldsymbol{x}_1^{*(0)}$. Once the scheme achieves sufficient accuracy, the control parameter is incremented again to $\mu_2 = \mu_1 + \Delta\mu$, and the process is repeated to trace the solution branch.
However, this algorithm encounters difficulties near fold bifurcations, where increasing the control parameter leads to regions without solutions (see section 2.3.1). To address this, a pseudo-arclength continuation method is implemented. The arclength s, locally approximated using the Pythagorean theorem

$$|\boldsymbol{x}^*|^2 + (\Delta\mu)^2 = (\Delta s)^2, \tag{2.40}$$

is used as the new control parameter, with μ considered part of the extended solution $\boldsymbol{y}^* = (\boldsymbol{x}^*, \mu)$. From Eq. (2.40) the constraint

$$p(\boldsymbol{x}^*, \mu, s) = |\boldsymbol{x}^*|^2 + (\Delta\mu)^2 - (\Delta s)^2 \tag{2.41}$$

follows and supplements the system. At the roots of $p(\boldsymbol{x}^*, \mu, s)$ the Pythagorean theorem for the arc length is fulfilled. Thus, we write the extended system:

$$\boldsymbol{E}(\boldsymbol{y}^*, s) = \begin{pmatrix} \boldsymbol{F}(\boldsymbol{x}^*, \mu) \\ p(\boldsymbol{x}^*, \mu, s) \end{pmatrix}. \tag{2.42}$$

Using Newton's method, roots of both $\boldsymbol{E}(\boldsymbol{y}, s) = 0$ and $\boldsymbol{F}(\boldsymbol{x}, \mu) = 0$ are found. More details can be found in [Thi21]. Pseudo-arclength continuation is crucial for this thesis, as the solutions exhibit numerous folds in parameter space, mostly in the form of snaking.
The Matlab program `DDE-Biftool` [Sie+16; ELR02], designed for DDEs, is utilized for the continuations in this thesis. To address the delay-algebraic nature of the KGTI while using `DDE-Biftool`, a recently developed extension is used [HGJ21]. This extension allows the use of a mass matrix, see Eq. (2.4).
Additionally, the existing system, without phase modulation, is extended by an additional real field for the time dependence inside the cosine. We define in Eq. (2.28) for the argument of the cosine:

$$G(t) = \omega t \tag{2.43}$$

and therefore, the additional derivative to include to the symbolic functions in the continuation program `DDE-Biftool` is simply

$$\frac{\mathrm{d}G}{\mathrm{d}t} = \omega. \tag{2.44}$$

Since $G(t)$ would not be periodic on its own it would be impossible to implement this additional field for periodic solutions in `DEE-Biftool`. Therefore the boundary conditions of this field are take modulus 2π. Moreover, the definition of the field Y is extended with the phase modulation using the definition in Eq. (2.43) for the argument of the cosine.
Finally, for the implementation in `DDE-Biftool` we have the following set of equations:

$$\boldsymbol{M}\dot{\boldsymbol{x}} = \begin{pmatrix} \mathrm{d}E/\mathrm{d}t \\ 0 \\ \mathrm{d}G/\mathrm{d}t \end{pmatrix} = \begin{pmatrix} \left[-1 + i\left(|E(t)|^2 - \delta\right)\right] E(t) + hY(t) \\ \eta e^{i[\varphi_0 + m\cos(G(t))]}\left[E(t-\tau) - Y(t-\tau)\right] + \sqrt{1-\eta^2}Y_0 - Y(t) \\ \omega \end{pmatrix} \tag{2.45}$$

with the mass matrix $\boldsymbol{M}$ defined as

$$\boldsymbol{M} = \begin{pmatrix} 1 & 0 & 0 \\ 0 & 0 & 0 \\ 0 & 0 & 1 \end{pmatrix} \tag{2.46}$$

removing the derivative in Y from the equation. In the real implementation the complex fields E and Y are split into real and imaginary parts, however for the sake of readability we left this step out in this presentation.

3 The Influence of Phase Modulation

Throughout this thesis, the study of the KGTI with a modulated feedback phase can be approached from two perspectives. First, it can be treated as a standard synchronization problem involving two self-sustained oscillators with unidirectional coupling. Alternatively, the coupled system can be viewed as a single entity, with its synchronized solutions seen as periodic orbits. We will employ methods from both approaches to achieve a comprehensive understanding of the system in question.

3.1 Synchronization

In general, the phase-modulated KGTI, defined in Eqs. (2.25a) and (2.28), exhibits two fundamental dynamics. The first involves the synchronization of the pulse frequency to the phase modulation. In this scenario, there is precisely one pulse per modulation period $T = 2\pi/\omega$, and, after a transitional phase, the pulse consistently occurs at the same point within each period.
The second scenario is the unsynchronized state. Here, the modulation frequency ω deviates to much from the natural frequency of the pulses ω_0. A stronger modulation, i.e. increasing m, would be able to enslave the pulses to the periodicity of the phase modulation. However, the amplitude of the modulation is too small to fully entrain the pulses to the driving frequency. Despite this, the TLSs still respond to the modulation, resulting in non-uniform motion. Depending on the amplitude of the phase modulation, the pulses either accelerate or decelerate. In the two-time representation (see Fig. 3.1), scaled with the period $T = 2\pi/\omega$ of the phase modulation, the forcing causes the pulse to periodically propagate through the σ-direction with a modulated velocity. This dynamic is characterized by two frequencies: the frequency of the phase modulation ω and the frequency of the periodic movement through the σ-dimension, referred to as the *beat frequency* Ω_{beat}. The interaction of these two frequencies produces a quasi-periodic motion.
For the unsynchronized case, we can have two cases. A real quasi-periodic motion would be present if the two frequencies ω and Ω_{beat} are incommensurable. This is a kind of dynamics which `DDE-Biftool` cannot capture. If ω and Ω_{beat} are whole-numbered multiples of each other then, in reality, we have some periodic dynamics. Nevertheless, this only occurs in a few cases and the corresponding period would be too long for an efficient continuation. Therefore we rely on numerical integration to study quasi-periodic dynamics. To determine Ω_{beat}, we use a center of mass algorithm,

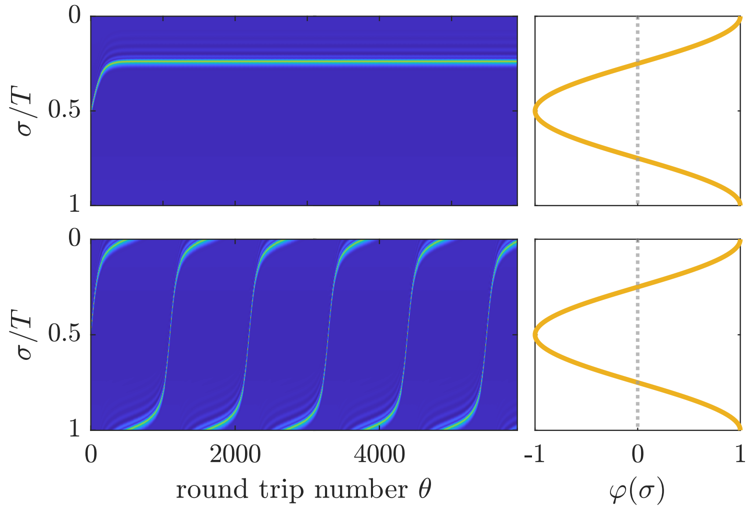

Figure 3.1: Examples for the synchronized and unsynchronized dynamics of the KGTI with periodic phase modulation in two-time representations scaled to the period $T = 2\pi/\omega$ of the phase modulation. The upper row shows the synchronized case of a single pulse with $\omega = 0.0619$ and the lower row shows the unsynchronized case where the frequency of the forcing is changed to $\omega = 0.0618125$. The other parameters are $\delta = 1.5$, $h = 2$, $\eta = 0.75$, $\varphi_0 = 0$, $m = 0.12$, $Y_0 = 0.55$ and $\tau = 100$. The panels on the right indicate the phase modulation as in Fig. 2.7.

see Chapter 3.4.3 for more details, which identifies the points where the pulse leaves the σ-axis on one side and reappears on the other side, determining the corresponding period.
In the synchronized case, where the dynamics exhibit a single period, the solution can be analyzed using `DDE-Biftool`. This tool also provides the period of the resulting periodic orbit as part of the solution branches.

3.1.1 Arnold Tongue

In general, synchronization depends on two key parameters: the frequency of the phase modulation ω and the coupling strength between the oscillators. In our study, the amplitude of the phase modulation m represents the coupling strength. To examine how synchronization varies with these parameters, we follow the approach outlined in Section 2.6.
First, the detuning between the frequency of the pulses Ω and the modulation frequency ω as a function of the frequency ω is plotted in Fig. 3.2 (i). On the x-axis, the modulation frequency ω is scaled with the natural frequency of the periodic orbit corresponding to the TLS without phase modulation ω_0. The y-axis shows the detuning between the frequency of the periodic orbits Ω and the modulation frequency ω. The blue dots represents data calculated from direct numerical simulations (DNSs). It is evident that within a small range around ω_0, the detuning vanishes, indicating synchronization in this region. In this synchronization region, the periodic orbit can be continued using `DDE-Biftool`. The corresponding curve is plotted in orange and forms a very narrow loop, bounded by fold bifurcations at both ends.

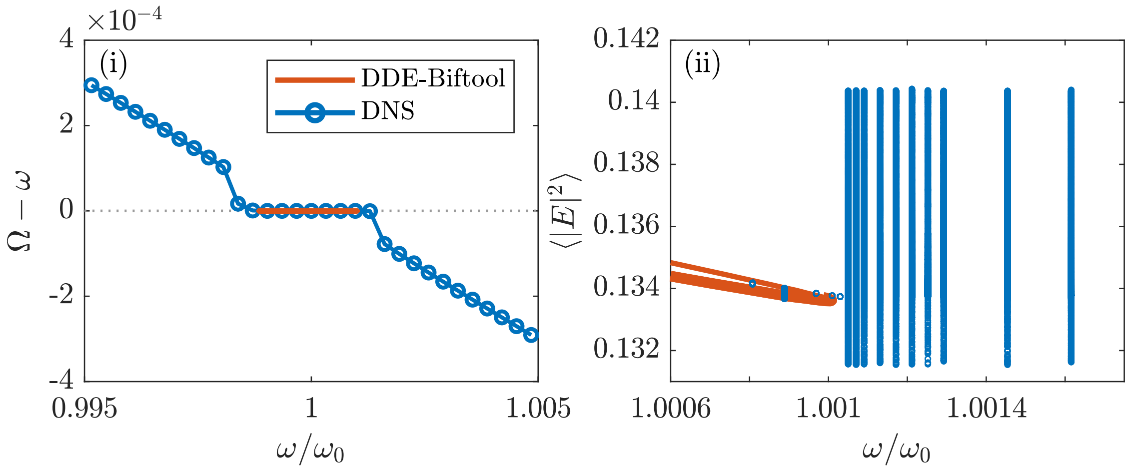

Figure 3.2: (i) Detuning of the periodic orbit of a TLS, with frequency Ω, and the periodic phase modulation frequency ω as a function of ω. The amplitude of the modulation is $m = 0.12$. In blue, we show the detuning determined via DNS and in orange the synchronization region determined using `DDE-Biftool`. The other parameters are as in Fig. 3.1. The frequencies ω are scaled with the natural frequency ω_0 of the TLS without phase modulation. (ii) shows the same `DDE-Biftool` continuation plotted with the integrated intensity measure, focusing on the fold bifurcation on the right side, in orange. In blue, we show the integrated intensities with each circle for various round trips, crossing over to the unsynchronized state.

In Fig. 3.2 (ii), we focus on the fold bifurcation point on the loop's right side. Here, the fold becomes visible in the integrated intensity measure. The blue dots represent the integrated intensities of single round trips, determined from DNS. This allows us to extend the diagram into the quasi-periodic regime, where the integrated intensity varies depending on the specific round trip. Despite this variance, the amplitude remains in the same order of magnitude.

Unfortunately, in the synchronized case, the blue dots from the DNS do not fully align with the continuation (orange). This discrepancy is due to the finite time step used in the DNS. Reducing the integration step size decreases the variance in the integrated intensity values. Additionally, the loop is very narrow, and `DDE-Biftool` can employ a higher number of mesh points per period since it only uses one period. Such a small discretization step is not feasible in the DNS. However, the transition from the synchronized to unsynchronized case is proven with the fundamental change in the integrated intensity of the DNS.

A two-parameter continuation of the two fold bifurcation points in m and ω results in a diagram known as an Arnold tongue, depicted in Fig. 3.3. Inside the colored region, the two oscillators synchronize. The fold continuation, or Arnold tongue, for several other solutions of the KGTI in the same parameter regime is displayed in Fig. 3.16.

As described in textbooks on synchronization, for small values of m, the borders of the Arnold tongue are linear. However, with stronger coupling, other system-specific effects come into play [PRK01].

The highly asymmetric shape of the tongue for $m > 0.24$ indicates that at high modulation strengths, the pulses of the KGTI can more easily be accelerated to synchronize with the phase modulation. Conversely, the frequency range where the pulses need

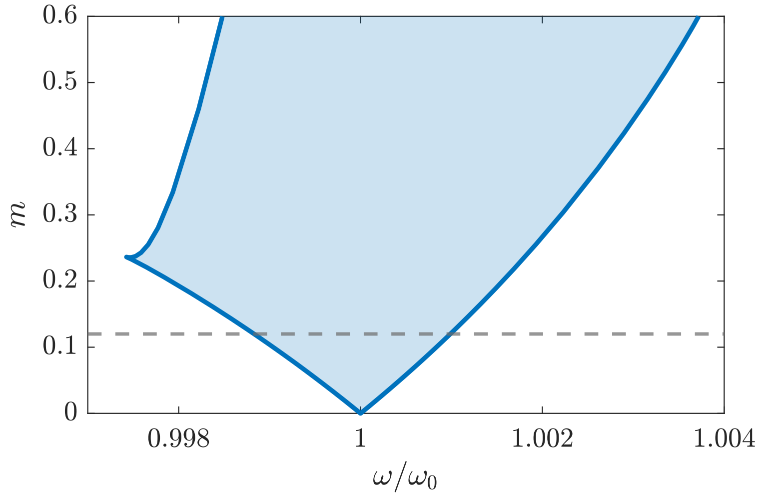

Figure 3.3: Arnold tongue for the synchronization of the periodic orbit of a TLS with the periodic phase modulation of frequency ω and amplitude m. The dashed line corresponds to the case displayed in Fig. 3.2. The other parameters are as in Fig. 3.1.

to be decelerated for synchronization is significantly smaller. These effects are highly nonlinear and are further explored in Chapters 3.2.1 and 3.4.2.

3.1.2 Higher-Order Synchronization

So far, we have assumed that the periodic forcing has a frequency ω close to that of the TLS without phase modulation ω_0, resulting in synchronization where these frequencies become equal. Now, consider a periodic modulation of the feedback phase with e.g. double the frequency (or half the frequency). When the frequency of the phase modulation is doubled, every other oscillation of the phase modulation is empty and the synchronization ratio becomes 1 : 2, as shown in Fig. 3.4 (iii).

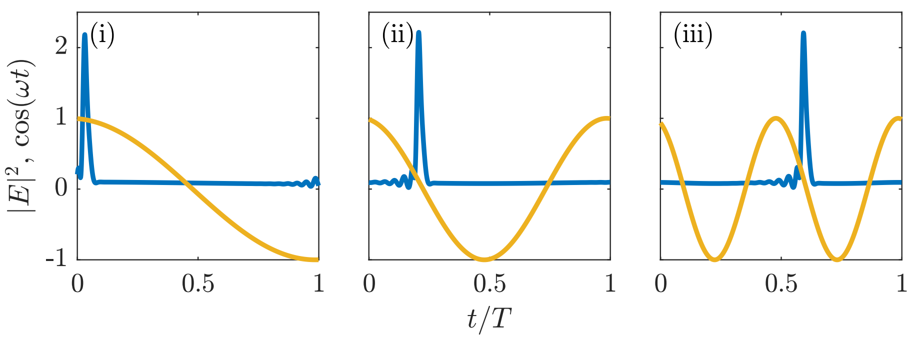

Figure 3.4: Time traces of higher-order synchronization with frequency (i) $\omega = \omega_0/2$, (ii) $\omega = \omega_0$ and (iii) $\omega = 2\omega_0$. Here, $\omega_0 = 0.0619$ and all other parameters are as in Fig. 3.1.

Fig. 3.4 displays one period $T_0 = 2\pi/\omega_0$ of the time trace for 2 : 1, 1 : 1, and 1 : 2 synchronization ratios. The chosen period T_0 corresponds to that of the TLS without modulation, approximately $T \approx 101.6$, in all three cases. For the phase modulation we choose multiples of the the natural frequency ω_0. Therefore, in parameter space we are

located at the center of the corresponding Arnold tongue. In Fig. 3.4 (i), two pulses appear within one period of the phase modulation, while in Fig. 3.4 (iii), every second oscillation is "skipped". Additionally, Fig. 3.4 (ii) depicts the original case with one pulse per period of the phase modulation.
Typically the higher-order tongues are very narrow so that it is difficult to find them but, in theory, synchronization is possible with widely different frequencies [PRK01]. However, for this thesis we will concentrate on the 1 : 1 tongues.

3.1.3 Saddle-Node Infinite Period Bifurcation

At a general level, we now understand the dynamics both inside and outside of a synchronization tongue. However, the question remains: what occurs when crossing from the unsynchronized to the synchronized state by continuously changing ω?

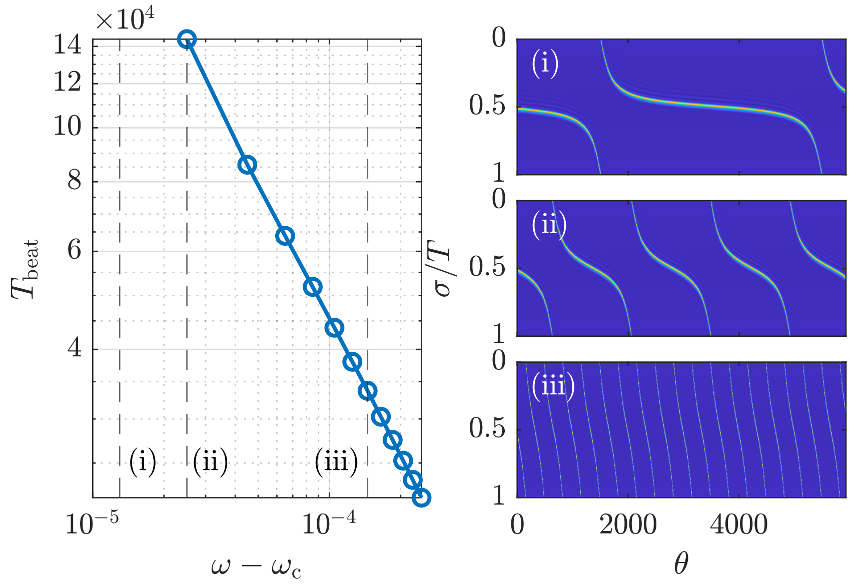

Figure 3.5: Scaling behavior of the period T at the border of an Arnold tongue in a double logarithmic diagram. The critical frequency is $\omega_c = 0.061965$. (i) - (iii) show DNS in two-time representations at the indicated positions which correspond to the frequencies $\omega = \{0.061969, 0.61975, 0.621\}$, respectively. All other parameters are as in Fig. 3.1.

We adjust ω along the dashed horizontal line in Fig. 3.3 and make DNS and concentrate the fold on the loop's right side. Far from the synchronization region, the period of the beat remains small, but as we approach the border, this period begins to diverge, as illustrated in Fig. 3.5 (i)-(iii). This diverging period hints at the occurrence of a global bifurcation. Additionally, the color maps in the two-time diagrams remain consistent, indicating that while the periodicity changes, the amplitude remains within the same order of magnitude. This fact is also clearly visible in the integrated intensity shown in Fig. 3.2 (ii). To establish a scaling law for the period, we plot $T_{\text{beat}} = 2\pi/\Omega_{\text{beat}}$ as a function of $(\omega - \omega_c)$ in a double-logarithmic diagram. In this case the critical frequency is $\omega_c = 0.061965$.
The double logarithmic plot in Fig. 3.5 shows a straight line, suggesting an exponential scaling of the period as $T_{\text{beat}} \propto (\omega - \omega_c)^{-1/2}$. This scaling behavior is characteristic of

a **S**addle-**N**ode **I**nfinite **Per**iod (SNIPER) bifurcation [Str15].
More figuratively speaking, as ω decreases, the limit cycle corresponding to periodic motion through the σ-dimension forms a bottleneck at approximately $\sigma = 0.5/T$. The exact position of the bottleneck depends on the side of the Arnold tongue where the synchronization border is crossed. On the other side of the Arnold tongue the bottle neck would form at approximately $\sigma = 0$. For more details on this topic see Section 3.4.3.
At the bottleneck, the pulse is slowed down by the phase modulation. This can be seen clearly in Fig. 3.5 (i), where the pulse remains at $\sigma \approx 0.5/T$ over many round trips. At the critical modulation frequency ω_c, the pulse is not only decelerated at the bottleneck, now the pulse is entrained to the phase modulation and synchronization of the TLS in the KGTI occurs. At this critical point, a new stable attractor emerges, corresponding to a stable periodic orbit. In the case of the system given in Chapter 2.3.4 the SNIPER bifurcation involves one limit cycle and fixed points. In the transition between unsynchronized and synchronized, the situation is much more complicated as there are only limit cycles and no fixed points involved.

3.1.4 Excitable Orbits

When the parameters (ω, m) are chosen near the edge of an Arnold tongue, the pulses are positioned close to the extrema of the phase modulation (for more background on this point see Chapter 3.4.3) and the entire dynamics is close to the transition between a stable periodic orbit to a quasi periodic motion. The quasi-periodic motion includes a comparatively large excursion through the space-like dimension. In this scenario, random noise can be used to excite the pulse, causing it to propagate through the period.
A dynamical system is deemed excitable if a sufficiently strong perturbation from the resting state triggers a large-amplitude excursion in phase space, mostly independent of the specifics of the perturbation, before returning to the resting state. Excitability is a concept observed in various real-world systems, such as the action potential of neurons. There are four generic types of excitability, defined by the nearby codimension-1 bifurcations that lead to a limit cycle [Izh06].
One of these bifurcations leading to a periodic orbit is the SNIPER bifurcation, a bifurcation we can find at the edges of the synchronization regions in the KGTI with phase modulation. When ω and m are chosen such that the system is within an Arnold tongue but near its edge, adding noise can perturb the system enough to trigger an excitable orbit. This perturbation causes the pulse to undertake a large-scale excursion through the space-like time dimension, after which it returns to its resting position. Subsequent excursions occur when random perturbations are sufficient to push the pulse out of the stable part of the period.
In Fig. 3.6, a two-time diagram illustrates such an excitable orbit in the phase modulated KGTI. The resting position of the pulse in the space-like dimension is near the minimum of the phase modulation, as seen in Fig. 3.20. When the pulse reaches the other side of the minimum due to noise, it becomes unstable and travels through the period until it once again stabilizes near the phase modulation minimum. The excursions are timed randomly due to the noise, ruling out the periodic excursions seen in

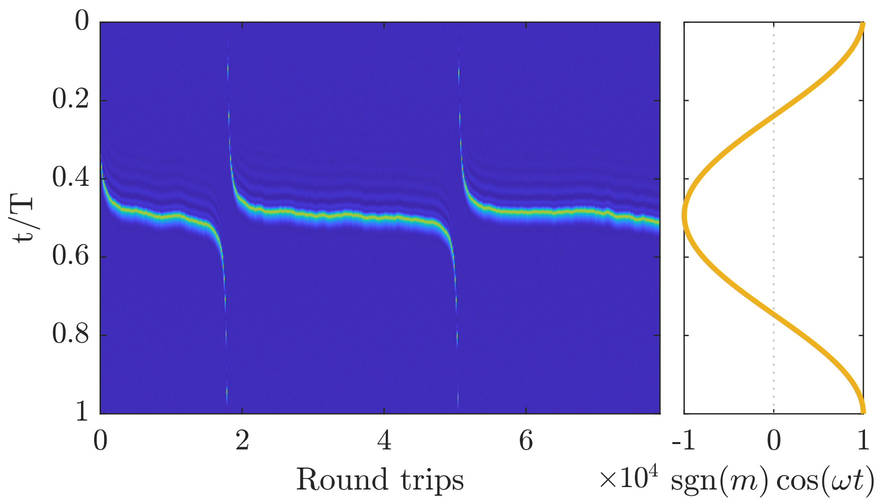

Figure 3.6: An excitable orbit in the KGTI shown in a two-time representation (left) relative to the phase modulation (right). The parameters are $\delta = 1.5$, $h = 2$, $\eta = 0.75$, $\varphi_0 = 0$, $m = 0.08$, $\omega = 0.06194672$, $Y_0 = 0.55$, $\tau = 100$ and the noise amplitude is $7.5 \cdot 10^{-3}$.

the unsynchronized case.

3.2 Weakly Dissipative Limit

After a general analysis in the framework of synchronization, we will start with a detailed study of the TLS and modes appearing as solutions in the KGTI with phase modulation. We will begin our analysis from a weakly dissipative limit. In this limit the KGTI was shown to be equivalent to the well-studied LLE. This regime is marked by small cavity losses and weak injection, i.e., $\eta \approx 1$ and $\tilde{\varphi}$ has to be in the same order of magnitude as η differs from one [SGJ22], for more details see Chapter 2.5.3.
Additionally, beyond the constraints of the LLE regime, we have selected $\delta = 1/\sqrt{3}$, which results in $\beta_3 = 0$ and thus eliminates third-order dispersion. This choice simplifies the dynamics of the microcavity. We refer to this specific value of δ as δ_{magic}. Additionally, this choice enables us to compare our results with previous works from another group which studied the LLE with a parabolic potential [Sun+20; Sun+22; SWP23].
A monomode CW injection invariably maintains a uniform CW background. In the KGTI, as defined in Eqs. (2.25a) and (2.25b), the CW solutions can form a bistability characterized by an S-shaped curve between high and low intensity CW solutions. In the original setting, without phase modulation, and with parameters $\delta = 1/\sqrt{3}$, $h = 2$, $\eta = 0.99$, $\varphi_0 = 0.3235\pi$, and $\tau = 300$, the resulting continuation in Y_0 is illustrated in the backdrop of Fig. 3.7 in light gray.
Operating the KGTI in the normal dispersion regime devoid of third-order dispersion ($\delta = 1/\sqrt{3}$), we find no stable bright TLS [Par17] only the dark counterparts. After rescaling to remove the drift term, only even derivatives remain in the differential equation, resulting in (almost) symmetric pulses. Only higher-order terms and mixed derivatives of third order, such as fifth-order residuals truncated during the multiscale

analysis, may introduce slight asymmetries. In Fig. 3.7, the solution branch of the dark TLS is depicted in dark gray, illustrating the typical collapsed snaking in the upper half, while the lower half seamlessly transitions back to the low-intensity CW state given the absence of bright TLS solutions.

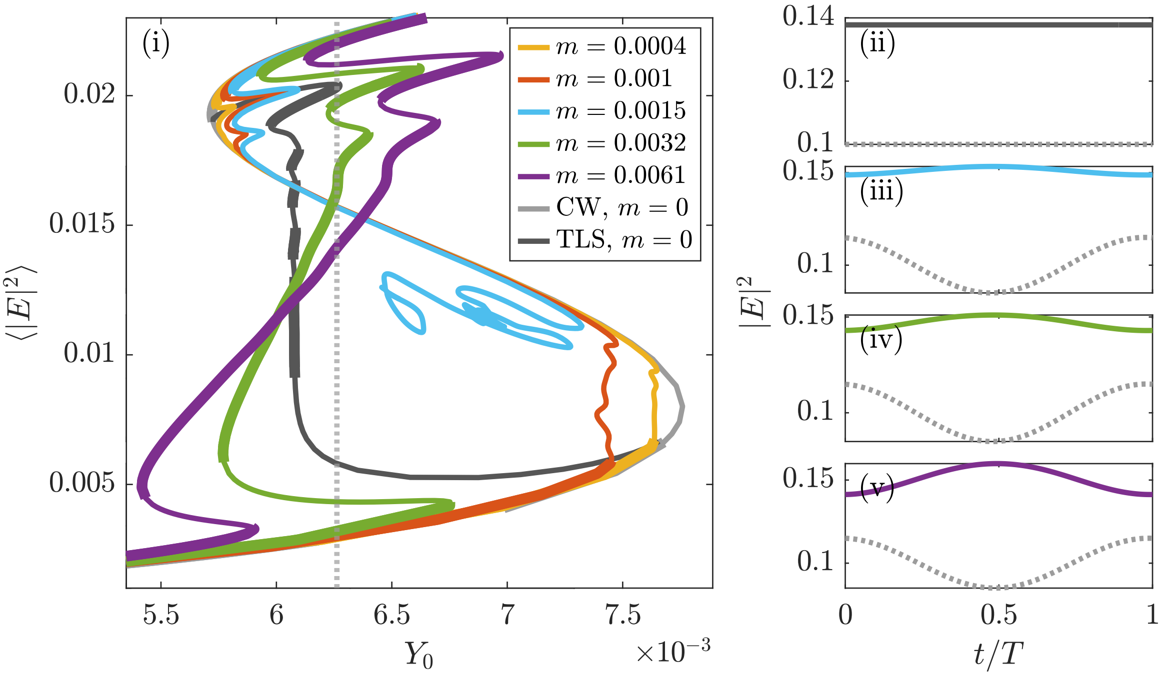

Figure 3.7: (i) Bifurcation diagram in Y_0 showing the original CW and TLS branches for $m = 0$ and deformed equivalences of CW branch for finite modulation strengths m. The parameters are $\delta = 1/\sqrt{3}$, $h = 2$, $\eta = 0.99$, $\varphi_0 = 0.3235\pi$, $\omega = 0.0208 \approx 2\pi/T$, and $\tau = 300$. Panels (ii) - (v) show the modulated high-intensity CW solutions the corresponding position in (i) at the dashed line close to the upper stable part of the CW solution. The dashes line indicates the phase modulation profile.

3.2.1 Influence of Phase Modulation on the Weakly Dissipative Limit

We now activate the phase modulation and examine its impact on the TLS solutions. For the modulation frequency we chose the frequency of the periodic orbit corresponding to the first dark TLS which is $\omega = 0.0208 = 2\pi/T$ and the modulation strength m is gradually increased. First, we focus on the CW branch and in a second step we will discuss the TLS branch.

3.2.1.1 Continuous Wave Solutions

For the CW branch, we observe a progressive deformation originating at the fold points, illustrated in Fig. 3.7 (i). Near the upper fold point, the deformation initially resembles a collapsed snaking pattern, though it remains completely unstable for small values $m = \{0.0004, 0.001, 0.0015\}$. As m increases, segments of the branch stabilize and take on a slanted form reminiscent of the original TLS branch at $m = 0$.

Conversely, the deformation at the lower fold point appears significantly more irregular, lacking discernible structure for small m. At $m = 0.0015$, this branch connects to some unstable and irregular structures, since this part is unstable we will not investigate it further. Only at higher values of m, the deformed CW branch regains stability and reconnect with its lower counterpart.
Examining the profiles of the CW solutions, for $m = 0$, as anticipated, we observe a horizontal line, as shown in Fig. 3.7 (ii). With increasing modulation strength, this line bends, resembling a cosine-like profile, as depicted in Fig. 3.7 (iii) and (iv). Finally, at higher modulation strengths, illustrated in Fig. 3.7 (v), the CW solution undergoes significant deformation due to phase modulation, resulting in a Gaussian-like pulse, this last comparison is even more clearer in Fig. 3.11 (i).

3.2.1.2 Temporal Localized States

In contrast, the TLS branch, shown in Fig. 3.7 (i) (dark gray), exhibits a markedly different behavior. Upon introducing periodic forcing, the TLS branch (dark gray) breaks down, leaving behind an isolated loop of infinitesimal size for every point of the original TLS branch. This loops are called isolas and are bordered by two fold bifurcations. However, when m increases the isolas start to grow in width and reconnect with each other. This process of growing and reconnecting is illustrated in Fig. 3.7 (i) - (v). The markers indicate the points from the original TLS branch that we will follow for increasing values of m.
In Fig. 3.8 (ii), for the finite value of $m = 0.0004$, multiple of the infinitesimal isolas have already connected. At this value there are four isolas observable marked at the two corresponding fold bifurcations with crosses, squares and triangles, respectively. One loop is marked with a diamond and on the other side a star. This loop is the result of two already reconnected loops.
Transitioning to panel (iii), at $m = 0.001$ the isolas marked with squares and triangles have connected to form an extended isola. The isola marked with a diamond and a star has been left out to increase clarity. Further increasing m to 0.0015 the isolated loop is almost touching the deformed CW branch (see panel (v), triangle marker), this indicates the modulation amplitude m where the isolated loops reconnect to the CW branch. Increasing m beyond 0.0015, the isolas are reconnected with the deformed CW branch, described in the previous chapter, marking the point at which the snaking structure of the modulated CW branch regains the typical alternating stable/unstable structure, compare with the green and purple branches Fig. 3.7 (i). Fig. 3.8 (ii) - (v) illustrate these changes in the isolated loops and the (modulated) CW branch resulting from the phase modulation. The connection between the markers in each panels is even more explored in the following paragraph.
The three-dimensional plots in Fig. 3.9 depict the branches from Fig. 3.8 stacked behind each other, adding a third dimension to represent the amplitude of the phase modulation m. Two-parameter continuation in Y_0 and m of the fold bifurcations bordering the isolated loops reveal how the marked points (black markers in Fig. 3.8) are connected and change for increasing m. Demonstrating the expanding and reconnecting behavior of the isolas and deformed CW branches. For instance, the isolas marked with triangles and squares originate from only one point on the TLS branch

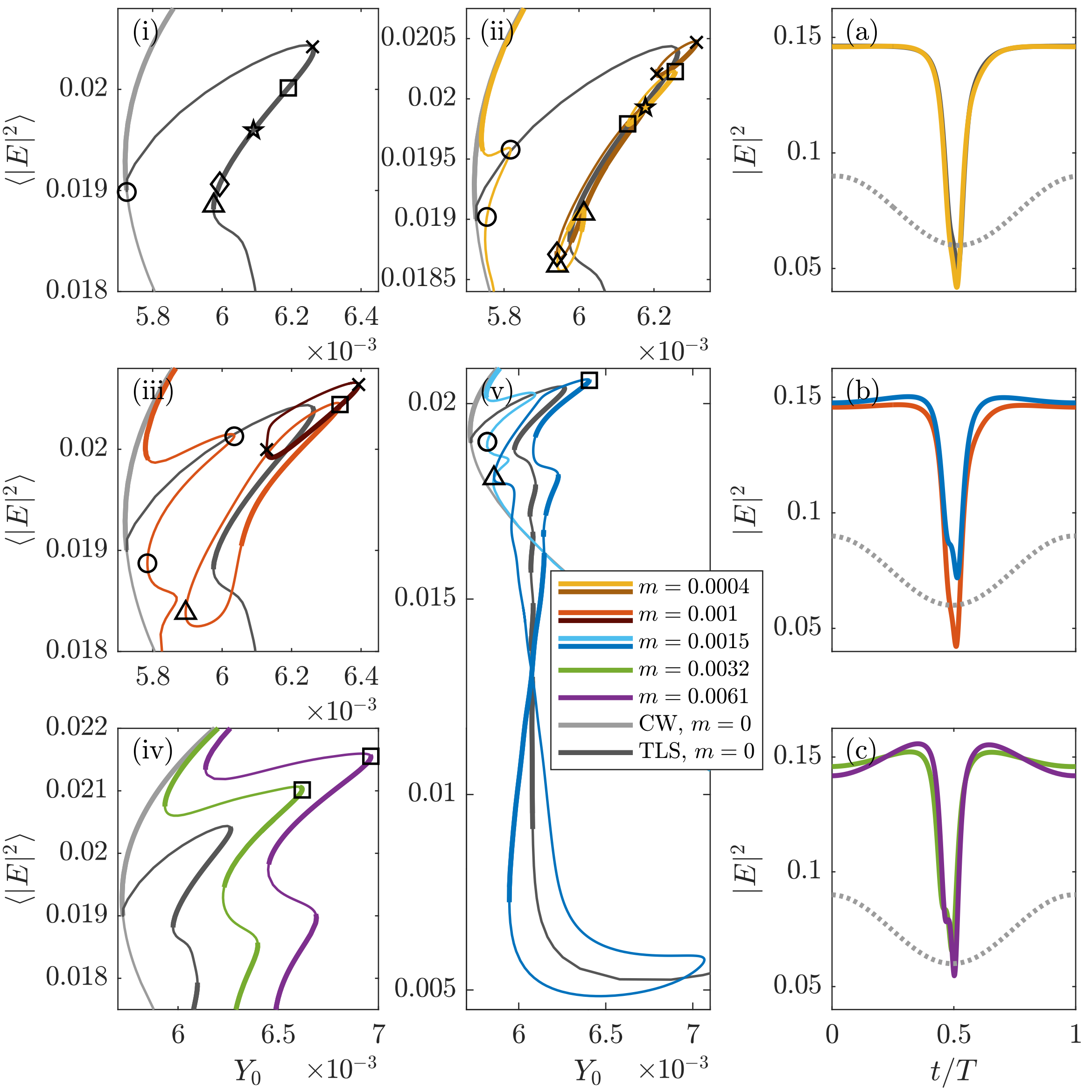

Figure 3.8: Bifurcation diagrams of the first dark TLS in Y_0 for $m = \{0, 4\times10^{-4}, 10^{-3}, 1.5\times 10^{-3}, 3.2\times10^{-3}, 6.1\times10^{-3}\}$. The case for $m = 0$ (light and dark gray), from panel (i), is always displayed in the background. The points marked in panel (i), at $m = 0$, are tracked through panels (ii) - (v) for increasing m. The markers can be connected via two-parameter continuations of fold bifurcation points in m and Y_0, see Fig. 3.9. The parameters are the same as in Fig. 3.7. (a) - (b) show the corresponding profiles of stable TLS at corresponding m-value. The dashed line indicates the phase modulation profile.

with $m = 0$. As m increases these isolas grow in width and connect at the fold points facing each other. The corresponding fold bifurcation point continuations form a W-shape in the (Y_0, m)-plane (solid black line in Fig. 3.9), where the reconnecting occurs as m increases beyond the middle arc of the W. After this point, the isolas have merged to one big loop.
This pattern can be found at various stages of the reconnection process, at a small scale e.g. the diamond and pentagram markers connected with the thin dotted line, or

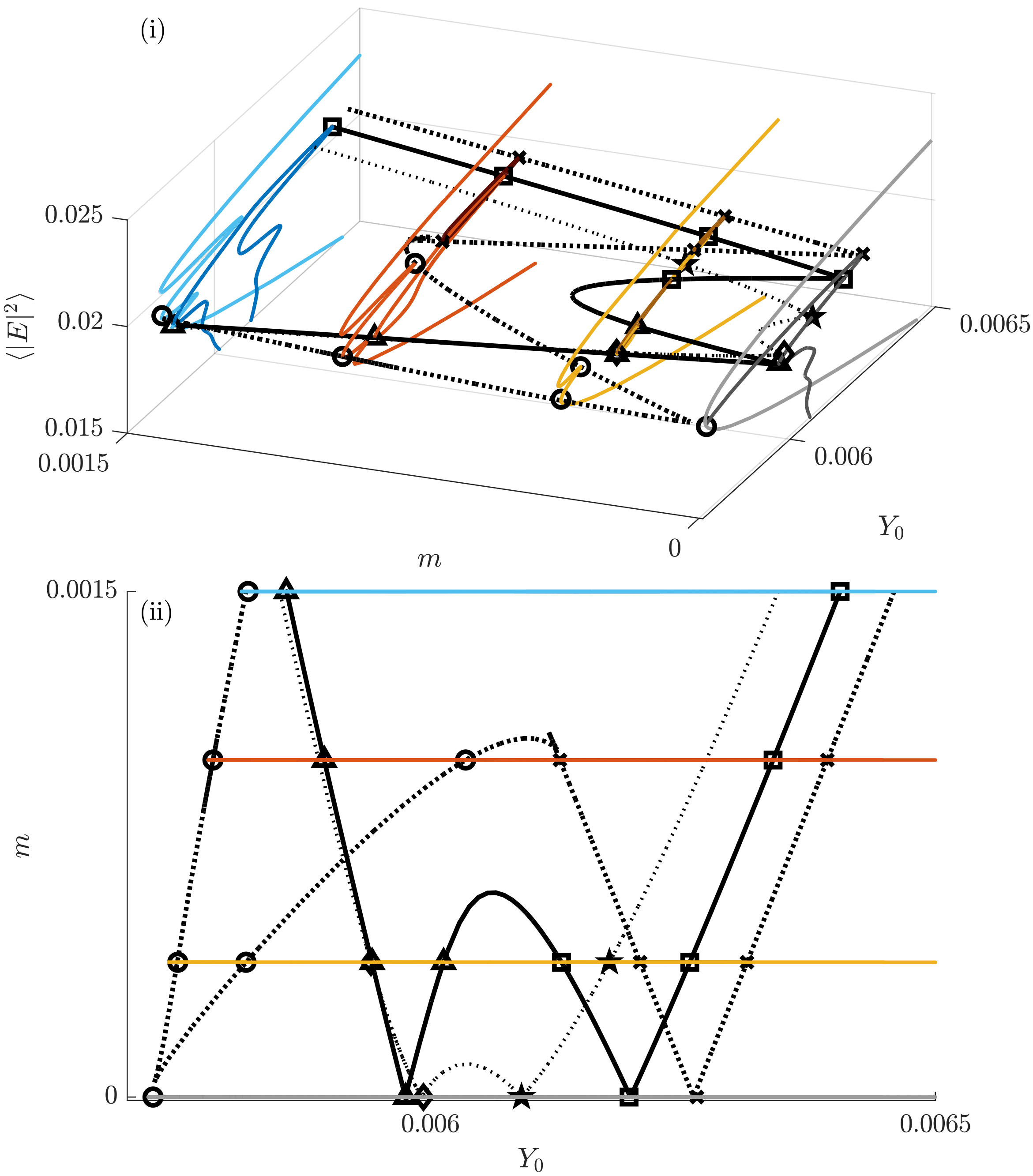

Figure 3.9: Bifurcation diagrams showing the reconnecting of isolas when increasing the modulation strength m. The colored branches are the same as in Fig. 3.8, additionally, we show continuations of fold bifurcation points which connect the colored branches at the various m-values. Panel (i) shows a three-dimensional version, additionally including an axis for the modulation strength m and panel (ii) shows the projection of the top panel into the (Y_0, m)-plane.

large scale, marked with crosses and circles (thick dotted line). In this manner, each point on the TLS for $m = 0$ becomes a tiny isola for a finite m and immediately starts to reconnect with other isolas forming larger isolas, as m in creases, as depicted in Fig.

3.8. Until, for large m we only have one unified branch left which is a slanted version of the original TLS branch.
The profiles of TLS solutions corresponding to these isolated islands are displayed in Fig. 3.8 (a) - (c). For small m (i.e. the yellow profile in panel (a)) they closely resemble those of the original case with $m = 0$ (dark gray), with the main distinction being a slight modulation in background intensity due to the periodic phase modulation, akin to the modulated CW solutions, compare Fig. 3.7 (ii) - (v). As m increases further, the curvature of high-intensity CW background on which the TLS live becomes more pronounced, compare Fig. 3.8 (b) and (c), as expected from the analysis of the CW branch.
At $m = 0$, the TLS form due to locking of domain walls. With phase modulation, understanding the changes in TLS profiles requires considering the Hermite-Gauss modes that we discuss in the next section.

3.2.2 Hermite-Gauss Modes

In the good cavity limit, where $\eta \approx 1$ and $\tilde{\varphi}$ is small, the KGTI can be described by the LLE, as shown in Eq. (2.31). Mathematically, the LLE corresponds to a driven and damped nonlinear Schrödinger equation [SGJ22]. Adding the periodic phase modulation, in the approximated form of a parabolic potential and neglecting gains and losses, we get to the Gross-Pitaevskii equation. For the "cold cavity", i.e. without the Kerr nonlinearity, the approximations lead to the one-dimensional Schrödinger equation of a harmonic oscillator and the corresponding solutions are the so-called Hermite-Gauss (HG) modes [Sun+20] and can be calculated analytically. Therefore, when the influence of the nonlinearity is small, a solution of the full system can be decomposed in the orthonormal basis of the HG modes [Sun+22].
The HG modes, are given by

$$\psi_n\left(\frac{x}{d}\right) = \frac{\pi^{-1/4}}{\sqrt{2^n n!}} H_n\left(\frac{x}{d}\right) e^{-\frac{x^2}{2d^2}}, \tag{3.1}$$

with $n \in \mathbb{N}$, where $H_n(y)$ are the Hermite polynomials and we define $y = d\frac{x}{d}$ with the scaling ratio d corresponding to the width of the HG modes [Sun+23]. The modes fulfill the following differential equation

$$\frac{\partial^2 \psi_n}{\partial y^2} + (2n + 1 - y^2)\psi_n = 0. \tag{3.2}$$

First, we neglect the term $F(A)$ on the right-had side of the LLE, defined in Eq. (2.31). Consequently, the linear part of the LLE can be reduced to the Gross-Pitaevskii equation

$$\partial_\theta A = i\tilde{\varphi}(\sigma)A - i\frac{\beta_2}{2}\frac{\partial^2 A}{\partial \sigma^2}. \tag{3.3}$$

In this case, the function $\tilde{\varphi}(\sigma)$ introduces the periodic phase modulation. For simplicity, we focus on one pulse and one period of phase modulation. By using a Taylor expansion of the cosine function defining the phase modulation, we can approximate the periodic potential as a parabolic potential. It is crucial to choose the correct expansion point. Numerical time integration shows that TLS are always positioned at the minimum of

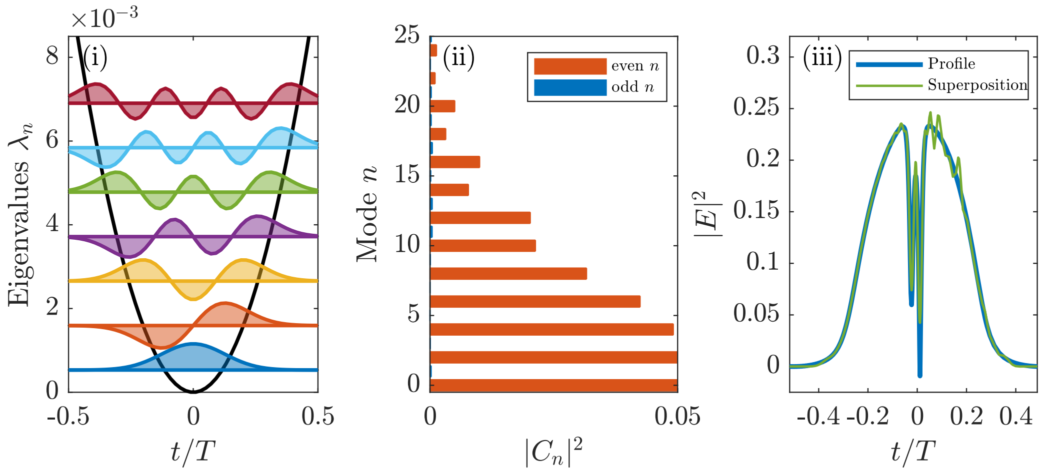

Figure 3.10: (i) HG modes, Eq. (3.1), in a parabolic potential at their corresponding eigenvalues, shifted by $\Delta\varphi$ for clarity. (ii) mode energies $|C_n|^2$ for the pulse shown in (iii). (iii) exemplary pulse from the LLE regime (blue) and superposition of HG modes (green).

the phase modulation for the synchronized case in the LLE limit. Therefore, we shall differentiate between two cases depending on the sign of m.

1. **Case $m > 0$:**

In this case, the minima of the phase modulation coincide with those of the cosine function, thus the expansion point is placed at π/ω. This results in:

$$m\cos(\omega\sigma) = |m|\left(-1 + \frac{(\omega\sigma)^2}{2}\right) + \mathcal{O}\big(\sigma^4\big).$$

2. **Case $m < 0$:**

In this case, the minima of the phase modulation coincide with the maxima of the cosine. Consequently, the cosine is expanded at zero:

$$m\cos(\omega\sigma) = -|m|\left(1 - \frac{(\omega\sigma)^2}{2}\right) + \mathcal{O}\big(\sigma^4\big) = |m|\left(-1 + \frac{(\omega\sigma)^2}{2}\right) + \mathcal{O}\big(\sigma^4\big).$$

Both cases can be unified into a single formulation that is independent of the sign of m. This allows us to rewrite the term $\tilde{\varphi}(\sigma)$ as follows:

$$\begin{aligned}\tilde{\varphi}(\sigma) &= \varphi(\sigma) - 2\arctan(\delta)\\ &\approx \varphi_0 + |m|\left(-1 + \frac{(\omega\sigma)^2}{2}\right) - 2\arctan(\delta)\\ &= \frac{|m|\omega^2}{2}\sigma^2 + \Delta\varphi.\end{aligned}$$

Using $\Delta\varphi = |m| + \varphi_0 - 2\arctan(\delta)$, we introduce a constant term $\Delta\varphi$ in Eq. (3.3), resulting in a constant shift in the corresponding eigenvalues. By inserting the rewritten terms into Eq. (3.3) and using the abbreviations $C = \dfrac{|m|\omega^2}{2}$ and $B = -\dfrac{\beta_2}{2}$, we obtain:

$$\partial_\theta A = \left(i\frac{|m|\omega^2}{2}\sigma^2 + i\Delta\varphi\right)A - i\frac{\beta_2}{2}\frac{\partial^2 A}{\partial\sigma^2} \tag{3.4}$$

$$= \left(iC\sigma^2 + i\Delta\varphi\right)A + iB\frac{\partial^2 A}{\partial\sigma^2}. \tag{3.5}$$

To solve this equation, we use the ansatz $A(\sigma,\theta) = e^{-i\lambda_n\theta}\psi_n\left(\frac{\sigma}{d}\right)$. Substituting this ansatz into Eq. (3.5) leads to the following linear eigenvalue problem:

$$-i\lambda_n\psi_n(\sigma) = \hat{H}\psi_n\left(\frac{\sigma}{d}\right), \tag{3.6}$$

where $\hat{H} = iC\sigma^2 + i\Delta\varphi + i\frac{B}{d}\partial_\sigma$. Utilizing the HG modes and Eq. (3.2), we separately solve the homogeneous and inhomogeneous parts. For the homogeneous part, we find the scaling ratio of the HG modes:

$$d^2 = \sqrt{-\frac{B}{C}} = \sqrt{\frac{\beta_2}{|m|\omega^2}}.$$

Thus, we can conclude that as the absolute value of the phase modulation strength increases, the width of the HG modes decreases.
From the inhomogeneous part, we find the dressed eigenvalues:

$$\lambda_n = -\Delta\varphi + \frac{B}{d^2}(2n+1) = -\Delta\varphi - \sqrt{BC}(2n+1).$$

The dressing of the eigenvalues with the constant shift of $\Delta\varphi$ arises from two sources. The first contribution originates from the first term of the Taylor expansion: $|m|$ and the second from the effective round trip phase $\tilde{\varphi}_0 = \varphi_0 - 2\arctan(\delta)$.
In Fig. 3.10 (i) the HG modes, defined in Eq. 3.1, are shown inside a parabolic potential, located at the corresponding eigenvalues but shifted by $-\Delta\varphi$ for clarity. Here, the relationship of the HG modes, corresponding eigenvalues and parabolic potential is visible.
Since the HG modes, as definded in Eq. (3.1), form a complete orthogonal basis, any solution $A(\sigma,\theta)$ of Eq. (3.3) can be expanded in HG modes as

$$A(\sigma,\theta) = \sum_n C_n(\theta)e^{i\lambda_n\theta}\psi_n(\sigma), \tag{3.7}$$

where

$$C_n(\theta)e^{i\lambda_n(\theta)} = \int_{-\infty}^{\infty} A(\sigma,\theta)\psi_n(\sigma)\mathrm{d}\sigma \tag{3.8}$$

is the complex amplitude. Here, the mode energy corresponds to $|C_n(\theta)|^2$ [Sun+22].
In Fig. 3.10 (ii), the mode energy distribution corresponding to the TLS in Fig. 3.10 (iii) or Fig. 3.11 (ii) is plotted. As shown, only even modes contribute significantly to the pulse sjape. The mode energies of the odd modes are negligible and not visible in the bar diagram. This underlines the fact that the LLE, Eq. (2.31), at $\delta = \delta_{magic} = 1/\sqrt{3}$ contains only even terms, resulting in an (almost) symmetric temporal profile. Only

small higher-order odd terms, such as the fifth-order terms, contribute minimally. Fig. 3.10 (iii) compares the original TLS profile (blue) with the superposition of HG modes weighted by the calculated mode energies $|C_n|^2$ (green). The good agreement demonstrates that the cavity's dynamics can be described by HG modes.
The characteristics of the HG modes explain the behavior of the pulse shapes observed earlier in Fig. 3.11. Starting with a small phase modulation strength, the HG modes are broad, and the background on which the TLS live is only slightly bent. As the absolute value of $|m|$ increases, the scaling ratio d decreases, resulting in more localized HG modes with narrower widths. Simultaneously, the field amplitudes $|E|^2$ and $|Y|^2$ drop to nearly zero in the remainder of the period. While the background, on which the dark TLS live, undergoes significant deformation, the TLS themselves remain confined at the potential minimum and exhibit no significant dynamics. The strong deformation of the background causes the profiles to resemble bright TLS look-alikes. However, this is simply the HG modes dominating the dynamics and reshaping the high-intensity background due to the parabolic potential created by the periodic phase modulation.

3.2.3 Resonance Curves: $\tilde{\varphi}_0$-Continuations

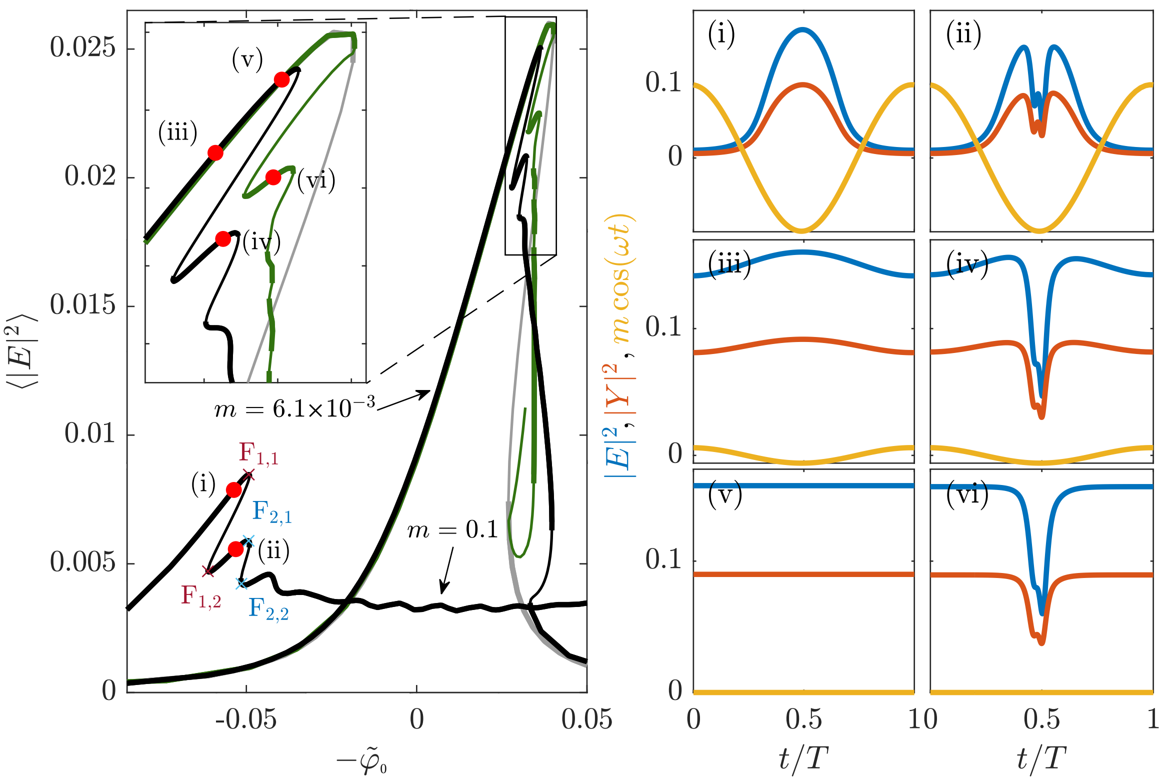

Figure 3.11: Bifurcation diagram showing the integrated pulse intensity versus $-\tilde{\varphi}$ for the CW (light gray) and TLS (green) with $m = 0$, and TLS for $m = \{6.1 \times 10^{-3}, 10^{-1}\}$ (black). (i) - (vi) present the corresponding profiles at the positions indicated with the red dots, we show $|E|^2$ in blue, $|Y|^2$ in orange and the phase modulation profile in yellow. The parameters are as in Fig. 3.7 and the injection in this diagram is $Y_0 = 0.0066$.

In the KGTI, as defined in Eqs. (2.25a) and (2.25b), the parameter $\tilde{\varphi}_0 = \varphi_0 -$

$2\arctan(\delta)$ corresponds to the cavity detuning in the LLE. A continuation of the CW solution in $\tilde{\varphi}_0$, for $m = 0$, reveals the cavity's resonance curve, shown in light gray in Fig. 3.11. The Kerr nonlinearity induces an intensity-dependent nonlinear phase shift [Sun+23], causing a tilt in the cavity's response curve. At high intensities, the phase shift becomes more pronounced, leading to a bistability of CW solutions. The TLS for $m = 0$, which form as domain walls between the high- and low-intensity CW solutions, lie on a snaking branch, displayed in green in Fig. 3.11.
When the potential strength is increased to $m = 0.031$, the detuning region widens slightly, but the overall shape of the TLS branch remains qualitatively the same. Further increasing m to 0.062 results in an extended resonance curve. The several resonance peaks can be traced back to the HG modes, the linear eigenmodes of this system, which fill the phase-modulated system and dominate the dynamics in this regime [SWP23; Sun+23].
The resulting bifurcation diagrams in $\tilde{\varphi}_0$ for varying m show how the system's resonances change from the unmodulated case, where TLS form via domain locking, to dynamics dominated by HG modes. A similar study, but fully restricted to the LLE, has been presented in [SWP23; Sun+23], and the resulting bifurcation diagrams exhibit qualitatively the same behavior. However, the equations are formulated slightly different, since in our case the LLE (see Eq. (2.31)) is derived from the KGTI. Comparing the two formulations, one can see that the variable $-\tilde{\varphi}_0$ corresponds to the cavity detuning used in [SWP23; Sun+23]. Therefore, to be able to directly compare the results, we show $-\tilde{\varphi}_0$ on the horizontal axis.
Increasing the injection Y_0 introduces more energy into the cavity, raising the intensities and causing the Kerr effect to further tilt the resonance peak. Additional fold bifurcations can occur and the bistability ranges widens [SWP23]. Two-parameter continuation in Y_0 and $\tilde{\varphi}_0$ of the fold bifurcations marked in Fig. 3.11 shows that increasing Y_0 leads to potentially richer dynamics. Depending on the value of Y_0 (while keeping $\tilde{\varphi}_0$ fixed), the number of fold bifurcations can be controlled. The corresponding diagram is shown in Fig. 3.12.

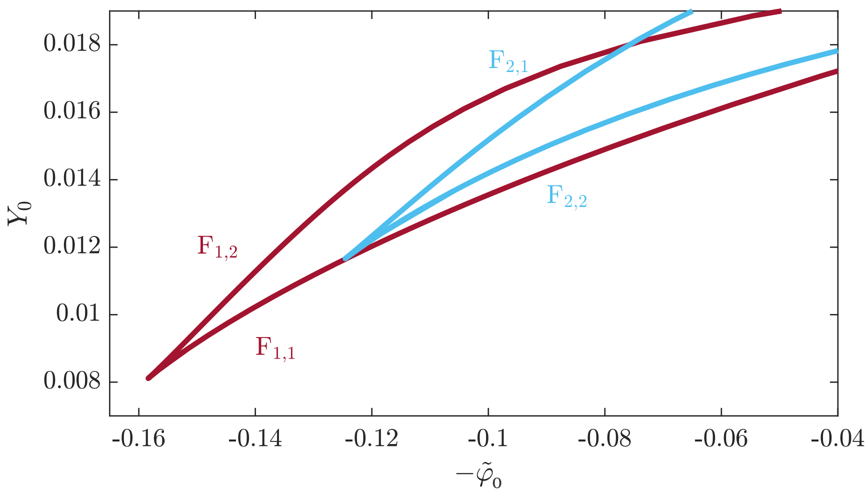

Figure 3.12: Phase diagram in $-\tilde{\varphi}$ and Y_0 showing continuations of fold bifurcation points. The continued bifurcation points are marked in Fig. 3.11.

3.3 Leaving the Weakly Dissipative Limit

In the next step, we adjust δ, the detuning, to allow for third-order dispersion in our setup. Specifically, we modify δ to deviate from $\delta_{\mathrm{magic}} = 1/\sqrt{3}$. This adjustment would result in oscillatory tails both at the low and, additionally, at the high intensity levels, which stabilizes bright TLS. The oscillatory behavior of the fronts can be linked to their spatial eigenvalues. In the absence of third-order dispersion, the spatial eigenvalue corresponding to a front connecting the lower to the upper CW solution has a real value. When changing δ, this eigenvalue leaves the real axis and become complex. Now, both spatial eigenvalues are complex. The imaginary components cause an oscillatory approach to the upper CW state [PGG17]. Moreover, the new detuning value breaks the reflection symmetry at a low order, namely the third order, which cannot be neglected (unlike the fifth order), thus leading to highly asymmetric pulses.
Regrettably, we also need to reduce the value of η. The strong reflectivity of the external mirror results in pronounced oscillatory tails, making a numerical study challenging as a very fine mesh would be required to resolve these fine structures. To maintain feasible computation times, we must allow for more dissipation, decreasing to $\eta = 0.95$.
However, numerical path continuations remain computationally intensive. Therefore, we will focus on studying the main concept: the formation of isolas and the reconnection of isolas into a unified branch.
The choice of $\delta = 0.75$ and $\varphi_0 = 0.323435\pi$, as used in Fig. 3.13, leads to $\tilde{\varphi}_0 = -0.27716$ which is outside the limit of the LLE, as defined in Eq. (2.31), placing this study in the nonlinear regime. Therefore nonlinear effects influence the cavity's dynamics and, furthermore, in the DAE it is not possible to distinguish the terms responsible for TOD as clearly as in the the PDE.
As illustrated in Fig. 3.13 (i), increasing δ to 0.75 causes the TLS branch for $m = 0$ (dark gray) to display additional snaking in its lower section. This snaking, even at its widest point, exhibits a tiny pinning region winding with a high frequency. The snaking is possible due to oscillatory tails at the high intensity level of the domain walls (see Fig. 3.13 (iii)), which allow the fronts to lock and form bright TLS [PGG17].
When increasing δ, the corresponding spatial eigenvalues for the fronts connecting the low-intensity domain to the high-intensity domain leave the real axis and become imaginary [Par17]. For δ values close to δ_{magic}, the imaginary part of the eigenvalues remains small, thus the oscillations have a high frequency and the domain walls can lock at various short distances due to the frequency of the oscillatory tails. Consequently, the snaking structure is confined to a narrow Y_0-range and features a high winding frequency. Further increasing δ results in oscillatory tails with a lower frequency and, therefore, a broader snaking pattern.
Comparatively, the snaking structure at the top corresponding to dark TLS is broader and has a lower winding frequency and covers a wider Y_0-range, owing to the lower frequency oscillatory tails at the low intensity CW domain (see Fig. 3.13 (iii)).
The implementation of phase modulation alters the original snaking branch, fragmenting it into a series of small isolated loops, similar to the LLE case before in Chapter 3.2.1. This fragmentation is shown in Fig. 3.13 (i), the dark gray branch breaks down into isolas for a finite m, two examples are shown in blue. When m increases, these isolas start to reconnect. Simultaneously, for a finite modulation strength m the CW

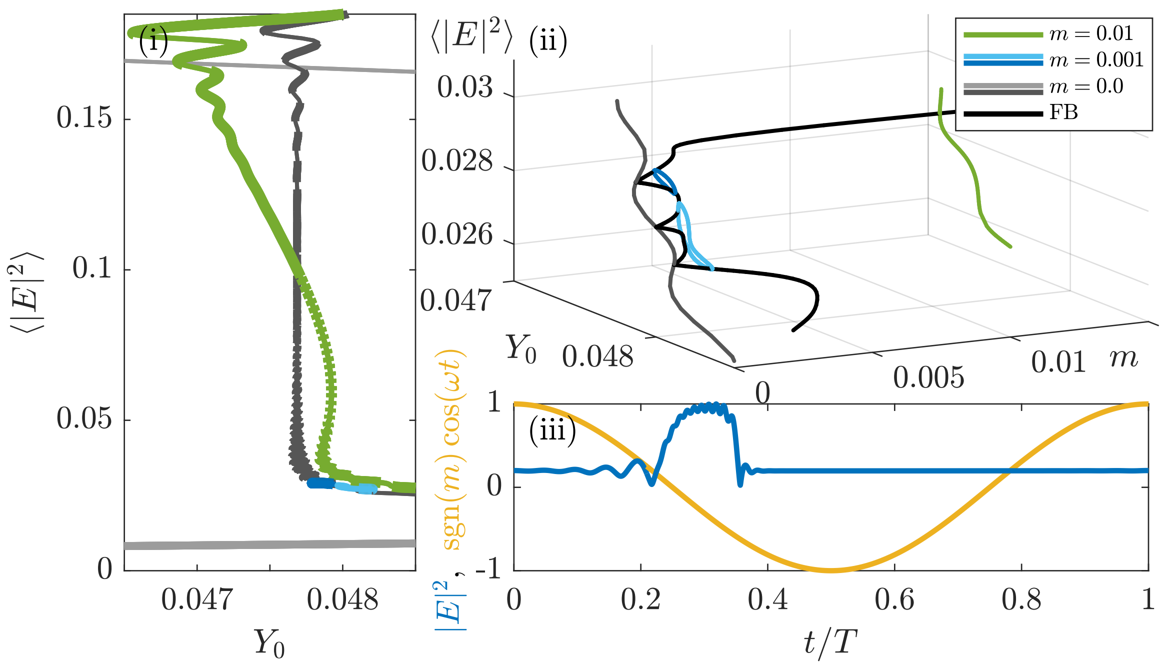

Figure 3.13: Bifurcation diagram close to the LLE regime, (i) shows continuations in Y_0 at $m = 0$ and at the finite value 0.001 (0.01) shown in blue (green). Panel (ii) presents the reconnecting of the isolas (blues) to a unified snaking branch (green) in a three-dimensional diagram. In black we show the connecting continuations of fold bifurcation points. (iii) shows an examplary pulse profile. The parameters are $\delta = 0.75$, $h = 2$, $\eta = 0.95$, $\varphi_0 = 0.323435\pi$, $\omega = 2\pi/301.6451$ and $\tau = 300$.

branch starts to deform at its fold bifurcation points, as before in the LLE regime in Chapter 3.2.1.1. This process is displayed in Fig. 3.13 (ii), where continuations of fold bifurcation points are shown (black) within a three-dimensional diagram. The fold continuation connects two isolas (blue) into a unified snaking branch (green) at $m = 0.01$. Note that the light blue isola, at a smaller modulation strength, would separate into two distinct loops for a smaller modulation strength.
However, the deformation to the CW branch are wildly unregular and show no structure. Furthermore, due to intricate field profiles it is numerically highly expensive to perform a continuation, therefore we are able to show the corresponding bifurcation diagram of the CW branch. Nevertheless, Fig. 3.13 (ii) displays the main concept: the growing and reconnection process of the isolas which occur as a consequence of including the phase modulation.
The profiles of the branches presented in Fig. 3.13 (ii) are all qualitatively very similar, hence only one profile is depicted in Fig. 3.13 (iii) to increase clarity. The similarity of the profiles can be traced back to the small intensity range covered by the blue isolas. For both, the reconnected snaking branch (green) and the original TLS branch (dark gray), a variety of locking distances are observable, spanning from dark to bright TLS. Furthermore, observing the TLS profile (Fig. 3.13 (iii)) the effect of phase modulation on the low-intensity CW background is only minimal and unnoticeable, even at the high modulation strength of the reconnected snaking branch in green. It is evident that the HG modes cannot influence the dynamics in this regime, since the HG modes would

introduce a strong modulation of the background intensity of the profiles. Additionally, the pulse shape is notably asymmetric, an effect explained by leaving the LLE regime and altering δ thus allowing for TOD, an asymmetric effect that corresponds to an uneven term in the LLE at a low order.

Another significant difference is the positioning of the stable pulses, which are not always situated at the lowest point in the valley of the phase modulation, as before without TOD in the LLE regime, but rather show a preference for certain positions within the period. Additionally, the pulses can move in the potential due to their asymmetric shape to arrive at this optimal position. In the LLE limit without TOD, the dynamics are primarily influenced by the HG modes, with the pulses always located at the minimum of the phase modulation. Consequently, the HG modes do not constitute an adequate explanation for the observed pulse shapes and positioning. The reason for this subtle pulse positioning within the potential will be further studied in the following chapters, within a parameter range that is computationally more feasible.

3.3.1 Stabilizing TLSs Outside of the Bistability Region

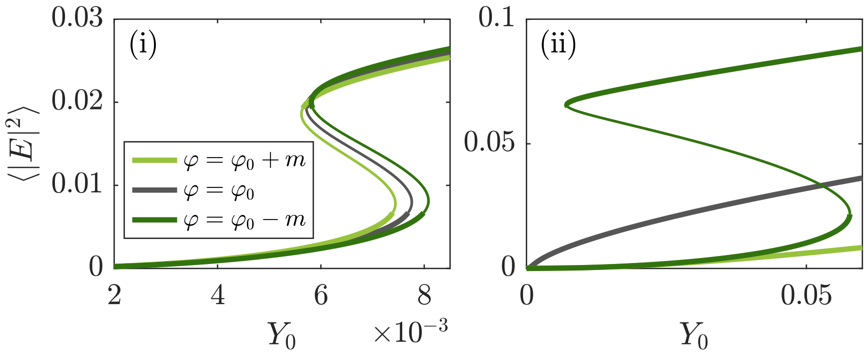

Figure 3.14: CW branches for maximal and minimal phase modulation, (i) in the LLE limit with parameters as in Fig. 3.7 with $m = 0.001$ and (ii) outside but close to the bistability region with parameters $\delta = 0.6$, $h = 2$, $\eta = 0.995$, $\varphi_0 = 1.0808$, $\tau = 300$ and $m = 0.1$.

With the parameter set studied in the last section, we have a bistability of CW solutions but are still located close to its onset. Consequently, by modulating the phase φ with a large enough amplitude, one can periodically move over the onset of bistability. This stabilizes TLSs in a parameter set that does not exhibit a bistability of CW solutions which is generally required for TLSs to occur. This scenario is depicted in Fig. 3.14 (i) and (ii). In both panels, three CW branches are shown (dark gray, light green, and dark green) corresponding to the cases $\cos(\omega t) = \{1, -1, 0\}$ where the phase modulation is at its maximum. In panel (i) all three branches show bistability, this was always the case until now.

Conversely, in panel (ii) only the branch for $\varphi = \varphi_0 - m$ exhibits bistability. In this regime the creation of TLSs without phase modulation (gray branch) would be impossible. However, due to the periodic variation in φ, the system repeatedly enters the bistable regime, enabling the formation of TLS.

The corresponding continuation for this artificial TLS formation is shown in Fig. 3.15 (i) in dark blue. The corresponding parameters are $\delta = 0.6$, $h = 2$, $\eta = 0.995$,

$\varphi_0 = 1.0808$, $m = 0.1$, $\omega = 0.0208$ and $\tau = 300$. This branch exhibits an unstructured sequence of folds where the branch gains stability at certain points. Exemplary profiles for such a stable section are shown in panel (iii) along with the periodic phase modulation in yellow. Based on the green profile shape, it can be followed that the TLSs are formed via HG modes due to its close resemblance with the profile in Fig. 3.10. The other profile shape (red) is markedly more irregular, but shows similarities to the other profile at the rising and falling edge, indicating some influence from the HG modes.

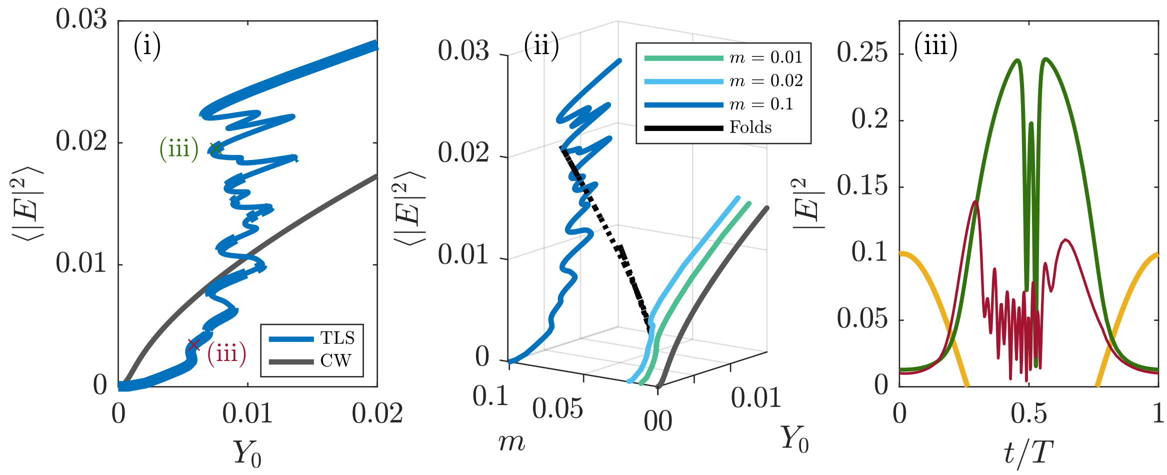

Figure 3.15: Stabilizing TLSs without having a bistable CW. (i) bifurcation diagram in Y_0. In dark gray the CW branch shows no bistability. Dark (light) green show the CW branch for maximal phase modulation with $m = 0.1$. In dark blue we have TLSs forming due to the phase modulation. (ii) shows a three-dimensional version of (i). The light blue and turquoise CW branches nucleate folds when m increases. In black we show exemplary two-parameter continuations of fold bifurcations. (iii) displays the profile corresponding to the marker in (i). We choose $\omega = 0.0208$ and the parameters are as in Fig. 3.14 (ii), technically corresponding a parameter regime without bistability of CW solutions.

In Fig. 3.15 (ii), a third axis is added to the diagram to illustrate the nucleation of fold bifurcations on the CW branch. At $m = 0.01$ (turquoise), the first fold occurs, and its two-parameter continuation is shown as a solid black line. The next fold bifurcation nucleates at $m = 0.02$ and is depicted as a dashed black line. Multiple fold bifurcations form in a similar manner, but only these two are shown for clarity.
However, the stable sections on the TLS branch are relatively small, so we do not study this effect further. Nonetheless, stabilizing TLS outside a bistability region (but close to it) is a notable finding.

3.4 Beyond the Weakly Dissipative Limit

After exploring the parameter regime of the well-studied LLE, characterized by small injection and losses where influence of the nonlinearity on the microcavity's dynamics is small. Further, we gradually increased the complexity by adjusting the detuning δ. We now transition to a parameter regime that exhibits strong characteristics of various effects and, in contrast to the regimes visited before, shows highly nonlinear

characteristics.
Specifically, we choose $\delta = 1.5$, $h = 2$, $\eta = 0.75$, $\varphi_0 = 0$, and $\tau = 100$. In this parameter range, the microcavity's dynamics are influenced by a combination of TOD, nonlinearity, group-velocity dispersion, drift, losses and injection. However, in the system's equation these effects are hidden as there is no corresponding normal form. We study the system in the normal dispersion regime, meaning δ is positive. Despite the complexity, the dynamics are not excessively intricate (unlike in Chapter 3.3 with high-frequency oscillatory tails), making the computations feasible.

3.4.1 Synchronization

The natural periods of the TLSs vary depending on the pulse shape. Therefore, there is no common natural frequency ω_0 for all TLSs. However, with sufficiently strong modulation, there exists a modulation frequency at which all pulse shapes can be synchronized simultaneously.

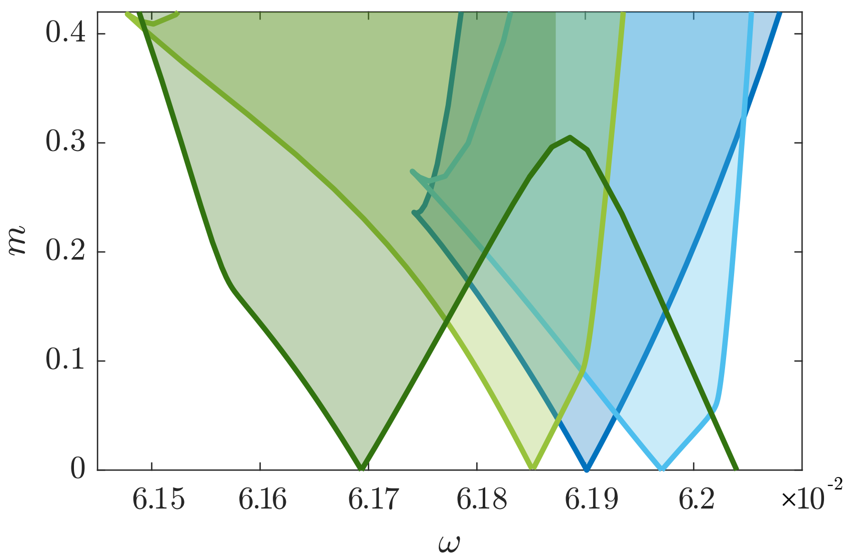

Figure 3.16: Synchronization regions of various TLS in the phase modulated KGTI. The parameters are $\delta = 1.5$, $h = 2$, $\eta = 0.75$, $\varphi_0 = 0$ and $\tau = 100$. Moreover, the colors are the same as in Fig. 3.18 and represent TLS of different widths: the first bright TLS is shown in dark blue, the second bright TLS in light blue, the first dark TLS in dark green, and the second dark TLS in light green..

First, we aim at a parameter range of (ω, m) where various pulse shapes ranging from bright to dark TLSs, as shown in Fig. 2.9, can be found. We start by using the KGTI without phase modulation, corresponding to $m = 0$, and perform time simulations with varying initial conditions, leading to periodic orbits with different profile shapes, to determine the periods T_i of all TLS. Using these periods, we initialize DNS with a small but finite value of m and a frequency ω close to $2\pi/T_i$, trapping the original pulse in the potential created by the phase modulation.
Next, we initialize a continuation in ω, similar to the red loop marking the synchronization region in Fig. 3.2 (i). For the y-measure used to plot the continuation, we

choose the detuning between the frequencies of the periodic orbit and the periodic phase modulation. This continuation produces a loop spanning horizontally across the Arnold tongue with a fixed modulation strength m, with folds on either side, as shown exemplary in Fig. 3.2 (i). We then perform a two-parameter continuation in ω and m of the fold bifurcation points. This results in synchronization tongues for each of the pulse profiles, as shown in Fig. 3.16. All resulting tongues overlap in a common region approximately at $(\omega, m) = (0.0618, 0.22)$, which is where we study our system. The colors in this diagram correspond to the profiles shown in Fig. 3.18.

For small m, the borders of the synchronization region are perfectly straight lines, a typical property of weakly forced oscillators [PRK01]. As m increases, the characteristics of the system dominate and cause different behaviors. Generally, the synchronization regions widen (up to $m \approx 0.23$), after which other system-specific effects take over and alter the shapes of the Arnold tongues, as previously discussed.

The dark green tongue exhibits a different behavior from the others, with the right-side border curving downward and reducing back to $m = 0$. However, on the right side of the bend, all solutions with the profile of the first dark TLS are unstable. Therefore, this curious part of the Arnold tongue should not influence the resulting dynamics.

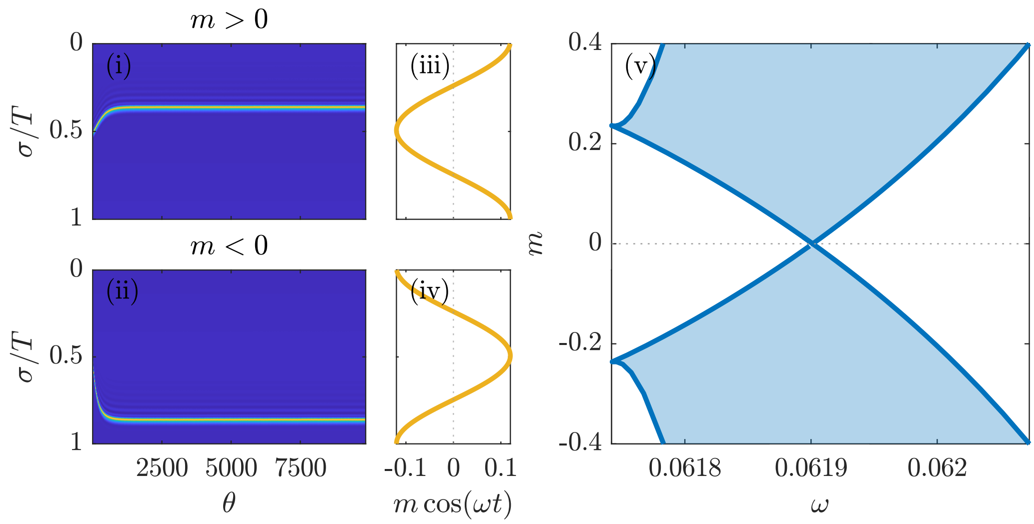

Figure 3.17: Comparison for positive and negative modulation strengths, exemplary for the first bright TLS. (i) and (ii) show DNS in a two-time representation relative to the phase modulation in (iii) and (iv), respectively, here $\omega = 0.0619$ and $|m| = 0.12$. (v) presents a two-parameter continuation of fold bifurcation points in ω and m (positive and negative) which border the synchronization region, shaded in blue. The other parameters are as in Fig. 3.16.

Additionally, we perform DNS for negative modulation strength. Intuitively, changing the sign of m corresponds to a phase shift of half a period. With all other parameters and the initial condition fixed, the resulting dynamics are quite similar. The pulse shape and the long-term position relative to the extrema of the phase modulation remain the same. The only difference in the time traces, shown in Fig. 3.17 (i) and (ii), is the transient, explained by the initial condition's position relative to the phase modulation's maxima or minima. For $m > 0$, we initialize the pulse at the minimum,

while for $m < 0$, we initialize it at the maximum, compare with Fig. 3.17 (i) - (iv). After initialization, the pulses propagate to the same position relative to the maximum of the phase modulation. Due to periodicity, the two cases are effectively identical.
Moreover, the fold bifurcation continuations that border the Arnold tongues can be extended further, crossing the line $m = 0$ to negative phase modulation amplitudes. In Fig. 3.17 (v), we show this extended continuation for the Arnold tongue of the first bright TLS. The resulting shape in the negative m half-space is identical to that for positive m. This holds true for all other pulse shapes. Thus, we will concentrate only on positive modulation strength in the following discussion.

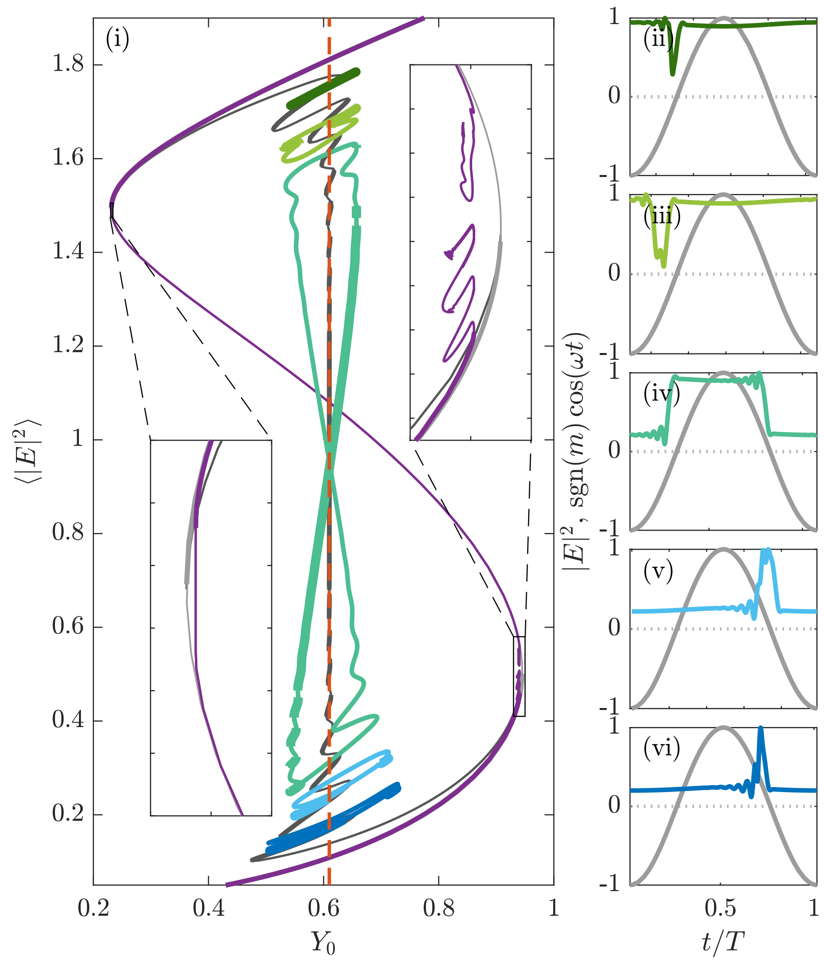

Figure 3.18: Bifurcation diagram in Y_0, shown in (i) are the case for $m = 0$: CW branch (light gray) and TLS branch (dark gray) and the separated loops for a finite modulation strength $m = 0.22$. The purple branch corresponds to the CW branch at a finite value of $m = 0.01$. In (ii) - (vi) we display the corresponding TLS profiles at the dashed orange line in (i) together with the phase modulation in gray. The parameters are $\delta = 1.5$, $h = 2$, $\eta = 0.75$, $\varphi_0 = 0$, $\omega = 0.0618$ and $\tau = 100$.

Next, at the point $(\omega, m) = (0.0618, 0.22)$, we perform a continuation in Y_0 for all pulse shapes to find a diagram that can be compared with the original case from Fig. 2.9. As before in the LLE regime, for a finite modulation strength we observe the TLS branch fragments into a stack of isolated structures similar to isolas but here varying wildly in size. The resulting bifurcation diagram is shown in Fig. 3.18 (i) and (ii) - (vi) illustrate the corresponding TLS profiles, indicated by their color, relative to the phase modulation (gray). In panel (i) we show additionally the CW branch for $m = 0$ (light gray) and at a finite value $m = 0.01$ (purple)

The isolas correspond to solutions very similar to the KGTI system without phase modulation, ranging from bright to dark TLS, originating from the locking of domain walls through TOD. This is understandable, as the phase modulation only slightly curves the low- or high-intensity background and does not eliminate the oscillatory tails caused by TOD. However, the small amount of phase modulation separates some of the windings of the snaking branch into isolated loops. Other parts form larger structures, similar to the shape of an hourglass, however still disconnected from the CW branch.

The CW branch at $m = 0.01$, Fig. 3.18 (i) (purple), is, for the most part, identical to the CW branch at $m = 0$ (light gray). However, as discussed in Chapter 3.2.1.1, the phase modulation causes the CW to deform at the fold bifurcation points (see the insets in Fig. 3.18 (i) for a closer comparison). The deformation at the upper fold bifurcation point is minor, but at the lower fold bifurcation point, the deformations are significantly more pronounced. The branch has already split and reconnected with some complex and irregular structures. Nevertheless, all these deformations of the CW branch are unstable and do not result in any observable behavior in numerical time simulations.

Even with a small modulation amplitude of $m = 0.01$, the deformations at the lower fold bifurcation point lead to highly irregular structures. Therefore, we will restrict our study of the CW branch to this small modulation amplitude.

3.4.2 Reconnecting Isolas

Now, we study what happens to the separated isolas when we increase the modulation strength. The isolas exhibit typical reconnecting behavior for increasing modulation strength, as observed in other parameter regimes. As shown in Fig. 3.18, only the dark green solution, corresponding to the first dark TLS, forms a simple loop for $m = 0.22$. All other isolas have already started to reconnect with neighboring isolas and exhibit more complex shapes. In the middle, an extended structure forms, resembling an hourglass (turquoise). Vertically, the branches correspond to typical snaking behavior, slanted by some degree. This structure consists of many isolas that have already reconnected at smaller modulation strengths.

As m increases further, the other isolas (light blue and light green) connect to the large, extended turquoise isola, see Fig. 3.19. During this process, the turquoise isola significantly widens at the top and bottom of its hourglass shape ($m = 0.3$). Further increasing m amplifies these effects. However, in the lower right part of the hourglass, the branch fully changes its behavior, forming a collapsed snaking structure oscillating around some Maxwell line parallel to the y-axis. The collapsed snaking has a tiny pinning region and is therefor not visible. However, this part gains no stability. The profiles of the solutions on this part of the branch are very different from other parts and do not resemble the original TLSs. This suggests that the increased modulation strength causes the branch to disconnect from the unstable parts and reconnect to various other unstable structures during its reshaping process, as further explored in the next paragraph. All other parts of the branch continue the described process of widening the top and bottom of the hourglass shape.

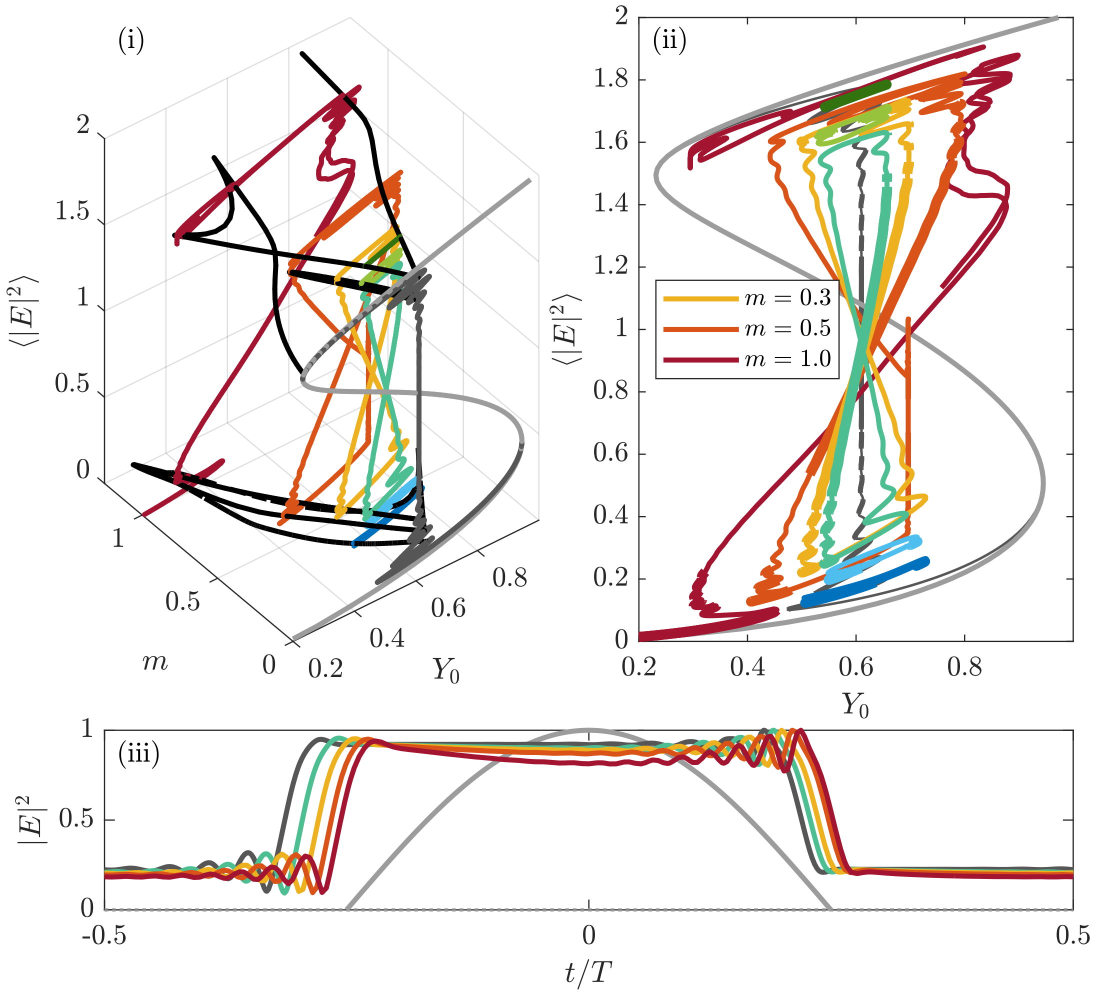

Figure 3.19: Bifurcation diagrams for increasing the modulation strength m. (i) shows continuations in Y_0 in a three-dimensional diagram where the third dimension corresponds to m. In black, we show two-parameter continuations in m and Y_0 of fold bifurcation points. (ii) displays the same branches projected onto the $(Y_0, \langle |E|^2 \rangle)$-plane, additionally to Fig. 3.18 we show branches at $m = 0.3, 0.5$ and 1.0; the other parameters are the same. A comparison of the pulse profiles relative to the potential (gray) at the smallest point of the hourglass shape is shown in (iii).

Further increasing m leads to the reconnection of the bottom of the hourglass structure to the deformed CW branch. At the top, the process is less clear. The isola corresponding to the first dark TLS state is not reconnected to the large isola like the others, but still, is increased in size and roughly mimics the shape of the CW branch. Despite this unclear behavior, we read from the diagram that at this m-value, almost all solutions are unstable, except for some of the first bright TLS.
The strong modulation of the background on which the TLS exist likely hinders the stable locking of domain walls, preventing a clear snaking structure from forming at this

parameter value. Additionally, when φ is modulated with $m = 1.0$, we periodically reach a parameter regime where the upper CW branch becomes unstable, and the mechanism for forming TLS in the normal dispersion regime breaks down due to the partial lack of bistability in homogeneous solutions. This is supported by the fact that only some bright TLS, which mostly live on the lower CW and only make short excursions to the upper CW, are stable for $m = 1.0$. Thus, strong modulation disrupts the mechanism that forms TLS within the KGTI.

For this parameter set, the influence of the phase modulation on the profile is compared with the LLE regime small, and no pulses constituted of HG modes are formed, compare with Fig. 3.19 (iii). Instead, we observe highly nonlinear effects and TOD forming TLS, as in the unmodulated case and only a small modulation of the high- and low-intensity domains. Therefore, the HG modes, which are solutions to the linearized system without TOD, do not explain the observed solutions. However, the influence of phase modulation is still visible in the discussed phenomena such as synchronization effects and new shapes of the Y_0-continuations.

In this highly nonlinear regime, at $m = 1.0$ the isolas reconnect to the deformed CW branch. For the LLE regime and in the nonlinear regime close to the LLE regime, the modulation strength has to be much smaller ($m = 0.0032$ and 0.01, respectively) for the reconnection to the CW branch. This difference is due to the proximity to the onset of bistability which is close to the LLE regime [SGJ22], and the case for nonlinear regime close to the LLE falls in between.

Close to the onset of bistability, the phase space exhibits significant changes for small parameter variations, whereas far from bifurcations, the phase space remains nearly unchanged for small parameter variations. Moreover, the mechanisms leading to a change in the dynamics due to phase modulation are fundamentally different in the two regimes. Namely, we have HG modes in the LLE regime and the interplay of a potential and TOD in the regime of this chapter.

3.4.3 Pulse Center Dynamics

In this chapter, we aim to deepen our understanding of how the phase modulation influences pulse's position when TOD is present. Numerical time simulations reveal that in the synchronized case pulses consistently travel to specific positions, depending on their shape, within the phase modulation and remain there.

To study the pulse positions effectively, we implement a *center of pulse* (COP) norm, analogous to the center of mass, on a circular domain, to account for the periodicity of the solutions as described in [BB08].

Each point in time t_i of the periodic orbit is mapped to an angle:

$$\vartheta_i = \frac{t_i}{T} 2\pi, \tag{3.9}$$

where T is the period and $t_i \in [0, T)$.

Using this angle, we calculate two new coordinates corresponding to a point on the unit circle:

$$\xi_i = \cos(\vartheta_i) \tag{3.10a}$$

$$\zeta_i = \sin(\vartheta_i). \tag{3.10b}$$

These coordinates are then multiplied by the corresponding intensities, summed, and averaged by the integrated intensity to obtain a weighted average position, similar to the center of mass:

$$\overline{\xi} = \frac{1}{\langle |E|^2 \rangle} \sum_i |E(\xi_i)|^2 \xi_i \tag{3.11a}$$

$$\overline{\zeta} = \frac{1}{\langle |E|^2 \rangle} \sum_i |E(\zeta_i)|^2 \zeta_i. \tag{3.11b}$$

Finally, these values are mapped back into a new angle $\overline{\vartheta}$,

$$\overline{\vartheta} = \mathrm{arctan2}\left(-\overline{\xi}, -\overline{\zeta}\right) + \pi. \tag{3.12}$$

Here, arctan2 is the 2-argument arctangent function. From $\overline{\vartheta}$, the center of profile t_{COP} is obtained:

$$t_{\mathrm{COP}} = T \frac{\overline{\vartheta}}{2\pi}. \tag{3.13}$$

Within the synchronization region, the pulse exhibits different stable positions depending on the imposed modulation frequency. It is notable that these positions correspond consistently to extrema of the phase modulation when located at the boundaries of an Arnold tongue in parameter space.

To investigate this behavior, we plot a continuation in ω using different norms. First, we focus on the bright TLS, previously depicted in dark blue in Fig. 3.18.

When plotted with the integrated intensity measure, the continuation forms an isolated loop, as shown in Fig. 3.20 (a), with the upper half unstable and the lower part stable. In the center of pulse (COP) norm, see Fig. 3.20 (c), we observe a periodic, cosine-like variation in the position throughout the isola. Stability changes precisely at the fold points of the isola and not in between. The positions of the pulses at the folds coincides with the extrema of the phase modulation. For the stable section, the bright pulse lives on the rising edge of the phase modulation, while for the unstable section, the pulse is situated on the falling edge. This is illustrated in Fig. 3.20 (i) and (ii) with the colored background marking the stable parts.

For the dark TLS (dark green), the position of the dashed line in Fig. 3.20 (iii) and (iv) may seem counterintuitive. However, since the calculation of t_{COP} is analogous to determining the center of mass on a periodic domain, this position precisely indicates where the highest "mass" — that is, the most intensity — is located within one period. Therefore, it is important to distinguish between the visual position of the dark TLS and the position given by t_{COP}.

The behavior and stability of the pulse position for the dark TLS are the same to those of the bright TLS when focusing on t_{COP}, see Fig. 3.20 (c) and (d) for comparison. Both types of pulses are stable when $t_{\mathrm{COP}} \in [0.5, 1]$. However, if we consider the visual position of the dark TLS, the dip that forms the dark TLS must be within the interval $[0, 0.5]$ for the TLS to be stable.

The reason behind this behavior lies in the interaction between the TLS and the phase modulation. The rising edge of the phase modulation supports the transition to the high-intensity CW state, stabilizing the bright TLS. Conversely, the falling edge hinders this transition, leading to the instability. For the dark TLS, the stable region is where

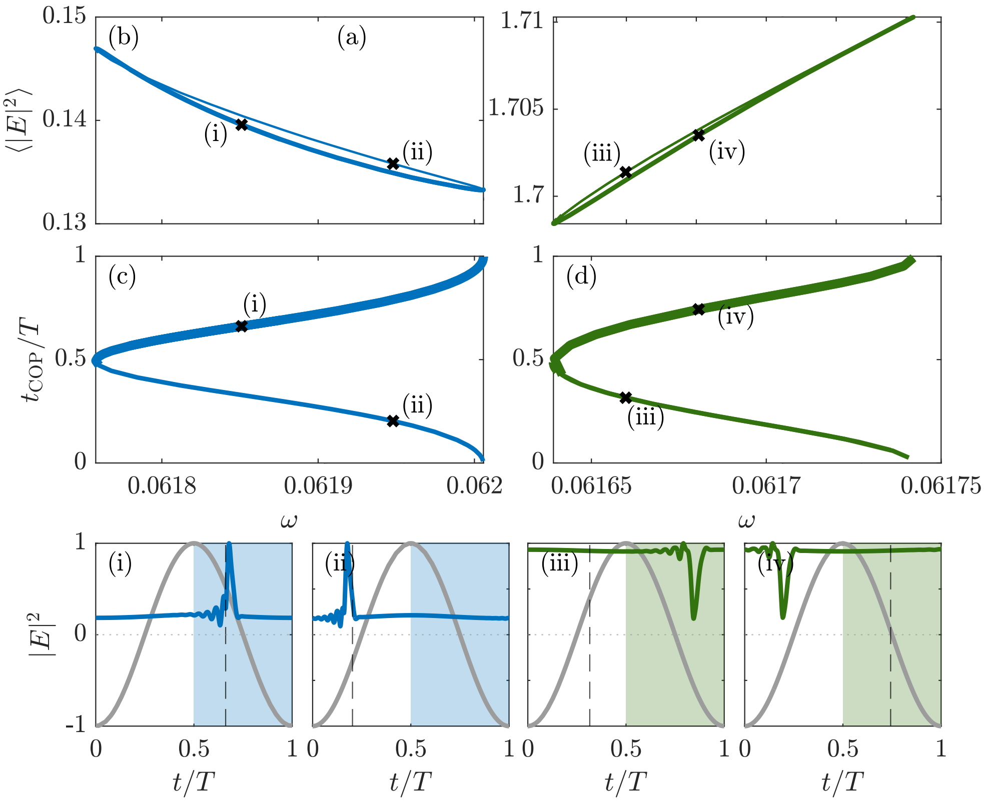

Figure 3.20: Panels (a) and (b) show continuations in ω with the integrated-intensity measure of the first bright and dark solution, respectively. Panels (c) and (d) show the same continuations in the center of pulse norm. (i) - (iv) show the pulse profiles at the indicated positions and the black dashed line shows the value of the center of pulse measure. The shaded areas corresponds to the stable sections of the branches. The parameters are as in Fig. 3.18.

the falling edge of the phase modulation facilitates the transition to the low-intensity state, while the rising edge causes instability.

Similarly, wider TLS, such as those in Fig. 3.18 (iv), are stable when the connection from the low to high-intensity CW solution is on the rising edge of the phase modulation and the connection from high to low intensity is on the falling edge. Reversing these positions, or shifting the pulse by half a period, would render the pulse unstable. This behavior is analogous to that of the narrower TLS.

3.5 Potential-Well Model

In previous chapters, we observed that with TOD activated, pulses within the KGTI with phase modulation, Eqs. (2.25a) and (2.28), settle into specific positions within the phase modulation, depending on the system parameters (ω, m). Specifically, near the edge of the synchronization region, pulses tend to localize at the extrema of the phase modulation. However, for intermediate parameter values, precisely predicting the pulse positions becomes challenging besides the general cosine-shape visible in Fig. 3.20.

This chapter aims to develop an effective equation of motion for the pulse position within the potential induced by phase modulation, viewing the pulse as a particle moving within a potential landscape. We picture the system without modulation and assume the influence of the modulation on the system is only a small perturbation. The resulting model is named potential-well model (PWM). Similar modeling approaches have successfully explained phenomena such as delay-induced depinning of localized structures in the inhomogeneous Swift-Hohenberg equation [Tab+17; Tab19], the interaction of localized structures in the delayed Adler equation [MJG20] and the arrested motion of isolated domain walls [JAH15].

3.5.1 Neutral Modes of the Adjoint System

In preparation for the derivation of the actual PWM, we start with determining the neutral modes of the system without modulation and its adjoint which are essential in the course of the derivation. Since the phase symmetry of our system is broken due to the detuned monomode injection, according to Goldstone's theorem [Gol61], the breaking of continuous symmetries leads to the appearance of new modes (or particles, in particle physics). This new mode corresponds to a translation along the periodic orbit, known as the neutral mode. The Floquet multiplier for this neutral mode is one, which is why it is used in the projection process in Chapter 3.5 to ensure a non-zero result for the involved scalar products.
In this chapter, we calculate the neutral and neutral adjoint mode of the KGTI without phase modulation, i.e. $m = 0$.

3.5.1.1 Time-Advanced System

The TLSs are periodic orbits of the system defined in Eqs. (2.25a) and (2.25b) contain delayed terms. Due to causality, the period T of the solutions must be bigger than the delay τ, which gives a residual drift or response time $\rho = T - \tau$. In the long delay limit, T and τ grow to infinity, but their difference, the residual drift, approaches a constant. Using the drift, the time delay contribution can be rewritten as a time-advanced term, i.e. $E(t-\tau) \to E(t+\rho)$. In this slightly different system, the TLS can be interpreted as homoclinic orbits. In the long delay limit, the periodic and homoclinic orbits coincide [Sch21].
The time-advanced system has the advantage that its eigenmodes are the adjoint modes of the original time-delayed system [Hal77]. Therefore, it is the aim to implement the time-advanced system and use `DDE-Biftool` functions to obtain the adjoint neutral mode of the unperturbed system.
We start with the time-delayed system of Eqs. (2.25a) and (2.25b) and introduce the abbreviations

$$\begin{aligned} \dot{E}(t) &= f(E(t), Y(t)) \\ Y(t) &= g(E(t-\tau), Y(t-\tau)). \end{aligned}$$

Next, considering periodic solutions with period $T = \tau + \rho$ (then $\tau = T - \rho$), where ρ is the response time of the system, we can write:

$$E(t-\tau) = E(t-(T-\rho)) = E(t-T+\rho) = E(t+\rho)$$

and the same holds for $Y(t-\tau) = Y(t+\rho)$.
Therefore we can rewrite our system as a time-advanced system:

$$\begin{aligned}\dot{E}(t) &= f(E(t), Y(t)),\\ Y(t) &= g(E(t+\rho), Y(t+\rho)).\end{aligned}$$

For the implementation in `DDE-Biftool` a negative time-delay is not feasible, hence some alterations have to be made:
First, the time is inverted, $t \to -t$:

$$\begin{aligned}\dot{E}(-t) &= f(E(-t), Y(-t)),\\ Y(-t) &= g(E(-t-\rho), Y(-t-\rho)).\end{aligned}$$

Second, the term $-t$ is substituted with t'

$$\begin{aligned}\dot{E}(t') &= -f(E(t'), Y(t')),\\ Y(t') &= g(E(t'-\rho), Y(t'-\rho)).\end{aligned}$$

Finally, the time-mesh of the initial condition, taken from a stable point of a branch at which we need the corresponding neutral mode of the adjoint system, is inverted, and the parameter value for τ is changed to $\rho = T - \tau$. The created continuation point is corrected, and the stability is calculated with `DDE-Biftool` functions. Simultaneously, `DDE-Biftool` computes the eigenfunctions corresponding to the Floquet multipliers. `DDE-Biftool` starts by calculating the eigenvalues with the largest magnitude first. For the stable point of the direct system, all Floquet multipliers satisfy $|\mu| \leq 1$. However, in the time-advanced system implemented in `DDE-Biftool`, all Floquet multipliers are unstable because we inverted the time to make the implementation feasible. Additionally, since `DDE-Biftool` starts with the largest eigenvalues, the neutral eigenvalue with $\mu = 1$ is the smallest for the time-inverted system. Depending on the discretization, a large number of eigenvalues are computed before reaching the neutral one. This approach makes it impossible to obtain the neutral Floquet multiplier and its corresponding eigenfunction. Consequently, a different approach to the adjoint system is required.

3.5.1.2 Linearized Delay Equation

An alternative approach to finding the neutral mode of the adjoint system is to start with the linearized delay system, which approximates the entire system well and has a known adjoint system. From the (adjoint) linearized system, time integration beginning from noise can be used to obtain the neutral mode.
First, we derive the linearized delay system. With the KGTI system (2.25a) and (2.25b) written in as vectorial system

$$\boldsymbol{M}\dot{\boldsymbol{\psi}}(t) = \boldsymbol{N}[\boldsymbol{\psi}(t), \boldsymbol{\psi}(t-\tau)] \tag{3.14}$$

where

$$\boldsymbol{\psi}(t) = \begin{pmatrix} E_{\mathrm{r}}(t)\\ E_{\mathrm{i}}(t)\\ Y_{\mathrm{r}}(t)\\ Y_{\mathrm{i}}(t)\end{pmatrix} \tag{3.15}$$

are all the involved fields E and Y with the real (E_r and Y_r) and imaginary parts (E_i and Y_i) separated and $\boldsymbol{M}$ is the mass matrix, defined as

$$\boldsymbol{M} = \begin{pmatrix} 1 & 0 & 0 & 0 \\ 0 & 1 & 0 & 0 \\ 0 & 0 & 0 & 0 \\ 0 & 0 & 0 & 0 \end{pmatrix}. \tag{3.16}$$

The mass matrix removes the derivatives of the fields Y_r and Y_i on the left-hand side, to satisfy the delay-algebraic nature of the system.
We introduce the ansatz $\boldsymbol{\psi} = \boldsymbol{\psi}_0 + \epsilon \boldsymbol{u}$, where $\boldsymbol{\psi}_0(t)$ is a T-periodic TLS solution of the unperturbed system and $\boldsymbol{u}(t)$ is a small perturbation for $\epsilon \ll 1$. The solutions for $\boldsymbol{u}(t)$ are again T-periodic and therefore fulfill the linearized equation

$$\boldsymbol{M}\dot{\boldsymbol{u}}(t) = \boldsymbol{A}(t)\boldsymbol{u}(t) + \boldsymbol{B}(t)\boldsymbol{u}(t-\tau) \tag{3.17}$$

omitting higher order in ϵ.
The T-periodic coefficient matrices are

$$\boldsymbol{A}(t) = \begin{pmatrix} -1 - 2E_\mathrm{i}E_\mathrm{r} & \delta - 3E_\mathrm{i}^2 - E_\mathrm{r}^2 & h & 0 \\ -\delta + 3E_\mathrm{r}^2 + E_\mathrm{i}^2 & -1 + 2E_\mathrm{i}E_\mathrm{r} & 0 & h \\ 0 & 0 & -1 & 0 \\ 0 & 0 & 0 & -1 \end{pmatrix} \tag{3.18}$$

and

$$\boldsymbol{B}(t) = \eta \begin{pmatrix} 0 & 0 & 0 & 0 \\ 0 & 0 & 0 & 0 \\ \cos\varphi & -\sin\varphi & -\cos\varphi & \sin\varphi \\ \sin\varphi & \cos\varphi & -\sin\varphi & -\cos\varphi \end{pmatrix}. \tag{3.19}$$

The full derivation can be seen in the Appendix A.1.
From the linearized delay equation we can find the adjoined equation by the conservation of the scalar product while shifting an operator $\mathcal{O}$: $\langle \boldsymbol{v} \mid \mathcal{O}\boldsymbol{u} \rangle = \left\langle \mathcal{O}^\dagger \boldsymbol{v} \mid \boldsymbol{u} \right\rangle$ which defines the adjoint system. Here, $\langle \boldsymbol{v}|$ is an adjoint mode and $\langle\ \rangle$ is the scalar product defined as

$$\langle \boldsymbol{v} \mid \boldsymbol{u} \rangle = \int_0^T \boldsymbol{v}(t)\boldsymbol{u}(t)\mathrm{d}t. \tag{3.20}$$

In the following, we formulate the linearized delay equation, Eq. (3.17), with operators instead of coefficients:

$$\boldsymbol{M}\dot{\boldsymbol{u}}(t) = \mathcal{L}(t)\boldsymbol{u}(t) + \mathcal{D}(t)\boldsymbol{u}(t-\tau), \tag{3.21}$$

where $\mathcal{L}(t)$ is the linear operator acting on the terms without time delay and $\mathcal{D}(t)$ is the linear operator acting on the terms with time delay.
For the derivation of the linear delay equation of the adjoint system we start by multiplying Equation (3.21) with $\boldsymbol{v}$ from the left and integrating over one period. Doing this, we end up with a scalar product. For the left-hand side, we go on with integration by parts:

$$\begin{aligned}\langle \boldsymbol{v} \mid \boldsymbol{M}\dot{\boldsymbol{u}}(t)\rangle &= \int_0^T \boldsymbol{v}(t)\boldsymbol{M}\dot{\boldsymbol{u}}(t)\mathrm{d}t \\ &= [\boldsymbol{v}(t)\boldsymbol{M}\boldsymbol{u}(t)]_0^T - \int_0^T \dot{\boldsymbol{v}}(t)\boldsymbol{M}\boldsymbol{u}(t)\mathrm{d}t \\ &= -\int_0^T \boldsymbol{M}\dot{\boldsymbol{v}}(t)\boldsymbol{u}(t)\mathrm{d}t\end{aligned} \tag{3.22}$$

where we use $[\boldsymbol{v}(t)M\boldsymbol{u}(t)]_0^T = 0$, since the solutions $\boldsymbol{u}$ and $\boldsymbol{v}$ are T-periodic.
The right-hand side holds:

$$\begin{aligned}\langle \boldsymbol{v} \mid \boldsymbol{M}\dot{\boldsymbol{u}}(t)\rangle &= \int_0^T \boldsymbol{v}(t)\left[\mathcal{L}(t)\boldsymbol{u}(t) + \mathcal{D}(t)\boldsymbol{u}(t-\tau)\right]\mathrm{d}t \\ &= \int_0^T \boldsymbol{v}(t)\left[\mathcal{L}(t)\boldsymbol{u}(t)\right]\mathrm{d}t + \int_0^T v(t)\left[\mathcal{D}(t)\boldsymbol{u}(t-\tau)\right]\mathrm{d}t \\ &= \int_0^T \left[\mathcal{L}^\dagger(t)\boldsymbol{v}(t)\right]\boldsymbol{u}(t)\mathrm{d}t + \int_\tau^{T+\tau} \boldsymbol{v}(t+\tau)\left[\mathcal{D}(t+\tau)\boldsymbol{u}(t)\right]\mathrm{d}t \\ &= \int_0^T \left[\mathcal{L}^\dagger(t)\boldsymbol{v}(t)\right]\boldsymbol{u}(t)\mathrm{d}t + \int_0^T \left[\mathcal{D}^\dagger(t+\tau)\boldsymbol{v}(t+\tau)\right]\boldsymbol{u}(t)\mathrm{d}t \\ &= \int_0^T \left[\mathcal{L}^\dagger(t)\boldsymbol{v}(t) + \mathcal{D}^\dagger(t+\tau)\boldsymbol{v}(t+\tau)\right]\boldsymbol{u}(t)\mathrm{d}t \\ &= \int_0^T \left[\boldsymbol{A}^\dagger(t)\boldsymbol{v}(t) + \boldsymbol{B}^\dagger(t+\tau)\boldsymbol{v}(t+\tau)\right]\boldsymbol{u}(t)\mathrm{d}t.\end{aligned} \tag{3.23}$$

Then we can compare the final lines for the right- and left-hand side and we follow the adjoint linear delay equation for the system reads

$$-\boldsymbol{M}\dot{\boldsymbol{v}}(t) = \boldsymbol{A}^\dagger(t)\boldsymbol{v}(t) + \boldsymbol{B}^\dagger(t+\tau)\boldsymbol{v}(t+\tau). \tag{3.24}$$

We can directly determine the adjoint coefficient matrices from the definition of $\boldsymbol{A}(t)$ and $\boldsymbol{B}(t)$.
To find the neutral modes, we integrate the linear delay equation and its adjoint counterpart numerically. Starting a numerical simulation of Equation (3.21) with noise as an initial condition will give us the neutral mode corresponding to the Floquet multiplier $\mu = 1$, which translates the system along the periodic orbit. We denote this mode as $\boldsymbol{u}_0$ or as $\boldsymbol{v}_0$ for the adjoint neutral mode, respectively. All other Floquet multipliers have a modulus smaller than 1, so the modes corresponding to these eigenvalues will decay during the time integration due to the noisy initial condition. The discretized linear delay equation, the udpate equation for the numerical integration and its derivation can be found in Appendix A.2.
Discretizing the linear adjoint system from Eq. (3.24), gives

$$-\boldsymbol{M}\frac{\boldsymbol{v}_{n+1} - \boldsymbol{v}_n}{\Delta t} = \boldsymbol{A}_n^\dagger \boldsymbol{v}_n + \boldsymbol{B}_{n+N}^\dagger \boldsymbol{v}_{n+N}. \tag{3.25}$$

This leads to the implicit scheme used for backward time integration. The time step size Δt is chosen such that $N = \dfrac{\tau}{\Delta t} \in \mathbb{N}$.

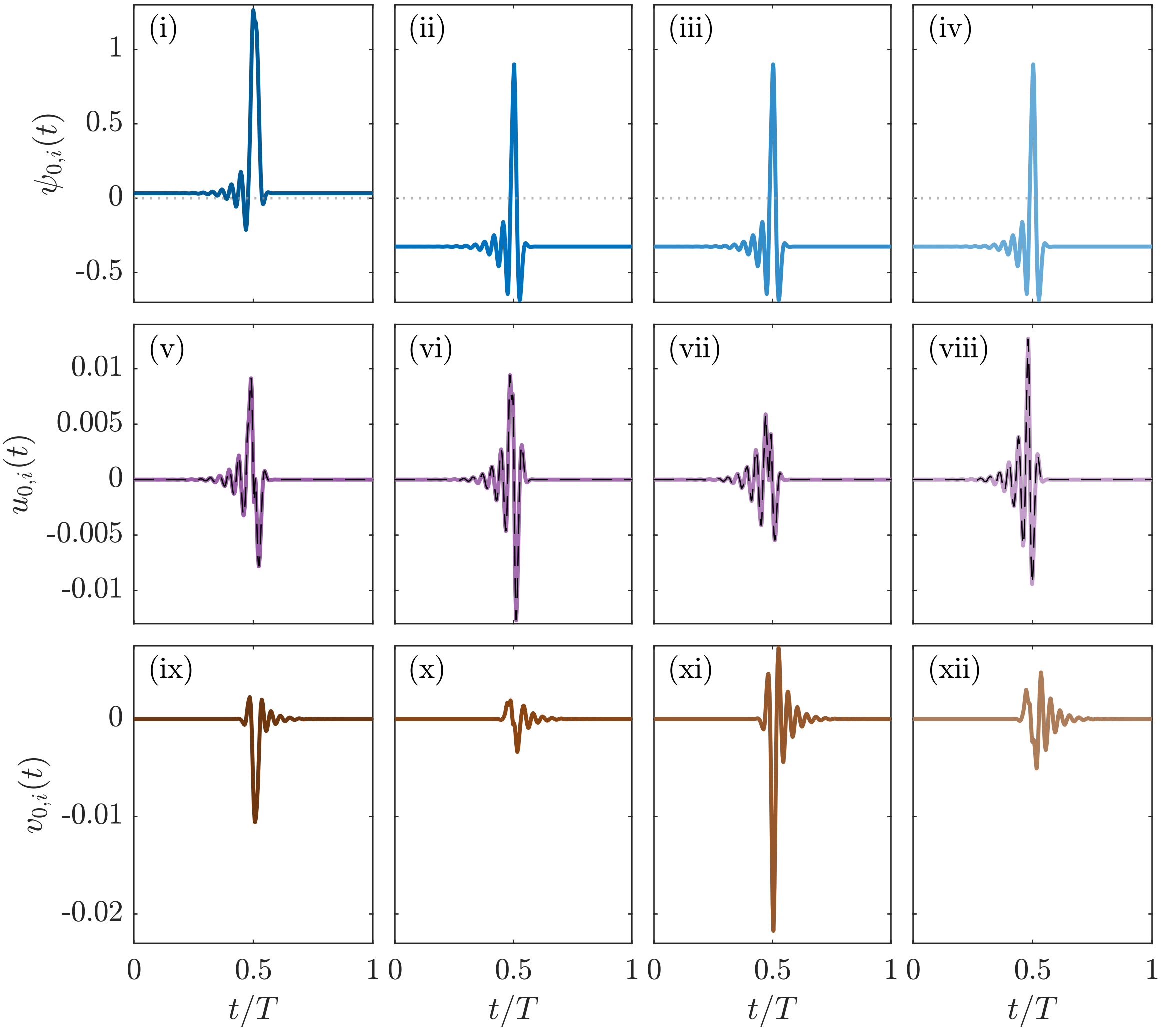

Figure 3.21: Panels (i) - (iv) show the components $\boldsymbol{\psi} = (E_\mathrm{r}, E_\mathrm{i}, Y_\mathrm{r}, Y_\mathrm{i})$ of the first bright TLS, as defined in Eq. (3.15); Panels (v) - (viii) show the components of the corresponding neutral mode $\boldsymbol{u}$, determined with the linear delay equation (purple) and with `DDE-Biftool` (dashed black), and panels (ix) - (xii) display the components of the adjoint neutral mode $\boldsymbol{v}$, respectively. The parameters are as in Fig. 3.18.

Now, solving for $\boldsymbol{v}_n$:

$$\begin{aligned} \boldsymbol{M}\boldsymbol{v}_n =& \boldsymbol{M}\boldsymbol{v}_{n+1} + \Delta t \left(\boldsymbol{A}_n^\dagger \boldsymbol{v}_n + \boldsymbol{B}_{n+N}^\dagger \boldsymbol{v}_{n+N} \right) \\ \left(\boldsymbol{M} - \Delta t \boldsymbol{A}_n^\dagger \right) \boldsymbol{v}_n =& \boldsymbol{M}\boldsymbol{v}_{n+1} + \Delta t \boldsymbol{B}_{n+N}^\dagger \boldsymbol{v}_{n+N} \\ \boldsymbol{v}_n =& \left(\boldsymbol{M} - \Delta t \boldsymbol{A}_n^\dagger \right)^{-1} \left(\boldsymbol{M}\boldsymbol{v}_{n+1} + \Delta t \boldsymbol{B}_{n+N}^\dagger \boldsymbol{v}_{n+N} \right). \end{aligned} \tag{3.26}$$

This provides the update equation which is used to find the neutral mode of the adjoint linearized system.

To illustrate the neutral modes of the linearized system and its adjoint, Fig. 3.21 presents the first bright soliton (blue, first row) alongside its corresponding neutral mode (purple, second row) and the neutral mode of the adjoint system (brown, third row), each field displayed separately according to the definition of $\boldsymbol{\psi}(t)$ in Eq. (3.15). In

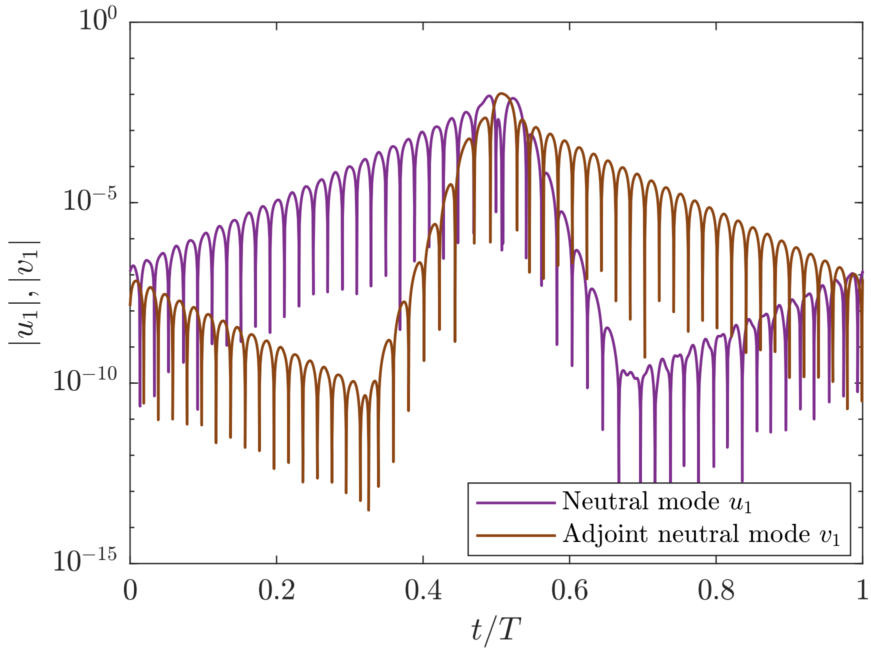

Figure 3.22: First components of the neutral mode $|u|$ (purple) and adjoint neutral mode $|v|$ (brown) in logarithmic scale. The modes are the same as in 3.21 (v) and (ix).

panels (v) - (viii) we show the neutral modes determined by `DDE-Biftool` with dashed black lines. The agreement is perfect and validates our approach via the linearized delay system.
An interesting comparison arises when plotting the neutral modes and the neutral modes of the adjoint system together in a logarithmic diagram, as shown in Fig. 3.22. As visible, the oscillatory tails are opposed, and the frequency and amplitude of the oscillations in both modes are of the same order of magnitude, highlighting their close relationship, as depicted similarly in [VGT18]. This comparison emphasizes the inherent symmetry and behavior of the system, illustrating how the neutral modes of the linearized system and its adjoint counterparts mirror each other, even in their oscillatory dynamics.

3.5.2 Derivation

We start by rewriting Eqs. (2.25a) and (2.28) as one equation:

$$\boldsymbol{M}\dot{\boldsymbol{\psi}}(t) = \boldsymbol{N}_m[\boldsymbol{\psi}(t), \boldsymbol{\psi}(t-\tau), t] \tag{3.27}$$

with the mass matrix $\boldsymbol{M}$ and $\boldsymbol{\psi}$ as defined in Eqs. (3.16) and (3.15), respectively. Due to the structure of the system's equations, we cannot separate the right-hand side into homogeneous, inhomogeneous, and delay parts as in [Tab19]. Hence, we treat the entire right-hand side as one functional.
The case $m = 0$ corresponds to the system without phase modulation, in other words, the unperturbed case without a potential:

$$\boldsymbol{M}\dot{\boldsymbol{\psi}}_0(t) = \boldsymbol{N}_0[\boldsymbol{\psi}_0(t), \boldsymbol{\psi}_0(t-\tau)]. \tag{3.28}$$

Here, $\boldsymbol{\psi}_0$ denotes solutions of the original system without phase modulation, representing the original autonomous case without direct time dependence.
We proceed under the assumption that the periodic phase modulation induces a small perturbation, primarily causing a temporal shift of the pulse without altering its overall shape. In Fig. 3.23, we compare the pulse shapes with (blue) and without (gray) phase modulation. It is evident that while the phase modulation alters the low-intensity background, the amplitude and general shape remain unchanged, validating our assumption. Notably, the phase modulation affects only the homogeneous CW solutions, leaving the domain walls unaffected.

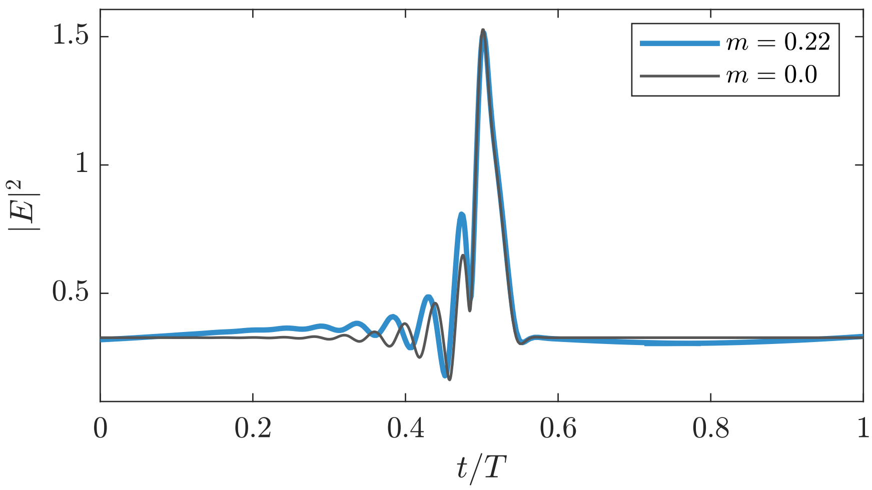

Figure 3.23: Comparison of the pulse shapes of the first bright TLS for $m = 0.0$ (black) and $m = 0.22$ (blue). All parameters are as in Fig. 3.18.

Thus, we write the ansatz:

$$\boldsymbol{\psi}(t) = \boldsymbol{\psi}_0 (t - r(t)) \tag{3.29}$$

which represents the original TLS solutions shifted by some value $r(t)$, while neglecting any deformations.
Substituting this ansatz into Eq. (3.27), we obtain:

$$\boldsymbol{M}(1 - \dot{r}(t))\, \dot{\boldsymbol{\psi}}_0(t - r(t)) = \boldsymbol{N}_m[\boldsymbol{\psi}_0 (t - r(t)), \boldsymbol{\psi}_0 (t - \tau - r(t - \tau)), t]. \tag{3.30}$$

Next, to recover $\dot{r}(t)$ from the left-hand side, we project onto the Goldstone mode $\langle \boldsymbol{v}_0(t - r(t))|$ of the adjoint system without phase modulation, as derived in the previous chapter.

$$\begin{aligned}\left\langle \boldsymbol{v}_0(t - r(t)) \middle| \boldsymbol{M}\dot{\boldsymbol{\psi}}_0(t - r(t)) \right\rangle (1 - \dot{r}(t))\\ = \left\langle \boldsymbol{v}_0(t - r(t)) \middle| \boldsymbol{N}_m[\boldsymbol{\psi}_0 (t - r(t)), \boldsymbol{\psi}_0 (t - \tau - r(t - \tau)), t] \right\rangle\end{aligned} \tag{3.31}$$

Since the solutions are periodic, we can shift the time inside the scalar product, which integrates over one period, without changing its value.

We choose to shift: $t' = t - r(t)$

$$\begin{aligned}
&\Big\langle \boldsymbol{v}_0(t') \Big| \boldsymbol{M}\dot{\boldsymbol{\psi}}_0(t') \Big\rangle \left(1 - \dot{r}(t)\right) \\
&\qquad = \Big\langle \boldsymbol{v}_0(t') \Big| \boldsymbol{N}_m \Big[\boldsymbol{\psi}_0(t'), \boldsymbol{\psi}_0\Big(t' + r(t) - \tau - r(\underbrace{t' + r(t)}_{=t} - \tau)\Big), t' + r(t) \Big] \Big\rangle \\
&\qquad = \Big\langle \boldsymbol{v}_0(t') \Big| \boldsymbol{N}_m \Big[\boldsymbol{\psi}_0(t'), \boldsymbol{\psi}_0\Big(t' - \tau\Big), t' + r(t) \Big] \Big\rangle. \qquad (3.32)
\end{aligned}$$

The argument of the delayed fields simplifies under the assumption that changes in r are small over one round trip, i.e., $r(t) \approx r(t - \tau)$.
Finally, utilizing Eq. (3.28), we substitute $M\dot{\boldsymbol{\psi}}_0(t')$ from the right-hand side and solve for $\dot{r}(t)$, yielding our equation of motion for the pulse position $r(t)$:

$$\dot{r}(t) = 1 - \frac{\Big\langle \boldsymbol{v}_0(t') \Big| \boldsymbol{N}_m \Big[\boldsymbol{\psi}_0(t'), \boldsymbol{\psi}_0\Big(t' - \tau\Big), t' + r(t) \Big] \Big\rangle}{\Big\langle \boldsymbol{v}_0(t') \Big| \boldsymbol{N}_0 [\boldsymbol{\psi}_0(t'), \boldsymbol{\psi}_0(t' - \tau)] \Big\rangle}. \qquad (3.33)$$

The scalar product in the numerator resembles a convolution when considered for all possible $r \in [0, T)$, due to its definition as $\langle \boldsymbol{\phi}(t') \mid \boldsymbol{\psi}(t') \rangle = \int_0^T \boldsymbol{\phi}^\dagger(t')\boldsymbol{\psi}(t')\mathrm{d}t'$.
The right-hand side of the effective equation of motion can be interpreted as a force $F(r)$ depending on the position r. An exemplary graph of this force and the corresponding potential $V(r)$, defined as

$$V(r) = \int_0^r -F(r')\mathrm{d}r', \qquad (3.34)$$

can be seen in Fig. 3.24 (ii). The denominator acts as a normalization and only depends on the unmodulated system. The force is periodic, compare with Fig. 3.24 (ii), just as the periodic phase modulation. At the roots of the force $F(r)$ the corresponding potential forms extrema.
In Fig. 3.24 (i), one can see that the pulse from a DNS, shown in a two-time diagram, settles nicely in the minimum of the potential $V_{\min}$, similar to the behavior of a ball rolling down a hill in the potential created by gravity. Here, the minimum of the potential calculated in the PWM and the long-term behavior of the DNS fit together. Moreover, we can compare the not only the long-term behavior but also the transient phase. To determine the time evolution of $r(t)$ from the equation of motion, we first calculate the force $F(r)$, which is the right-hand side of Eq. (3.33), as a function of r, at various r-values. Next, we discretize Eq. (3.33) as follows:

$$\frac{r_{n+1} - r_n}{\Delta t} = F(r_n) \qquad (3.35)$$

$$\Rightarrow r_{n+1} = r_n + \Delta t\, F(r_n). \qquad (3.36)$$

Which gives us the update equation for the numeric integration. Interpolation may be necessary to evaluate $F(r_n)$ accurately. The resulting motion, shown in Fig. 3.24 (i) with a red line, is compared with DNS and demonstrates good agreement with the position, except for some differences during the transient phase.

3.5.3 Comparison with DNS

When integrating the effective equation of motion for TLS of various widths, we always find a stable fixed point to which the position $r(t)$ evolves over time, corresponding to

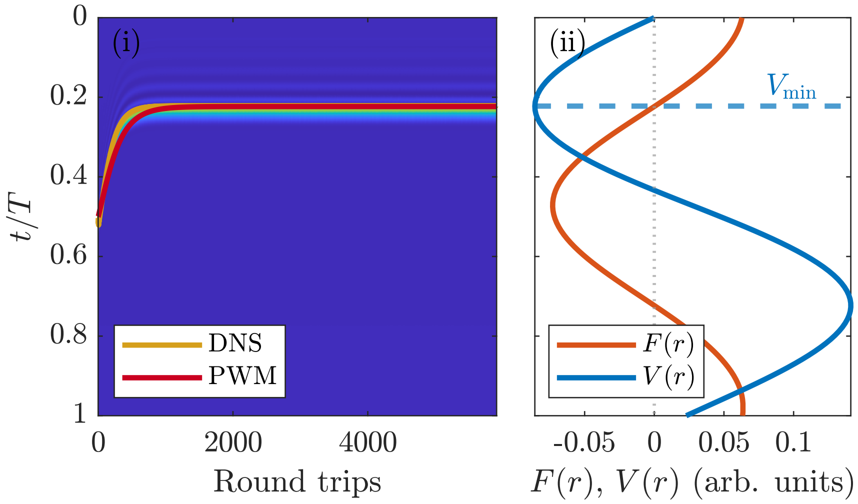

Figure 3.24: (i) shows DNS of the first bright TLS in a two-time representation with the center of pulse marked in yellow. In red we show the resulting pulse position, determined with the PWM. (ii) presents the force $F(r)$ (red) and the corresponding potential $V(r)$ (blue) calculated from the right-hand side of the effective equation of motion in Eq. (3.33), the dashed line indicates the potential minimum $V_{\min}$. All parameters are as in Fig. 3.18.

the minimum of the potential. Now, we study how the PWM predicts the motion of pulses with a different shape, we stay in the parameter set of Fig. 3.18.
In this parameter set, with $\delta = 1.5$, $h = 2$, $\eta = 0.75$, $\varphi_0 = 0$, and $\tau = 100$, we perform DNSs and track the center of the pulse profiles in two-time diagrams, shown by the yellow line in Fig. 3.25 (ii)-(vi). For better orientation we simultaneously show the bifurcation diagram in Y_0 showing the TLS isolas (i) and the corresponding profiles (vii) - (xi). For the chosen $m = 0.22$ and $\omega = 0.0618$, the DNSs yield a synchronized time evolution for all pulse shapes after a short transient. These dynamics can be recreated with the PWM, showing good qualitative agreement, compare the red and yellow lines in Fig. 3.25 (ii) - (vi). Initially, the pulses shift position until they find the optimal position within the phase modulation which coincides with the minimum of the minimum predicted by the PWM.
However, the exact transients do not fully align. The shape of the pulse (particularly the width) changes during the transient, violating the assumptions made in the derivation. But after the transient, the positions agree, indicating that the PWM is a good approximation for finding the resting position of the pulses for this parameter set.
When changing the parameters of the phase modulation, we can leave the synchronization region, leading to quasi-periodic motion that, conversely, the PWM cannot capture. Regardless of how far we move from the Arnold tongue, the periodic force (Fig. 3.24 (ii)) always changes its sign, creating a potential with minima and maxima, thus resembling synchronized dynamics. To be able to capture a quasi-periodic motion the force $F(r)$ has to lose its changes in sign to allow for saddle points or, more extrem, the complete loss of extrema in the potential.
Nevertheless, as observed before, the position of the minima of the potential $V(r)$ should change, depending on ω and m. First we will vary the modulation strength m. As shown in Fig. 3.26 (yellow), the long-term position of the first bright TLS strongly

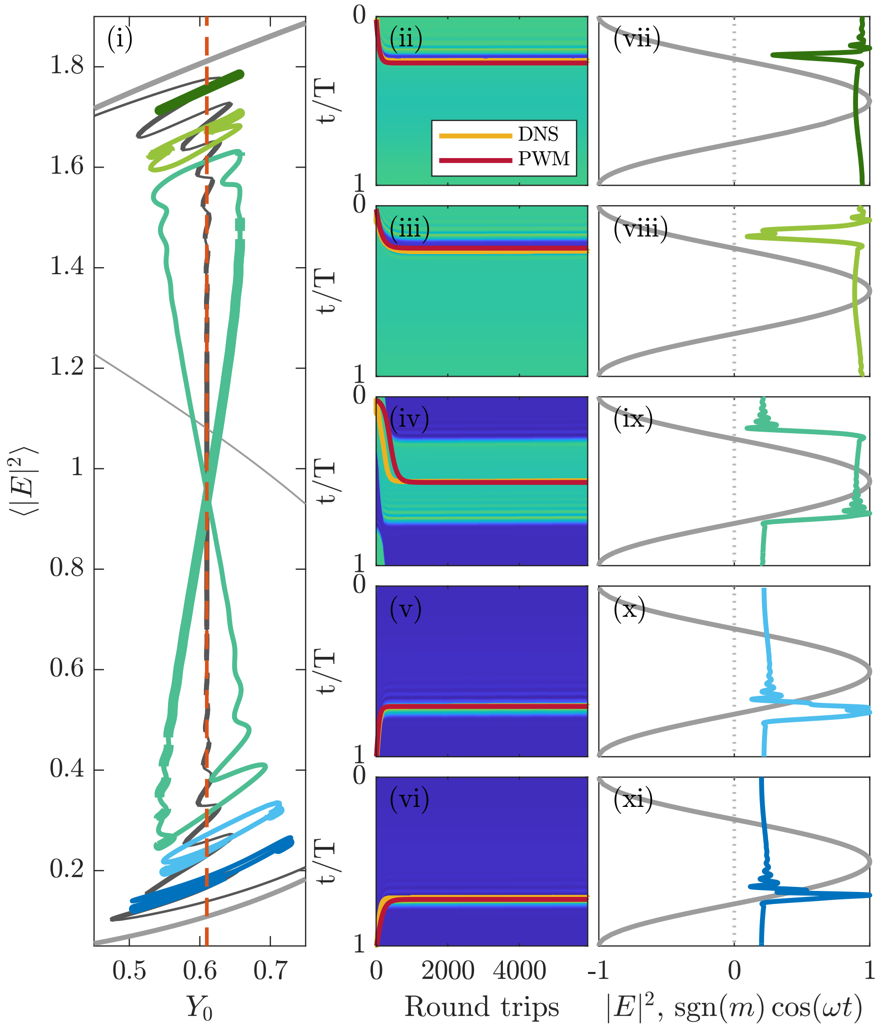

Figure 3.25: Comparison of DNS with the PWM for various pulse shapes. (i) shows continuations in Y_0, the system's parameters are the same as in Fig. 3.18. (ii) - (vi) shows two-time representations of DNS for the different pulse shapes with $Y_0 = 0.61$, as indicated by the dashed orange line in (i); in yellow the center of the pulses and in red the position $r(t)$, as determined by the PWM, are marked. (vii) - (xi) displays the long term stable pulse profiles relative to the phase modulation (gray).

depends on the modulation strength m, as determined from DNS. For smaller m, the position is at $r = 0.17$, increasing m shifts it to $r = 0.221$, and further increases move it to $r = 0.216$. For $m > 0.01$, the motion is quasi-periodic and not synchronized. The PWM, however, shows different results (red). The position determined with the PWM remains almost constant as m varies, with only a slight linear increase not visible in the diagram. This discrepancy suggests that both too small and too large of m values lead to poor agreement. The best accordance is found between $m = 0.9$ and 0.15.
A similar analysis for varying ω is plotted in Fig. 3.27. The PWM accurately describes the system at only two points, overall showing a completely different behavior than the DNS. From these sweeps, we conclude that there are significant issues with the effective equation of motion or the accompanying numerics.

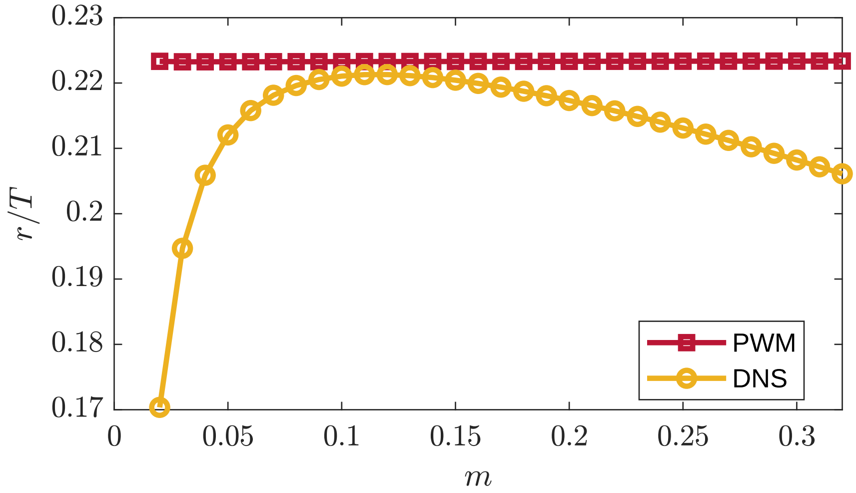

Figure 3.26: Comparison of DNS with the PWM for a parameter sweep in m. We plot the long-term stable position r of the first bright TLS in dependence of m. All other parameters are as in Fig. 3.18.

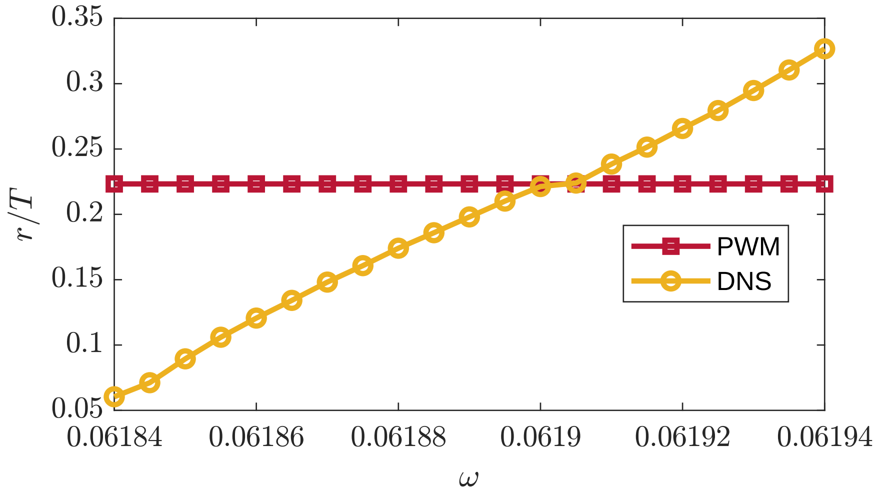

Figure 3.27: Comparison of DNS with the PWM for a parameter sweep in ω. We plot the long-term stable position r of the first brigth TLS in dependence of ω. All other parameters are as in Fig. 3.18.

Further exploration using this model cannot be useful unless the parameter sweeps agree over a broader range, such as reaching the edges of the Arnold tongue or modeling the transition to the unsynchronized case with quasi-periodic motion.
The derived system is quite complex and thus prone to errors at various points of the derivation and computation. In the course of the PWM, we combine fields from `DDE-Biftool` and our own integrator for the adjoint neutral modes. Choosing the correct point to align the profiles can be challenging. This is crucial since most parts of the profile is just a homogeneous steady state, and the real dynamics are contained in short intervals. Due to a slight time scale shift, we can lose any contribution from the dynamic parts when determining the scalar product. Numerically, the scalar product is defined as multiplying element-wise all discrete points, defining the fields or modes,

and summing over all discretization points.
Meanwhile, the neutral non-adjoint modes determined for the modes are cross-checked with `DDE-Biftool` and must be correct. In the logarithmic comparison, the adjoint modes also appear correct.
Moreover, the assumptions made in the derivation of the PWM, e.g. the constant shape of the pulse and $r(t) \approx r(t-\tau)$, may be unjustified, indicating that the neglected changes are essential for the system's dynamics. Lastly, simple and overlooked errors in the code can undermine the best derivation and render the implementation useless.

4 Conclusion and Outlook

The main goal of this thesis was to analyze the KGTI system subjected to periodic phase modulation. Through extensive numerical integration and path-continuation techniques, we studied the emerging dynamics of this expanded setup.
Phase modulation, achievable by periodically shifting the external mirror, introduces a potential to the system that alters the TLS's dynamics. In particular, we identified two distinct solution regimes within the phase-modulated KGTI. Synchronization regions, known as Arnold tongues, are crucial in determining the resulting dynamics. Within these regions, the TLS synchronize to the phase modulation. Outside these regions, the dynamics become quasi-periodic, with transitions between the two regimes occurring via a SNIPER bifurcation.
Moreover, at the edges of an Arnold tongue, the system exhibits excitable behavior where random noise can trigger pulse propagation through the space-like dimension propelled by the phase modulation and asymmetric shape, analogous to excitable dynamics in other systems like neuronal action potentials. This was demonstrated by the pulse's large excursions in response to perturbations.
In the uniform field limit and operating at $\delta = \delta_{\text{magic}}$, the resulting dynamics are dominated by the HG modes. The similarity to the LLE, combined with strong phase modulation, reveals resonance curves with peaks corresponding to HG modes. For weak phase modulation, the original collapsed snaking branch of the TLS breaks down into isolated loops. As the modulation amplitude m increases, these loops reconnect with each other and eventually with the deformed CW branch, resulting in a slanted version of the original snaking branch.
When leaving the LLE regime and simultaneously allowing for TOD, by adjusting the detuning δ and η, the pulses start to deviate from the HG-mode-induced profiles and begin to propagate since the TOD causes asymmetric pulse shapes.
In the highly nonlinear regime, the phase modulation similarly affects the collapsed snaking branch as in the LLE regime. For bright TLS, observable in the LLE regime only with TOD, the behavior is equivalent to the dark TLS. However, a large modulation amplitude destabilizes the system, while smaller m allows positioning of the TLS within the period by adjusting ω and m. However, the profiles are only slightly modulated by the phase modulation, contrary to the LLE regime, where the whole dynamics are dominated by the HG modes originating from the phase modulation.
An effective equation of motion for the TLS's position in the periodic phase modulation was derived by modeling the TLS as particles in a potential, disregarding deformations caused by phase modulation. To accurately project pulse dynamics, we calculated the neutral modes of the adjoint system. The adjoint system's neutral mode, correspond-

ing to a Floquet multiplier of one, was obtained using the linear delay equation and numerical time integration.
The PWM successfully modeled the long-term behavior for various TLS shapes for a small parameter range in ω and m. However, parameter sweeps revealed that the pulse position is highly sensitive to m and ω, a behavior not fully captured by the PWM, which shows a weak dependence on m and ω, limiting its applicability. Additionally, the PWM does not fully capture transient behaviors or the switch to quasi-periodic motion outside Arnold tongues.
For future optimizations, loosening the approximations, such as allowing small pulse deformations, could improve accuracy. Addressing potential numerical implementation errors and ensuring precise alignment of profiles in projections can also be areas for enhancement.
The study of KGTI under phase modulation reveals complex dynamics influenced by synchronization regions, modulation strength and frequency, and possible perturbations. The effective equation of motion provides a useful starting for understanding pulse behavior, though further refinements are needed to capture the full range of dynamics. Continued exploration of parameter spaces and improved numerical techniques will enhance our understanding and control of this system.
In the conservative limit the phase modulation leads mathematically to the Gross-Pitaevskii equation, which is deeply connected to the nonlinear Schrödinger equation. The Gross–Pitaevskii equation is a widely used mean-field approximation to describe Bose-Einstein condensates [MO06]. Therefore, the KGTI with phase modulation opens the possibility of finding Bose-Einstein condensates in optical time-delayed systems.
However, we were unable to identify a stable high-intensity CW solution that could serve as a foundation for dark solitons. Even a small phase modulation led to the disintegration of the CW solution, see Chapter A.3. Additionally, attempts to simulate a dark soliton without phase modulation resulted in a distortion within the CW solution, which eventually spread across the entire domain. Alternatively, the anomalous dispersion regime, where stable bright solitons have been observed, may offer a promising alternative for exploring the intriguing analogy of an optical BEC in a time-delayed system.
Revisiting the main question of this thesis, we sought to understand the emergent dynamics of the KGTI under periodic phase modulation. Our study has successfully highlighted the intricate interplay between modulation-induced changes to the TLS, alongside the synchronization and quasi-periodicity, showcasing the rich and complex behavior of this system. The effective equation of motion we developed can provide a foundation for understanding pulse behavior, and our findings open exciting avenues for further exploration. With more refined models and expanded scope of validity of the PWM, there is significant potential to enhance our grasp of these dynamics, leading to more precise control and innovative applications of these phenomena in practical settings.

Appendices

A.1 Derivation: Linear Delay System

For now we differentiate between real and imaginary part but we split the equations after the derivation. We use analogously to Equation (3.15): $\boldsymbol{u} = (u_{\mathrm{er}}, u_{\mathrm{ei}}, u_{\mathrm{yr}}, u_{\mathrm{yi}})$ and the delayed terms: $\boldsymbol{u}_\tau = (u_{\tau\mathrm{er}}, u_{\tau\mathrm{ei}}, u_{\tau\mathrm{yr}}, u_{\tau\mathrm{yi}})$. Inserting the given perturbation ansatz, we find for the first equation:

$$\dot{E}_{\mathrm{r}} + \epsilon\dot{u}_{\mathrm{er}} + i\dot{E}_{\mathrm{i}} + i\epsilon\dot{u}_{\mathrm{ei}} = \Big(-1 + i\Big\{\Big[(E_{\mathrm{r}} + \epsilon u_{\mathrm{er}})^2 + (E_{\mathrm{i}} + \epsilon u_{\mathrm{ei}})^2\Big] - \delta\Big\}\Big) \\ (E_{\mathrm{r}} + \epsilon u_{\mathrm{er}} + iE_{\mathrm{i}} + i\epsilon u_{\mathrm{ei}}) + h\left(Y_{\mathrm{r}} + \epsilon u_{\mathrm{yr}} + iY_{\mathrm{i}} + i\epsilon u_{\mathrm{yi}}\right) \quad \text{(A.1)}$$

and for the second equation:

$$0 = \eta e^{i\varphi}\left((E_{\tau\mathrm{r}} + \epsilon u_{\tau\mathrm{er}} + iE_{\tau\mathrm{i}} + i\epsilon u_{\tau\mathrm{ei}}) - (Y_{\tau\mathrm{r}} + \epsilon u_{\tau\mathrm{yr}} + iY_{\tau\mathrm{i}} + i\epsilon u_{\tau\mathrm{yi}})\right) \\ + \sqrt{1-\eta^2}Y_0 - \left(Y_{\mathrm{r}} + \epsilon u_{\mathrm{yr}} + iY_{\mathrm{i}} + i\epsilon u_{\mathrm{yi}}\right). \quad \text{(A.2)}$$

Collecting all terms of 0^{th} order in ϵ:

$$\dot{E}_{\mathrm{r}} + i\dot{E}_{\mathrm{i}} = \Big(-1 + i\Big\{\Big[E_{\mathrm{r}}^2 + E_{\mathrm{i}}^2\Big] - \delta\Big\}\left(E_{\mathrm{r}} + iE_{\mathrm{i}}\right)\Big) + h\left(Y_{\mathrm{r}} + iY_{\mathrm{i}}\right) \quad \text{(A.3)}$$

$$0 = \eta e^{i\varphi}\left((E_{\tau\mathrm{r}} + iE_{\tau\mathrm{i}}) - (Y_{\tau\mathrm{r}} + iY_{\tau\mathrm{i}})\right) + \sqrt{1-\eta^2}Y_0 - \left(Y_{\mathrm{r}} + iY_{\mathrm{i}}\right). \quad \text{(A.4)}$$

Now, for the 1^{st} order:
First, we have a look at the term in the square brackets [ ] from Equation (A.1):

$$\Big[(E_{\mathrm{r}} + \epsilon u_{\mathrm{er}})^2 + (E_{\mathrm{i}} + \epsilon u_{\mathrm{ei}})^2\Big] = \Big[E_{\mathrm{r}}^2 + 2E_{\mathrm{r}}\epsilon u_{\mathrm{er}} + \epsilon^2 u_{\mathrm{er}}^2 + E_{\mathrm{i}}^2 + 2E_{\mathrm{i}}\epsilon u_{\mathrm{ei}} + \epsilon^2 u_{\mathrm{ei}}^2\Big]. \quad \text{(A.5)}$$

Next we determine this expression which involves the terms from the square brackets:

$$[\quad]\left(E_{\mathrm{r}} + \epsilon u_{\mathrm{er}} + iE_{\mathrm{i}} + i\epsilon u_{\mathrm{ei}}\right) = E_{\mathrm{r}}^3 + 2E_{\mathrm{r}}^2\epsilon u_{\mathrm{er}} + E_{\mathrm{r}}\epsilon^2 u_{\mathrm{er}}^2 + E_{\mathrm{i}}^2 E_{\mathrm{r}} + 2E_{\mathrm{i}}E_{\mathrm{r}}\epsilon u_{\mathrm{ei}} + \epsilon^2 u_{\mathrm{ei}}^2 E_{\mathrm{r}} \\ + E_{\mathrm{r}}^2\epsilon u_{\mathrm{er}} + 2E_{\mathrm{r}}\epsilon^2 u_{\mathrm{er}}^2 + \epsilon^3 u_{\mathrm{er}}^3 + \epsilon u_{\mathrm{er}}E_{\mathrm{i}}^2 + 2E_{\mathrm{i}}\epsilon^2 u_{\mathrm{ei}}u_{\mathrm{er}} + \epsilon^3 u_{\mathrm{er}}u_{\mathrm{ei}}^2 \\ + iE_{\mathrm{i}}E_{\mathrm{r}}^2 + 2iE_{\mathrm{i}}E_{\mathrm{r}}\epsilon u_{\mathrm{er}} + \epsilon^2 u_{\mathrm{er}}^2 iE_{\mathrm{i}} + iE_{\mathrm{i}}^3 + 2iE_{\mathrm{i}}^2\epsilon u_{\mathrm{ei}} + \epsilon^2 u_{\mathrm{ei}}^2 iE_{\mathrm{i}} \\ + iE_{\mathrm{r}}^2\epsilon u_{\mathrm{ei}} + 2iE_{\mathrm{r}}\epsilon^2 u_{\mathrm{er}}u_{\mathrm{ei}} + i\epsilon^3 u_{\mathrm{er}}^2 u_{\mathrm{ei}} + i\epsilon u_{\mathrm{ei}}E_{\mathrm{i}}^2 + 2iE_{\mathrm{i}}\epsilon^2 u_{\mathrm{ei}}^2 + i\epsilon^3 u_{\mathrm{ei}}^3. \quad \text{(A.6)}$$

Then, only keeping terms of first order in ϵ we can simplify:

$$\begin{aligned}2E_\mathrm{r}^2 u_\mathrm{er} + 2E_\mathrm{i}E_\mathrm{r}u_\mathrm{ei} + &E_\mathrm{r}^2 u_\mathrm{er} + u_\mathrm{er}E_\mathrm{i}^2 + 2iE_\mathrm{i}E_\mathrm{r}u_\mathrm{er} + 2iE_\mathrm{i}^2 u_\mathrm{ei} + iE_\mathrm{r}^2 u_\mathrm{ei} + iu_\mathrm{ei}E_\mathrm{i}^2 \\ &= u_\mathrm{er}\left(3E_\mathrm{r}^2 + E_\mathrm{i}^2 + 2iE_\mathrm{i}E_\mathrm{r}\right) + u_\mathrm{ei}\left(2E_\mathrm{i}E_\mathrm{r} + 3iE_\mathrm{i}^2 + iE_\mathrm{r}^2\right) \qquad \text{(A.7)} \\ &= u_\mathrm{er}\left(3E_\mathrm{r}^2 + E_\mathrm{i}^2\right) + 2iu_\mathrm{er}E_\mathrm{i}E_\mathrm{r} + u_\mathrm{ei}\left(3iE_\mathrm{i}^2 + iE_\mathrm{r}^2\right) + 2u_\mathrm{ei}E_\mathrm{i}E_\mathrm{r}.\end{aligned}$$

Finally, we can go back to the full set of equations with all terms of first order in ϵ:

$$\begin{aligned}\dot u_\mathrm{er} + i\dot u_\mathrm{ei} &= (-1 - i\delta)(u_\mathrm{er} + iu_\mathrm{ei}) + h(u_\mathrm{yr} + iu_\mathrm{yi}) \\ &\quad + i\left[u_\mathrm{er}\left(3E_\mathrm{r}^2 + E_\mathrm{i}^2\right) + 2iu_\mathrm{er}E_\mathrm{i}E_\mathrm{r} + u_\mathrm{ei}\left(3iE_\mathrm{i}^2 + iE_\mathrm{r}^2\right) + 2u_\mathrm{ei}E_\mathrm{i}E_\mathrm{r}\right] \qquad \text{(A.8)} \\ 0 &= \eta e^{i\varphi}\left((u_{\tau\mathrm{er}} + iu_{\tau\mathrm{ei}}) - (u_{\tau\mathrm{yr}} + iu_{\tau\mathrm{yi}})\right) - (u_\mathrm{yr} + iu_\mathrm{yi}). \qquad \text{(A.9)}\end{aligned}$$

We use $e^{i\varphi} = \cos\varphi + i\sin\varphi$ to rewrite Equation (A.9) to be able to split the equations into real and imaginary parts:

$$\begin{aligned}0 = \eta((&\cos\varphi u_{\tau\mathrm{er}} + i\cos\varphi u_{\tau\mathrm{ei}} + i\sin\varphi u_{\tau\mathrm{er}} - \sin\varphi u_{\tau\mathrm{ei}} +) \\ &- (\cos\varphi u_{\tau\mathrm{yr}} + i\cos\varphi u_{\tau\mathrm{yi}} + i\sin\varphi u_{\tau\mathrm{yr}} - \sin\varphi u_{\tau\mathrm{yi}})) - (u_\mathrm{yr} + iu_\mathrm{yi}). \qquad \text{(A.10)}\end{aligned}$$

Now we are able to rewrite the linearized equations into matrix form with the fields split into real and imaginary parts as defined in Equation (3.15):

$$\begin{aligned}\boldsymbol{M}\dot{\boldsymbol{u}} = &\begin{pmatrix} -1 & \delta & h & 0 \\ -\delta & -1 & 0 & h \\ 0 & 0 & 0 & 0 \\ 0 & 0 & 0 & 0 \end{pmatrix}\boldsymbol{u} + \eta\begin{pmatrix} 0 & 0 & 0 & 0 \\ 0 & 0 & 0 & 0 \\ \cos\varphi & -\sin\varphi & -\cos\varphi & \sin\varphi \\ \sin\varphi & \cos\varphi & -\sin\varphi & -\cos\varphi \end{pmatrix}\boldsymbol{u}_\tau \\ &+ \begin{pmatrix} 0 & 0 & 0 & 0 \\ 0 & 0 & 0 & 0 \\ 0 & 0 & -1 & 0 \\ 0 & 0 & 0 & -1 \end{pmatrix}\boldsymbol{u} + \begin{pmatrix} -2E_\mathrm{i}E_\mathrm{r} & -3E_\mathrm{i}^2 - E_\mathrm{r}^2 & 0 & 0 \\ 3E_\mathrm{r}^2 + E_\mathrm{i}^2 & 2E_\mathrm{i}E_\mathrm{r} & 0 & 0 \\ 0 & 0 & 0 & 0 \\ 0 & 0 & 0 & 0 \end{pmatrix}\boldsymbol{u}. \qquad \text{(A.11)}\end{aligned}$$

Here, the terms are ordered in this way: linear parts from the first equation, delay terms (which stem only from the second equation), linear parts of the second equation and linearized nonlinear parts (only from the one term in the first equation). The mass matrix $\boldsymbol{M}$ is defined as before:

$$\boldsymbol{M} = \begin{pmatrix} 1 & 0 & 0 & 0 \\ 0 & 1 & 0 & 0 \\ 0 & 0 & 0 & 0 \\ 0 & 0 & 0 & 0 \end{pmatrix}. \qquad \text{(A.12)}$$

Finally, we bring the linearize equation into the form

$$\dot{\boldsymbol{u}} = \boldsymbol{A}(t)\boldsymbol{u}(t) + \boldsymbol{B}(t)\boldsymbol{u}(t-\tau) \qquad \text{(A.13)}$$

where we identify the T-periodic coefficients to be:

$$\boldsymbol{A}(t) = \begin{pmatrix} -1-2E_\mathrm{i}E_\mathrm{r} & \delta - 3E_\mathrm{i}^2 - E_\mathrm{r}^2 & h & 0 \\ -\delta + 3E_\mathrm{r}^2 + E_\mathrm{i}^2 & -1+2E_\mathrm{i}E_\mathrm{r} & 0 & h \\ 0 & 0 & -1 & 0 \\ 0 & 0 & 0 & -1 \end{pmatrix} \tag{A.14}$$

$$\boldsymbol{B}(t) = \eta \begin{pmatrix} 0 & 0 & 0 & 0 \\ 0 & 0 & 0 & 0 \\ \cos\varphi & -\sin\varphi & -\cos\varphi & \sin\varphi \\ \sin\varphi & \cos\varphi & -\sin\varphi & -\cos\varphi \end{pmatrix} \tag{A.15}$$

A.2 Discretizing the Linearized Delay Equation

We discretize Equation (3.21) to:

$$\boldsymbol{M}\frac{\boldsymbol{u}_n - \boldsymbol{u}_{n-1}}{\Delta t} = \boldsymbol{A}_n\boldsymbol{u}_n + \boldsymbol{B}_n\boldsymbol{u}_{n-N} \tag{A.16}$$

where we choose $N = \tau/\Delta t \in \mathbb{N}$. Solving for $\boldsymbol{u}_n$ gives us the update equation:

$$(\boldsymbol{M} - \boldsymbol{A}_n)\frac{\boldsymbol{u}_n}{\Delta t} = \boldsymbol{M}\frac{\boldsymbol{u}_{n-1}}{\Delta t} + \boldsymbol{B}_n\boldsymbol{u}_{n-N} \tag{A.17}$$

$$\Leftrightarrow \quad \boldsymbol{u}_n = (\boldsymbol{M} - \boldsymbol{A}_n)^{-1}(\boldsymbol{M}\boldsymbol{u}_{n-1} + \Delta t\boldsymbol{B}_n\boldsymbol{u}_{n-N}) \tag{A.18}$$

A.3 Conservative Limit

In the conservative limit, characterized by $\eta = 1$, both injection and loss are eliminated. Using the notation from Eq. (2.31), this implies $F(A) = 0$. Additionally, we set $\delta = \delta_\mathrm{magic}$ to eliminate TOD. The other parameters are chosen as $h = 2$, $\varphi_0 = 0$, and $\tau = 300$. We begin our analysis without phase modulation.
In this conservative limit, the Lugiato-Lefever equation (LLE) reduces to:

$$\left(i\frac{\partial}{\partial\theta} + \tilde{\varphi} - \frac{\beta_2}{2}\frac{\partial^2}{\partial\sigma^2} + \gamma|A|^2\right)A = 0 \tag{A.19}$$

This equation corresponds to the nonlinear Schrödinger equation (NLSE), with $\tilde{\varphi}$ acting as a potential. A similar form of this equation appears in the study of Bose-Einstein condensates (BEC), where it is known as the Gross-Pitaevskii equation. The Gross-Pitaevskii equation describes the ground state of a quantum system of identical bosons in the mean-field approximation [MO06].
The structural similarities between these equations suggest an intriguing analogy: the possibility of an equivalence between BEC and solitons in optical time-delayed systems. To explore this analogy, we first need to identify the CW solutions of the conservative system, which provide the foundation for the solitons. Starting from the full KGTI system without phase modulation, as defined in Eqs. (2.25a) and (2.25b), we obtain:

$$0 = \left[-1 + \left(|E_\mathrm{CW}|^2 - \delta\right)\right]E_\mathrm{CW} + hY_\mathrm{CW}, \tag{A.20a}$$

$$Y_\mathrm{CW} = E_\mathrm{CW} - Y_\mathrm{CW}. \tag{A.20b}$$

From these, we can deduce that either:

$$E_{\mathrm{CW}} = 0 \quad \text{and} \quad Y_{\mathrm{CW}} = 0 \tag{A.21}$$

or

$$E_{\mathrm{CW}} = \sqrt{\delta} \quad \text{and} \quad Y_{\mathrm{CW}} = \frac{1}{2}E_{\mathrm{CW}} = \frac{\sqrt{\delta}}{2}. \tag{A.22}$$

Using these values to initialize a DNS successfully reproduces the CW solutions.

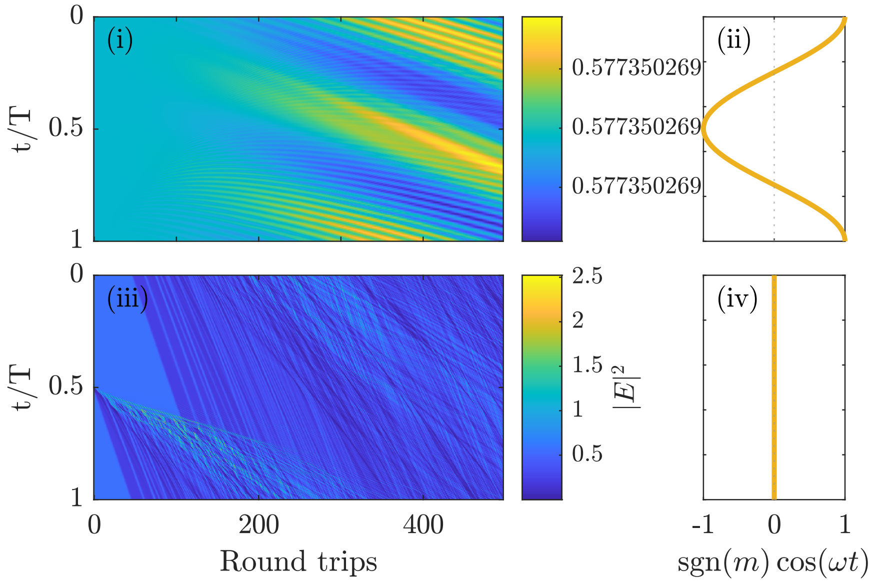

Figure 1: Two-time diagrams in the conservative regime with parameters $\delta = 1/\sqrt{3}$, $h = 2$, $\eta = 1$, $\varphi_0 = 0$, $\tau = 300$. (i) includes phase modulation with $m = 1 \cdot 10^{-6}$ and $\omega = 2\pi/301.5$ on top of the high-intensity CW solution. (iv) shows the time evolution of a dark soliton formed by connecting the high- and low-intensity solutions. (ii) and (iii) depict the corresponding phase modulation.

Next, we introduce a small phase modulation or a dark soliton connecting the high- and low-intensity solutions. The results of these DNS are shown in Fig. 1. It is evident that the phase modulation causes the high-intensity solution to collapse, behaving like an unstable solution, see Fig. 1 (i). Initially, the deviations from the high-intensity solution are minor, but over time, they grow uncontrollably, eventually leading to chaotic and shapeless time traces. In the figure, we present only a brief excerpt.
The dark soliton experiences a similar collapse, even without phase modulation. In this case, a dip in the intensity triggers a distortion that grows over successive round trips, eventually encompassing the entire domain, as depicted in Fig. 1 (iv). In both cases, stable dynamics necessary for studying optical BEC in the KGTI cannot be achieved with this setup.
Unexpectedly, in the normal dispersion regime, this line of inquiry comes to an abrupt halt. The high-intensity CW solution appears unstable, rendering this regime unsuitable for conservative dark solitons. However, stable conservative bright solitons have been observed in the KGTI under anomalous dispersion conditions, as reported in [SGJ22]. This anomalous dispersion regime may provide a promising environment for

observing a purely optical BEC in a time-delayed system. However, the anomalous dispersion regime lies beyond the scope of this thesis, which is focused on the normal dispersion regime.

References

[ABR99] F.Tito Arecchi, Stefano Boccaletti, and PierLuigi Ramazza. “Pattern formation and competition in nonlinear optics”. In: *Physics Reports* 318.1 (1999), pp. 1–83. ISSN: 0370-1573. DOI: https://doi.org/10.1016/S0370-1573(99)00007-1. URL: https://www.sciencedirect.com/science/article/pii/S0370157399000071.

[AFs15] John H. Argyris, Gunter. Faust, and SpringerLink (Online service). *An Exploration of Dynamical Systems and Chaos*. Berlin, Heidelberg: Springer Berlin Heidelberg, 2015. URL: http://dx.doi.org/10.1007/978-3-662-46042-9.

[Are+92] F. T. Arecchi et al. “Two-dimensional representation of a delayed dynamical system”. In: *Phys. Rev. A* 45 (7 Apr. 1992), R4225–R4228. DOI: 10.1103/PhysRevA.45.R4225.

[Bar+16] Stéphane Barland et al. “Localized States in Semiconductor Microcavities, from Transverse to Longitudinal Structures and Delayed Systems”. In: *Nonlinear Optical Cavity Dynamics*. John Wiley & Sons, Ltd, 2016. Chap. 4, pp. 77–106. DOI: https://doi.org/10.1002/9783527686476.ch4.

[BB08] Linge Bai and David Breen. “Calculating Center of Mass in an Unbounded 2D Environment”. In: *Journal of Graphics Tools* 13.4 (Jan. 2008), pp. 53–60. ISSN: 1086-7651. DOI: 10.1080/2151237x.2008.10129266.

[CW10] Steven T Cundiff and Andrew M Weiner. “Optical arbitrary waveform generation”. In: *Nature Photonics* 4.11 (2010), pp. 760–766.

[Del+07] P. Del’Haye et al. “Optical frequency comb generation from a monolithic microresonator”. In: *Nature* 450.7173 (Dec. 2007), pp. 1214–1217. ISSN: 1476-4687. DOI: 10.1038/nature06401.

[ELR02] K. Engelborghs, T. Luzyanina, and D. Roose. “Numerical bifurcation analysis of delay differential equations using DDE-BIFTOOL”. In: *ACM Trans. Math. Softw.* 28.1 (Mar. 2002), pp. 1–21. ISSN: 0098-3500. DOI: 10.1145/513001.513002.

[Ern08] Thomas Erneux. *Applied Delay Differential Equations*. Surveys and Tutorials in the Applied Mathematical Sciences. Dordrecht: Springer, 2008. URL: https://cds.cern.ch/record/1338316.

[Flo83] G. Floquet. “Sur les équations différentielles linéaires à coefficients périodiques”. fre. In: *Annales scientifiques de l’École Normale Supérieure* 12 (1883), pp. 47–88. URL: http://eudml.org/doc/80895.

[GA12] Philippe Grelu and Nail Akhmediev. “Dissipative solitons for mode-locked lasers”. In: *Nature Photonics* 6.2 (Feb. 2012), pp. 84–92. ISSN: 1749-4893. DOI: 10.1038/nphoton.2011.345.

[Get+22] Stephan Getzin et al. “Plant water stress, not termite herbivory, causes Namibia’s fairy circles”. In: *Perspectives in Plant Ecology, Evolution and Systematics* 57 (2022), p. 125698. ISSN: 1433-8319. DOI: https://doi.org/10.1016/j.ppees.2022.125698.

[Gol61] J. Goldstone. “Field theories with « Superconductor » solutions”. In: *Il Nuovo Cimento (1955-1965)* 19.1 (Jan. 1961), pp. 154–164. ISSN: 1827-6121. DOI: 10.1007/BF02812722.

[GP96] Giovanni Giacomelli and Antonio Politi. “Relationship between Delayed and Spatially Extended Dynamical Systems”. In: *Phys. Rev. Lett.* 76 (15 Apr. 1996), pp. 2686–2689. DOI: 10.1103/PhysRevLett.76.2686. URL: https://link.aps.org/doi/10.1103/PhysRevLett.76.2686.

[Gur22] Svetlana Gurevich. *Numerische Methoden für komplexe Systeme I.* 2022.

[Gus+15] F. Gustave et al. “Dissipative Phase Solitons in Semiconductor Lasers”. In: *Phys. Rev. Lett.* 115 (4 July 2015), p. 043902. DOI: 10.1103/PhysRevLett.115.043902. URL: https://link.aps.org/doi/10.1103/PhysRevLett.115.043902.

[Hal71] Jack K. Hale. *Functional differential equations*. Analytic theory of differential equations. Springer, Berlin, Heidelberg, 1971.

[Hal77] J.K. Hale. *Theory of Functional Differential Equations*. Applied mathematical sciences. Springer-Verlag, 1977.

[Her+14] T. Herr et al. “Temporal solitons in optical microresonators”. In: *Nature Photonics* 8.2 (Feb. 2014), pp. 145–152. ISSN: 1749-4893. DOI: 10.1038/nphoton.2013.343.

[HGJ21] Denis Hessel, Svetlana V. Gurevich, and Julien Javaloyes. “Wiggling instabilities of temporal localized states in passively mode-locked vertical external-cavity surface-emitting lasers”. In: *Opt. Lett.* 46.10 (May 2021), pp. 2557–2560. DOI: 10.1364/OL.428182. URL: https://opg.optica.org/ol/abstract.cfm?URI=ol-46-10-2557.

[HK84] B. Horovitz and J. A. Krumhansl. “Solitons in the Peierls condensate: Phase solitons”. In: *Phys. Rev. B* 29 (4 Feb. 1984), pp. 2109–2124. DOI: 10.1103/PhysRevB.29.2109. URL: https://link.aps.org/doi/10.1103/PhysRevB.29.2109.

[HTW92] M. Haelterman, S. Trillo, and S. Wabnitz. “Dissipative modulation instability in a nonlinear dispersive ring cavity”. In: *Optics Communications* 91.5 (1992), pp. 401–407. ISSN: 0030-4018. DOI: https://doi.org/10.1016/0030-4018(92)90367-Z. URL: https://www.sciencedirect.com/science/article/pii/003040189290367Z.

[Izh06] Eugene M. Izhikevich. *Dynamical Systems in Neuroscience: The Geometry of Excitability and Bursting*. The MIT Press, July 2006. ISBN: 9780262276078. DOI: 10.7551/mitpress/2526.001.0001.

[JAH15] J. Javaloyes, T. Ackemann, and A. Hurtado. "Arrest of Domain Coarsening via Antiperiodic Regimes in Delay Systems". In: *Phys. Rev. Lett.* 115 (20 Nov. 2015), p. 203901. DOI: 10.1103/PhysRevLett.115.203901. URL: https://link.aps.org/doi/10.1103/PhysRevLett.115.203901.

[Jau16] Lina Jaurigue. "Dynamics and stochastic properties of passively mode-locked semiconductor lasers subject to optical feedback". PhD thesis. Technische Universität Berlin, 2016. DOI: https://doi.org/10.14279/depositonce-5543.

[Koc+22] Elias R. Koch et al. "Square-wave generation in vertical external-cavity Kerr-Gires-Tournois interferometers". In: *Opt. Lett.* 47.17 (Sept. 2022), pp. 4343–4346. DOI: 10.1364/OL.468236.

[KV95] D. J. Korteweg and G. de Vries. "XLI. On the change of form of long waves advancing in a rectangular canal, and on a new type of long stationary waves". In: *The London, Edinburgh, and Dublin Philosophical Magazine and Journal of Science* 39.240 (1895), pp. 422–443. DOI: 10.1080/14786449508620739.

[Leo+10] François Leo et al. "Temporal cavity solitons in one-dimensional Kerr media as bits in an all-optical buffer". In: *Nature Photonics* 4.7 (July 2010), pp. 471–476. ISSN: 1749-4893. DOI: 10.1038/nphoton.2010.120. URL: https://doi.org/10.1038/nphoton.2010.120.

[LL87] L. A. Lugiato and R. Lefever. "Spatial Dissipative Structures in Passive Optical Systems". In: *Phys. Rev. Lett.* 58 (21 May 1987), pp. 2209–2211. DOI: 10.1103/PhysRevLett.58.2209. URL: https://link.aps.org/doi/10.1103/PhysRevLett.58.2209.

[LPB15] Luigi Lugiato, Franco Prati, and Massimo Brambilla. *Nonlinear Optical Systems*. Cambridge University Press, Feb. 2015. ISBN: 9781107477254. DOI: 10.1017/cbo9781107477254. URL: http://dx.doi.org/10.1017/CBO9781107477254.

[Lug+18] L. A. Lugiato et al. "From the Lugiato–Lefever equation to microresonator-based soliton Kerr frequency combs". In: *Philosophical Transactions of the Royal Society A: Mathematical, Physical and Engineering Sciences* 376.2135 (2018), p. 20180113. DOI: 10.1098/rsta.2018.0113. eprint: https://royalsocietypublishing.org/doi/pdf/10.1098/rsta.2018.0113. URL: https://royalsocietypublishing.org/doi/abs/10.1098/rsta.2018.0113.

[LWY11] M. Lichtner, M. Wolfrum, and S. Yanchuk. "The Spectrum of Delay Differential Equations with Large Delay". In: *SIAM Journal on Mathematical Analysis* 43.2 (2011), pp. 788–802. DOI: 10.1137/090766796. eprint: https://doi.org/10.1137/090766796. URL: https://doi.org/10.1137/090766796.

[MFS87] Elisha Moses, Jay Fineberg, and Victor Steinberg. "Multistability and confined traveling-wave patterns in a convecting binary mixture". In: *Phys. Rev. A* 35 (6 Mar. 1987), pp. 2757–2760. DOI: 10.1103/PhysRevA.35.2757. URL: https://link.aps.org/doi/10.1103/PhysRevA.35.2757.

[MJG20] L. Munsberg, J. Javaloyes, and S. V. Gurevich. "Topological localized states in the time delayed Adler model: Bifurcation analysis and interaction law". In: *Chaos: An Interdisciplinary Journal of Nonlinear Science* 30.6 (June 2020). ISSN: 1089-7682. DOI: 10.1063/5.0002015. URL: http://dx.doi.org/10.1063/5.0002015.

[MO06] Oliver Morsch and Markus Oberthaler. "Dynamics of Bose-Einstein condensates in optical lattices". In: *Reviews of Modern Physics* 78.1 (Feb. 2006), pp. 179–215. ISSN: 1539-0756. DOI: 10.1103/revmodphys.78.179. URL: http://dx.doi.org/10.1103/RevModPhys.78.179.

[Nie+92] F.-J. Niedernostheide et al. "Spatial and Spatio-Temporal Patterns in pnpn Semiconductor Devices". In: *physica status solidi (b)* 172.1 (1992), pp. 249–266. DOI: https://doi.org/10.1002/pssb.2221720123.

[Ode+14] V. Odent et al. "Experimental observation of front propagation in a negatively diffractive inhomogeneous Kerr cavity". In: *Phys. Rev. A* 90 (1 July 2014), p. 011806. DOI: 10.1103/PhysRevA.90.011806. URL: https://link.aps.org/doi/10.1103/PhysRevA.90.011806.

[OM15] Henrique M. Oliveira and Luís V. Melo. "Huygens synchronization of two clocks". In: *Scientific Reports* 5.1 (July 2015), p. 11548. ISSN: 2045-2322. DOI: 10.1038/srep11548. URL: https://doi.org/10.1038/srep11548.

[OTL11] V Odent, M Taki, and E Louvergneaux. "Experimental evidence of dissipative spatial solitons in an optical passive Kerr cavity". In: *New Journal of Physics* 13.11 (Nov. 2011), p. 113026. ISSN: 1367-2630. DOI: 10.1088/1367-2630/13/11/113026. URL: http://dx.doi.org/10.1088/1367-2630/13/11/113026.

[Par+21] P Parra-Rivas et al. "Origin, bifurcation structure and stability of localized states in Kerr dispersive optical cavities". In: *IMA Journal of Applied Mathematics* 86.5 (Aug. 2021), pp. 856–895. ISSN: 0272-4960. DOI: 10.1093/imamat/hxab031. eprint: https://academic.oup.com/imamat/article-pdf/86/5/856/40745316/hxab031.pdf. URL: https://doi.org/10.1093/imamat/hxab031.

[Par17] P. Parra-Rivas. "Dynamics of dissipative localized structures in driven nonlinear optical cavities". PhD thesis. 2017.

[Pes+04] M. Pesch et al. "Vectorial solitons, higher-order localized states and compound states in a single-mirror feedback system". In: *Conference on Lasers and Electro-Optics/International Quantum Electronics Conference and Photonic Applications Systems Technologies*. Optica Publishing Group, 2004, ITuH4. DOI: 10.1364/IQEC.2004.ITuH4.

[PGG17] P. Parra-Rivas, D. Gomila, and L. Gelens. "Coexistence of stable dark- and bright-soliton Kerr combs in normal-dispersion resonators". In: *Phys. Rev. A* 95 (5 May 2017), p. 053863. DOI: 10.1103/PhysRevA.95.053863. URL: https://link.aps.org/doi/10.1103/PhysRevA.95.053863.

[PRK01] A. Pikovsky, M. Rosenblum, and J. Kurths. *Synchronization : a universal concept in nonlinear sciences*. New York: Cambridge University Press, 2001.

[Sch+19] C. Schelte et al. "Tunable Kerr frequency combs and temporal localized states in time-delayed Gires–Tournois interferometers". In: *Opt. Lett.* 44.20 (Oct. 2019), pp. 4925–4928. DOI: 10.1364/OL.44.004925. URL: https://opg.optica.org/ol/abstract.cfm?URI=ol-44-20-4925.

[Sch21] C. Schelte. "Dynamics of Optical Localized Structures in Passively Mode-Locked Lasers". PhD thesis. Westfälische Wilhelms-Universität Münster, 2021.

[SGJ22] T. G. Seidel, S. V. Gurevich, and J. Javaloyes. "Conservative Solitons and Reversibility in Time Delayed Systems". In: *Phys. Rev. Lett.* 128 (8 Feb. 2022), p. 083901. DOI: 10.1103/PhysRevLett.128.083901. URL: https://link.aps.org/doi/10.1103/PhysRevLett.128.083901.

[Sie+16] Jan Sieber et al. *DDE-BIFTOOL Manual - Bifurcation analysis of delay differential equations*. 2016. arXiv: 1406.7144 [math.DS].

[SJG22] Thomas G. Seidel, Julien Javaloyes, and Svetlana V. Gurevich. "A normal form for frequency combs and localized states in Kerr–Gires–Tournois interferometers". In: *Opt. Lett.* 47.12 (June 2022), pp. 2979–2982. DOI: 10.1364/OL.457777. URL: https://opg.optica.org/ol/abstract.cfm?URI=ol-47-12-2979.

[SPH12] Albert Schliesser, Nathalie Picqué, and Theodor W. Hänsch. "Mid-infrared frequency combs". In: *Nature Photonics* 6.7 (June 2012), pp. 440–449. ISSN: 1749-4893. DOI: 10.1038/nphoton.2012.142. URL: http://dx.doi.org/10.1038/nphoton.2012.142.

[Str15] Steven H. Strogatz. *Nonlinear Dynamics and Chaos (with applications to Physics, Biology, Chemistry and Engineering)*. CRC Press, 2015.

[Sun+20] Yifan Sun et al. "Dynamics of mode-locked nanolasers based on Hermite-Gaussian modes". In: *Phys. Rev. A* 102 (4 Oct. 2020), p. 043503. DOI: 10.1103/PhysRevA.102.043503. URL: https://link.aps.org/doi/10.1103/PhysRevA.102.043503.

[Sun+22] Yifan Sun et al. "Dissipative Kerr solitons, breathers, and chimera states in coherently driven passive cavities with parabolic potential". In: *Optics Letters* 47.24 (Dec. 2022), p. 6353. ISSN: 1539-4794. DOI: 10.1364/ol.472900. URL: http://dx.doi.org/10.1364/OL.472900.

[Sun+23] Yifan Sun et al. *Nonlinear dynamics of dissipative structures in coherently-driven Kerr cavities with a parabolic potential*. 2023. arXiv: 2305.00487 [physics.optics].

[SWP23] Yifan Sun, Stefan Wabnitz, and Pedro Parra-Rivas. *Multimode resonance transition to collapsed snaking in normal dispersion Kerr resonators: Bright versus dark solitons*. 2023. arXiv: `2307.05027 [physics.optics]`.

[Tab+17] Felix Tabbert et al. "Delay-induced depinning of localized structures in a spatially inhomogeneous Swift-Hohenberg model". In: *Phys. Rev. E* 95 (3 Mar. 2017), p. 032213. DOI: `10.1103/PhysRevE.95.032213`. URL: `https://link.aps.org/doi/10.1103/PhysRevE.95.032213`.

[Tab19] Felix Tabbert. "Localized States in Dissipative Systems with Inhomogeneities". PhD thesis. Westfälische Wilhelms-Universität Münster, 2019.

[Thi21] Uwe Thiele. *Lecture "Introduction to Numerical Continuation" Winter Term 2020/21*. 2021. DOI: `10.5281/zenodo.4544848`. URL: `https://dx.doi.org/10.5281/zenodo.4544848` (visited on 01/02/2024).

[UMS96] Paul B. Umbanhowar, Francisco Melo, and Harry L. Swinney. "Localized excitations in a vertically vibrated granular layer". In: *Nature* 382.6594 (Aug. 1996), pp. 793–796. ISSN: 1476-4687. DOI: `10.1038/382793a0`. URL: `http://dx.doi.org/10.1038/382793a0`.

[VGT18] A. G. Vladimirov, S. V. Gurevich, and M. Tlidi. "Effect of Cherenkov radiation on localized-state interaction". In: *Phys. Rev. A* 97 (1 Jan. 2018), p. 013816. DOI: `10.1103/PhysRevA.97.013816`. URL: `https://link.aps.org/doi/10.1103/PhysRevA.97.013816`.

[YG14] Serhiy Yanchuk and Giovanni Giacomelli. "Pattern Formation in Systems with Multiple Delayed Feedbacks". In: *Phys. Rev. Lett.* 112 (17 May 2014), p. 174103. DOI: `10.1103/PhysRevLett.112.174103`. URL: `https://link.aps.org/doi/10.1103/PhysRevLett.112.174103`.

[YG15] Serhiy Yanchuk and Giovanni Giacomelli. "Dynamical systems with multiple long-delayed feedbacks: Multiscale analysis and spatiotemporal equivalence". In: *Phys. Rev. E* 92 (4 Oct. 2015), p. 042903. DOI: `10.1103/PhysRevE.92.042903`. URL: `https://link.aps.org/doi/10.1103/PhysRevE.92.042903`.

[YG17] Serhiy Yanchuk and Giovanni Giacomelli. "Spatio-temporal phenomena in complex systems with time delays". In: *Journal of Physics A: Mathematical and Theoretical* 50.10 (Feb. 2017), p. 103001. DOI: `10.1088/1751-8121/50/10/103001`.

[YP09] S. Yanchuk and P. Perlikowski. "Delay and periodicity". In: *Phys. Rev. E* 79 (4 Apr. 2009), p. 046221. DOI: `10.1103/PhysRevE.79.046221`. URL: `https://link.aps.org/doi/10.1103/PhysRevE.79.046221`.

[ZS72] V. E. Zakharov and A. B. Shabat. "Exact Theory of Two-dimensional Self-focusing and One-dimensional Self-modulation of Waves in Nonlinear Media". In: *Soviet Journal of Experimental and Theoretical Physics* 34 (Jan. 1972), p. 62.

Declaration of Academic Integrity

I hereby confirm that this thesis, entitled "Temporal Localized States in Injected Microcavities: The Influence of Phase Modulation" is solely my own work and that I have used no sources or aids other than the ones stated. All passages in my thesis for which other sources, including electronic media, have been used, be it direct quotes or content references, have been acknowledged as such and the sources cited. I am aware that plagiarism is considered an act of deception which can result in sanction in accordance with the examination regulations.

(Date and Signature of Student)

I consent to to having my thesis cross-checked with other texts to identify possible similarities and to having it stored in a database for this purpose.
I confirm that I have not submitted the following thesis in part or whole as an examination paper before.

(Date and Signature of Student)